NUMERICAL AND EXPERIMENTAL STUDY OF SINGLE PHASE AND MULTIPHASE DROPLET DYNAMICS ON ELECTROWETTING-ON-DIELECTRODE DIGITAL MICRO-FLUIDICS

by

MUN MUN NAHAR

Presented to the Faculty of the Graduate School of

The University of Texas at Arlington in Partial Fulfillment

of the Requirements

for the Degree of

DOCTOR OF PHILOSOPHY

THE UNIVERSITY OF TEXAS AT ARLINGTON

August 2018

To my loving mother and husband

Acknowledgements

The journey towards achieving a PhD degree has been a self-discovering experience for me. It is not only an academic accomplishment for me but also a process through which I gained valuable insights for life. It was never possible for me to complete this five-year pursuit without contributions from some of the people who directly and indirectly supported me throughout this undertaking and I am forever indebted to them. In this regard, my earnest gratitude goes towards my PhD supervisor Dr. Hyejin Moon. She is the ideal researcher that I aspire to be one day. She has given me the opportunity to develop my own ideas, to plan my own research strategies and execute them methodically. I am thankful for her support, guidance in the times when I faced various difficulties. She invested a tremendous amount of time in research discussions with me without which this dissertation would not complete successfully.

I would also like to thank my supervising committee members Dr. Ratan Kumar, Dr. Ashfaq Adnan, Dr. Miguel Amaya, Dr. Kyung Suk Yum for their valuable suggestions in my dissertation. I also thank my colleagues Venkatesan Arvind and Matin Torabinia for their various supports in my research. I am grateful to the Department of Mechanical and Aerospace Engineering to grant me Teaching Assistantship which was essential to financially support my education. I am also thankful to the facilities provided by Shimadzu Institute Nano Technology Research Center at UTA where I fabricated devices for my experiments.

I thank my husband MD Ashraful Islam for his continuous support and inspiration towards accomplishing my PhD successfully. In the most difficult times, it was his encouragement and sacrifices that made it possible for me to overcome the difficulties. I am forever thankful to my father and mother, whose love and care have made me the person that I am today. It was never possible to earn this PhD without the endless love, inspirations

and sacrifices that my mother made for me from my first day on earth until now. She was my first teacher and the most significant inspiration in my life to be a good human being. From her I learnt to gracefully face any challenge which was helpful to successfully complete my PhD as well.

July 25, 2018

Abstract

NUMERICAL AND EXPERIMENTAL STUDY OF SINGLE PHASE AND COMPOUND DROPLET DYNAMICS ON ELECTROWETTING-ON-DIELECTRODE DIGITAL MICRO-FLUIDICS

Mun Mun Nahar, PhD

The University of Texas at Arlington, 2018

Supervising Professor: Hyejin Moon

In the recent years, significant efforts have been devoted to the development of droplet based lab-on-a-chip devices of which advantages include being programmable and reconfigurable. Among various droplet flow based microsystems [1-5], electrowetting on dielectric (EWOD) digital microfluidics has many advantages, such as rapid switching response, no joule heating, no need for moving parts like pumps and valves, and most importantly low power requirement [6]. Basic droplet handling techniques - droplet dispensing, transporting, merging and splitting - can be done by sequentially activating and deactivating specific electrodes, which allows to address each droplet individually and to perform various unit processes such as encapsulation [7], mixing [8], extraction [9,10] and separation [9] in lab-on-a chip devices.

Understanding of the dynamics of droplet motion in an EWOD device is crucial to design and build devices in various applications. To date, many researchers have experimentally and numerically investigated droplet dynamics in EWOD. The review article by Mugele and Baret [6] discussed approaches to understand the electrowetting theory applicable for low voltages. They analyzed the origin of electrostatic forces that

reduce the contact angle and induce droplet motion. They also briefly discussed about the droplet dynamics.

The present study firstly [11] focuses on characterizing droplet velocity measurement and achieving faster droplet motion which is one of the basic aspects towards achieving high throughput. As we will discuss later, although many studies have been done to understand the relation between EWOD droplet velocity and various system parameters, such as electrode width, channel gap, applied voltage etc., a comprehensive guideline to measure and define the velocity of discrete deforming droplets was still missing. After characterizing the measurement technique, we used it to measure droplet velocity of a novel electrode design with different electrode operation schemes. The novel method was found to enhance the droplet velocity upto 100%. The experimental droplet velocity was compared with a theoretical model and velocity enhancement was analyzed.

In the second part of the study, we developed a numerical model for EWOD droplet motion. Navier-stokes equations coupled with the advection equation to track the interface of a water-air two-phase system was solved. Both Level Set and Phase Field method were used for the interface tracking and results from both methods were compared. Evolution of droplet shapes with time from numerical modeling was compared with that found from experiments [12].

Thirdly, we propose a study to characterize separation of phases from a compound droplet consisting of two immiscible liquids. Compound droplets can be used as an isolated unit to perform chemical reactions [13], to suppress evaporation [14], to extract agents [10]. In many of these applications, a critical step is the successful separation of the phases. Due to difference in liquid properties, the two phases of a compound droplet remain under different dynamic conditions, and separating them using

the usual technique applied on single phase droplet often does not work. Therefore, complete separation of the phases without having any residue from the other phase is challenging. During separation, the location of the pinch off point is determined by the way the neck is formed. Ideally, the interface and the pinch off point should align with each other in order to ensure minimum residue. We therefor propose to study the effects of different viscosity ratios of fluids on necking. The study will further include effects of surface tension, applied frequency in the investigation. Additionally, we will tune the location of necking before separation by applying different schemes of actuation.

Table of Contents

List of Illustrations

List of Tables

Chapter 1

Introduction

In drug delivery, pathological detection, food safety and quality control applications, bio-chemical analyses play a vital role. To isolate chemical or biological agents, to purify or concentrate, often times various sample preparation steps are required which are manually performed in a laboratory. The followed detection and measurement processes are also laborious and time consuming. The accuracy of detection techniques depends on the performance of the sample preparation steps including cleanness, purity of a compound or the concentration and therefore they need to have carefully designed methods and precise instrumentation technology and expert laboratory experts to carry out each step with extreme caution and care. With the advancement of the technology of miniaturization of many of the processes involved down to microscopic level, it has been possible to accommodate bio-chemical analyses in a single chip using the concept of lab-on-a-chip devices in a faster, automatically controlled manner with improved accuracy [15-17].

A lab-on-a-chip (LOC) is a device that integrates one or several laboratory functions on a single integrated circuit (commonly called a "chip") of only millimeters to a few square centimeters to achieve automation and high-throughput screening. They can handle extremely small fluid volumes down to less than pico-liters [15]. The concept of lab-on-a-chip device is shown in Fig. 1-1. Different steps of a bio-chemical analysis including sample preparation, purification and sensing can be integrated into a single chip. For example, an on-chip assay can be developed where DNA can be purified and detected using electro-chemical detection [16]. Lab-on-a-chip devices have been developed to detect high impact diseases such as HIV, TB [17]. They have also been used to create organ-on-chip [18] and as point of care diagnostic device

[19]. Lab-on-a-chip devices integrate various disciplines on a single chip including fluidics, electronics, optics, biosensors etc. as shown in Fig. 1-2 [20].

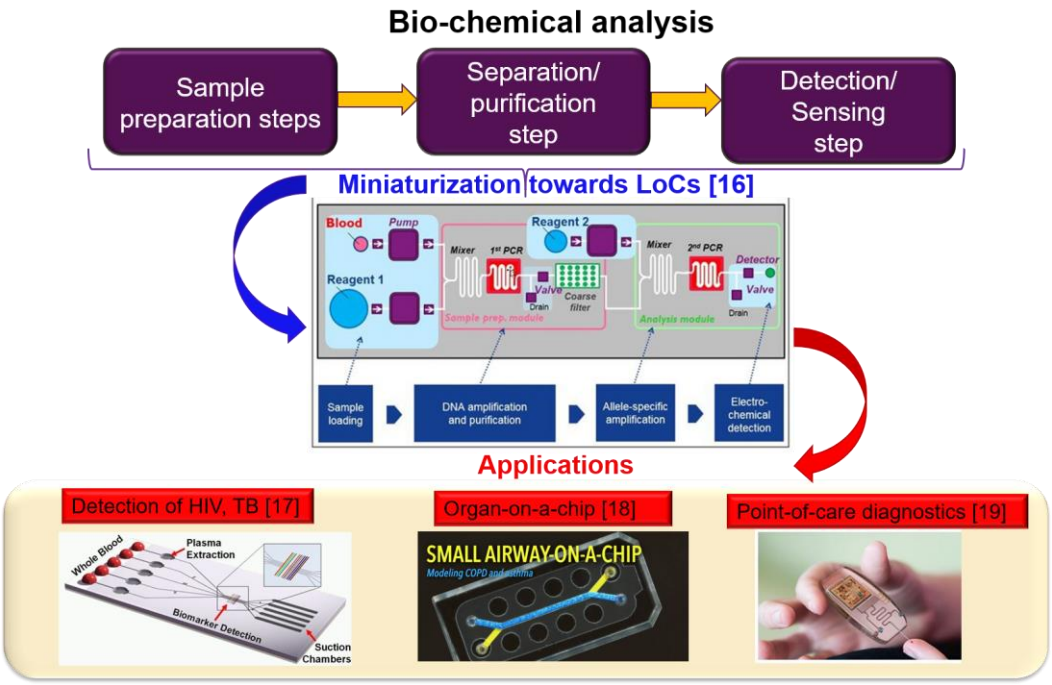

Figure 1-1 Concept of lab-on-a-chip device and its applications.

They are often called the “micro total analysis systems” or μTAS although the latter involve all the lab processes required for a particular chemical analysis whereas the former integrate one, two or more lab processes on a single chip. LoCs are subset of MEMS (Micro Electro-Mechanical Systems) and closely related to microfluidics which studies the physics of fluids at very small scale. These devices often combine fluidics, electronic, optical, biosensing processes in order to perform state-of-the-art pathological detection. The emerging microfluidic strategies in order to perform the effective integration of multiple microfluidic components leading to fully automated lab-on-a-chip

systems are: (i) Multilayer Soft Lithography; (ii) Capillary Driven and Paper-based Microfluidics; (iii) EWOD Driven Droplet Microfluidics; (iv) Multiphase Microfluidics; (v) Centrifugal Microfluidics; (vi) Electrokinetics, and (vii) Hybrid Microfluidics [20].

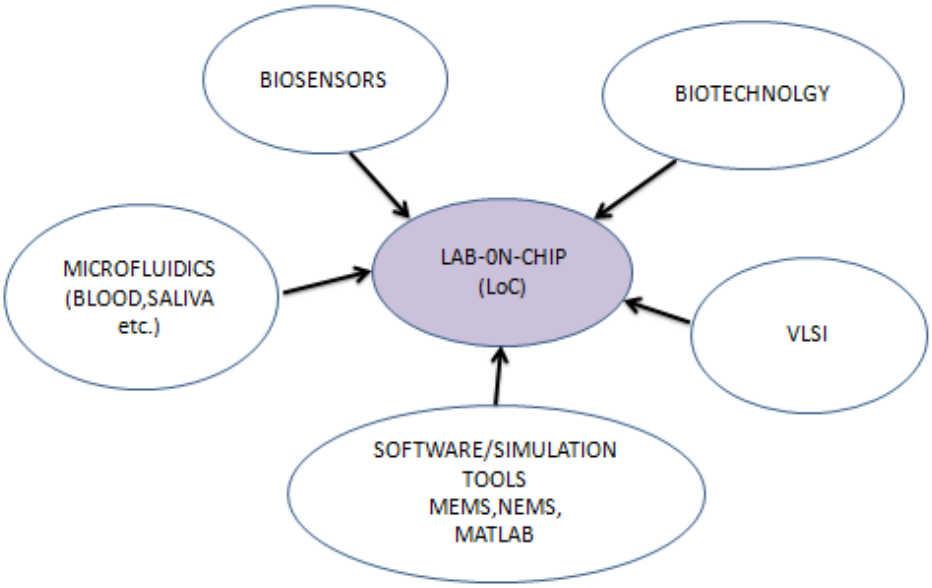

Figure 1-2 Interdisciplinary nature of lab-on-a-chip devices [15].

There are many advantages of lab-on-a-chip devices as shown in Fig. 1-3. The sample volumes of the reagents are very small in quantity and they can provide high throughput screening with total automation. Diffusion distance is smaller in small scale and mixing is faster. They also consume less power. Since they can scale single or multiple laboratory functions down to chip-format, they are extremely suitable to be utilized in the point-of-care devices. They can provide suitable platforms to perform pathological detection, proteomics, chemical synthesis, genomics etc.

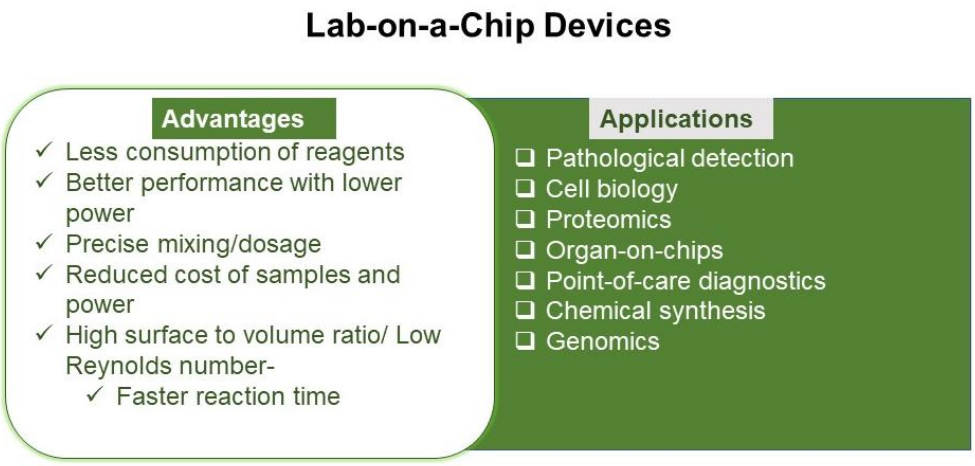

Figure 1-3 Advantages and applications of lab-on-a-chip devices.

1.1 Droplet Microfluidics

In the early 1980s, microfluidics appeared as a promising interdisciplinary technology. Microfluidics involves volumes of fluid in the range of microliters to pico-liters, and demonstrates many advantages such as rapid mass delivery and heat transfer, and reduced reagent use and waste generation. The reagent use can be reduced to nanoliters or less, and the reaction time can be reduced to mere seconds [22]. Microfluidics can be divided into two main categories: continuous microfluidics and droplet microfluidics as shown in Fig. 1-4. In continuous microfluidics, all the phases are continuous and if more than one phases are present, they are called co-flow systems. On the other hand, droplet microfluidics comprise of dispersed flow systems where one or more phases can be present as dispersed phases surrounded by a liquid/gas medium. Microdroplets offer the feasibility of handling miniature volumes (μl to fl) of fluids conveniently, provide better mixing, encapsulation, sorting, sensing and are suitable for high throughput experiments [23]. Droplet microfluidics entails both continuous-flow

emulsion-based droplet microfluidics and discrete droplet or digital droplet microfluidics as shown in Fig. 1-4. Droplet formation in the continuous-flow microfluidics is the result of an emulsion created by using two immiscible fluids, including liquid/liquid or gas/liquid systems. Various techniques, such as channel geometry (T-junction or flow-focusing) and dielectrophoresis, were well applied for good control of droplet generation [22]. For digital microfluidics, for droplet generation and actuation, typically capillary or surface tension driven actuation methods are utilized. Until now, different surface tension driven phenomena including electrowetting on dielectric (EWOD), dielectrophoresis, optical tweezers, surface acoustic waves, thermocapillary effects have been exploited to manipulate individual droplets typically surrounded by an air or oil medium as shown in Fig. 1-4(c).

There are many advantages of droplet microfluidics. For bio(chemical) reactions and analysis, droplet reactors show enhanced mixing and mass transfer within short diffusion distances, and boundary effects (such as axial dispersion) are avoided. Thus, they possess several remarkable advantages. The first is miniaturization: droplet reactors are small, in the range of sub-nanoliter scale, making single-cell or molecular analysis possible. The second is compartmentalization: droplets generated in the microfluidic channels can be manipulated independently and therefore serve as individual units for reactions. The third is parallelization: droplets are monodispersed and identical, hence provide large-scale quantitative reaction platforms for high-throughput analysis. Therefore, droplet microfluidics offers a route to performing typical laboratory operations with a small volume of reagents in significantly less time.

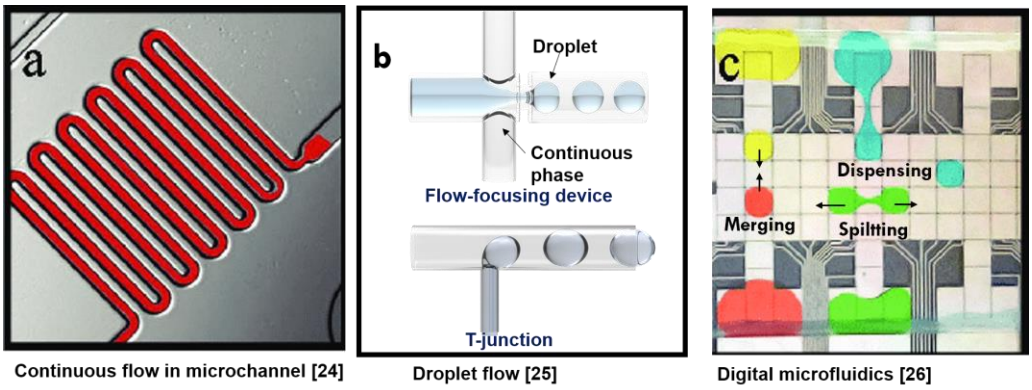

Figure 1-4 Different microfluidic systems (a) Continuous flow in a microchannel (b) droplet generation in a flow focusing device and in a T-junction (c) droplet manipulation in a digital microfluidic device.

Chapter 2

Electrowetting on Dielectric Digital Microfluidics Devices

In microscale, surface tension force dominates over gravitational and other body forces. Electrowetting on dielectric is one of the methods to utilize this. In electrowetting, nano to pico liter sized droplets can be handled by manipulating the wetting behavior of conductive liquid droplets placed on a conductive solid surface by applying voltage on that surface. The solid surface is generally coated with a dielectric layer to prevent electrolysis. Air or another liquid immiscible with the droplet liquid serves as a medium. The EWOD principle can be described using Fig. 2-1. A droplet resting on a solid surface is in equilibrium condition. Now voltage is applied on the electrically conductive surface and electrical charges accumulate along the solid-liquid interface thus forming an electric double layer. Because of the accumulated charges, the effective solid-liquid interfacial tension is reduced and the previous equilibrium is broken. Therefore, droplet reaches to a new equilibrium condition. To balance the interfacial energies at the three-phase contact line, the apparent contact angle between droplet and solid substrate is reduced. This is a reversible process meaning that when the voltage is removed, the droplet regains the initial contact angle.

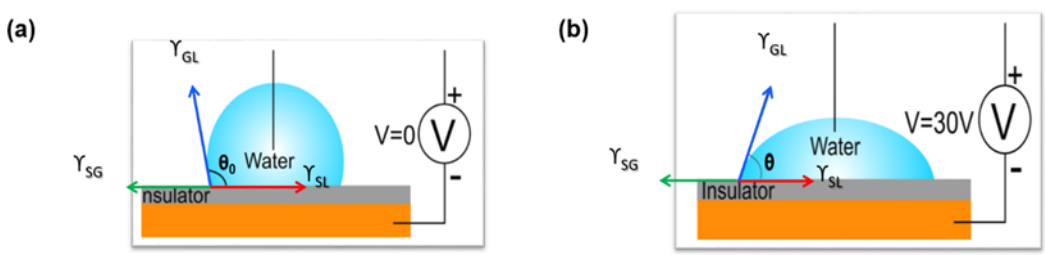

Figure 2-1 Electrowetting on dielectric principle. (a) A droplet resting on a solid surface with a contact angle θ_o at 0 voltage. (b) Contact angle changes to θ after applying voltage, V. γ_{SL}, γ_{SG} and γ_{GL} are the interfacial tensions between solid-liquid, solid-air and air-liquid respectively.

2.1 Theory of Electrowetting-on-Dielectric

In electrowetting, mostly partially wetting liquids on planar solid substrates are used where the droplets can be composed of aqueous salt solutions with a radius in the order of 1 mm or less [6]. Since the Bond number, $B_o = \sqrt{(\frac{\Delta\rho R^2}{\sigma})}$ is less than unity, the system is governed by surface tension forces rather than gravity. The free energy of the droplet, F is given as the product of the droplet interfacial area, A_i and the interfacial tension, σ_i as Eq. 2.1.

$$F = \sum Ai\sigma i - \lambda V \tag{2.1}$$

Where, λ being a Lagrangian variable, enforces the volume to remain constant and is equal to the pressure drop, ΔP across the liquid-vapor interface. Two conditions are derived by variational minimization of the above equation which all liquid morphologies need to fulfill to maintain equilibrium. The first one is the Laplace equation, which states that pressure jump across the interface does not change with the position:

$$\Delta P = \sigma_{lv}\left[\frac{1}{r_1} + \frac{1}{r_2}\right] = \sigma_{lv}\kappa \tag{2.2}$$

Here, r_1, r_2 are the principal radii of curvature and *k is the* mean curvature. The second condition relates Young's equilibrium contact angle θ_Y to the interfacial energies. According to this relation, when horizontal components of thee interfacial tensions are balanced without any external applied potential, the following relation is derived:

$$\sigma_{lv}\cos\theta_0 + \sigma_{sl(0)} = \sigma_{sv} \tag{2.3}$$

Here, s, l, v represents solid, liquid and vapor phases respectively and subscript 'o' denotes zero applied voltage. In the presence of applied voltage, the above relation takes the following form:

$$\sigma_{lv} \cos \theta_v + \sigma_{sl(V)} = \sigma_{sv} \tag{2.4}$$

where "v" denotes the applied voltage. Now combining Eq. 2.3 and 2.4, Eq. 2.5 is obtained:

$$\cos \theta_v - \cos \theta_0 = \frac{\sigma_{sl(0)} - \sigma_{sl(v)}}{\sigma_{lv}} \tag{2.5}$$

The right hand side of Eq. 2.5 can be expressed as the following with C being the system capacitance and V the applied voltage:

$$\cos \theta_v - \cos \theta_0 = \frac{1}{2} C V^2 \tag{2.6}$$

Equation 2.6 is the Lippmann-Young equation which expresses relation between applied voltage and the change in the contact angle [6].

2.2 Droplet Actuation using EWOD

Using electrowetting principle, wetting behavior of pico-liter to microliter sized droplets can be changed on a partially-non wetting surface and droplets can be manipulated in various ways. Two types of configurations can be used for EWOD devices as the following:

a) Sessile configuration where the droplet rests on a substrate
b) Sandwiched configuration where the droplet is sandwiched between two parallel plates.

Figure 2-2 illustrates the method of actuating a droplet using electrowetting principle. In this demonstration, a parallel plate EWOD device is used. The bottom plate contains an array of electrodes which have switches to turn them on and off. The top

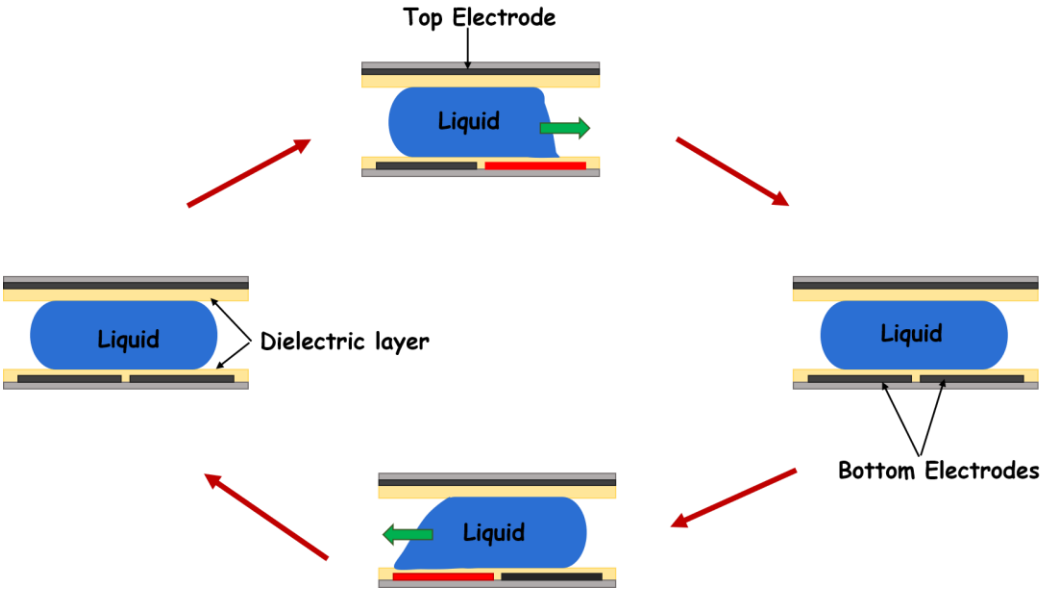

Figure 2-2 EWOD droplet actuation mechanism.

plate however is a single conductive layer which is grounded. To avoid electrolysis and increase the range of operating voltage, the conductive layer is coated with a dielectric material. Both the top and bottom plate have hydrophobic coatings at the topmost surface which comes into contact with the droplet. Initially the droplet sits on the substrate in such a way that its meniscus partially touches the next electrode. Now if that electrode is turned on, the part of the droplet meniscus which is on the electrode partially wets the surface and the contact angle locally changes on that portion of the meniscus. The change in the contact angle changes the curvature locally which in turn creates non-uniformity in the Laplace pressure difference across the interface according to Eq. 2.2. This local imbalance in pressure inside the droplet gives rise to a net driving force towards the active electrode and the droplet moves until its advancing meniscus reaches

the edge of that electrode. In typical EWOD devices, an array or a matrix of electrodes can be built and droplets can be moved along the array or on the matrix by sequentially switching on adjacent electrodes. Because a droplet can be handled individually, these devices are often called digital microfluidics devices.

2.3 EWOD applications, advantages and examples

By using electrowetting, a droplet can be formed, split into two droplets, two droplets can be merged together and transported. Many of these operations are required in lab-on- a-chip systems. In general, digital microfluidics offers several advantages over continuous or microchannel based systems such as the following:

- Low power requirement
- Small sample volume required for biological applications
- No moving parts such as pumps, valves required by the system
- Droplets can be controlled independently
- Devices can be programmed in a flexible manner

There are other techniques which have been used as the actuation mechanism in digital microfluidic devices [27]. Among them, optofluidic methods including optical tweezers, optical vortex, dielectrophoresis and surface acoustic waves are the most common. But because of the simplicity in working principle and reduced number of required mechanical parts, EWOD system has become the most popular option.

The following chart shows some of the applications of EWOD. It has been prominently used in sample preparation and sensing steps in many chemical and biological applications [28, 29]. Other applications include novel concepts such as digital cooling [27, 30], liquid lenses [31] etc. Because of the flexibility and automatic operation

mode, EWOD devices are good candidates for developing portable point of care devices, display systems and wearables for health monitoring purposes. They have also been used as the energy harvester [32].

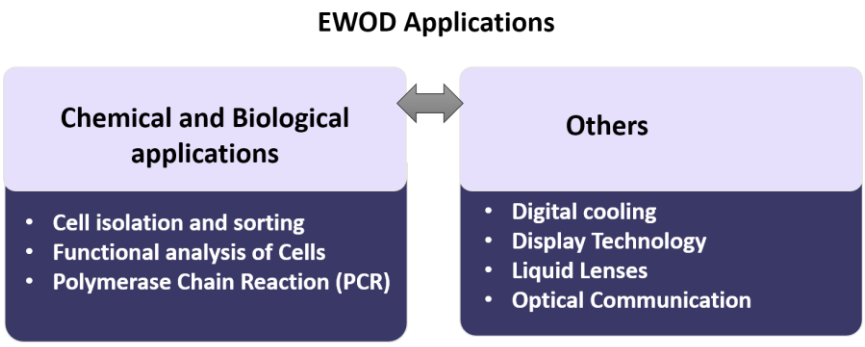

Figure 2-3 Applications of EWOD principle.

2.3.1 EWOD Device Design

For the parallel plate configurations, which is used in the current research, device design mainly involves designing the bottom chip. Based on the operations required for a particular study, a layout of the droplet actuation sequence is created and arrangement of the electrodes are designed on the mask. In our case, LEDIT has been used to make the layout. The design is then patterned on chromium coated glass mask. Usually, if the top plate does not contain anything such as sensors or microheaters, there is no need of designing the top chip.

Figure 2-4 shows the design on a mask for the bottom chip. The pattern from the mask would be transferred to a circular wafer during photolithography and therefore the mask has a circular outline and alignment marks. The mask contains the designs of (i) electrodes, separated from other nearby electrodes by a small gap of 10μm, (ii) contact pads, which connect the voltage supply (PCB board) to the electrodes, (iii) contact lines

which act as wires between electrodes and contact pads. The PCB board contains relays or switches which control voltage supply to individual electrodes. A customized LABVIEW

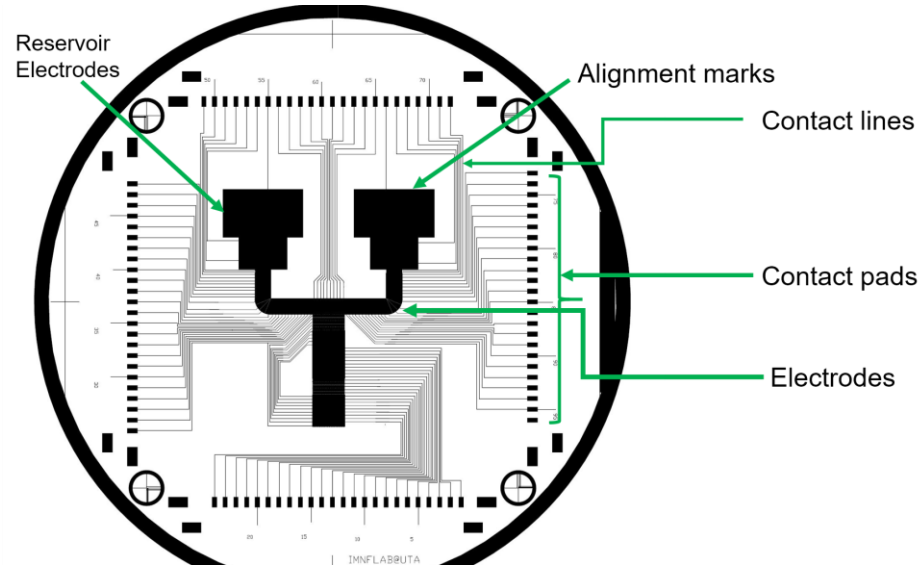

Figure 2-4 Pattern on the mask for the bottom chip.

program is used to send signals to the relay board to switch ON or OFF any particular electrode. The device assembly is presented in section 2.3.3.1.

2.3.2 Fabrication

The top and bottom chips of our device is fabricated in a cleanroom using standard photolithography, wet etching processes as shown in Fig. 2-5. Indium Tin Oxide ITO) or chromium coated glass substrate can be used as the top and bottom chip. The process starts with cleaning the wafer thoroughly with non-halogenated hydrocarbons: Acetone, Methanol, Isopropanol and then rinsing with DI water followed by a dehydration process at 150 ^{0}C for 5 minutes. For the bottom chip, at first HMDS is spin coated with the following recipe: speed of 500 rpm with a ramping rate of 100 rpm/s for 5 s; ramping with 900 rpm/s to 4000 rpm for 30s. The thin HMDS layer provides good adhesion between the ITO layer and the photoresist which will be deposited next. After the coating,

the wafer is baked at 150^0 C for 3 minutes. Next, a positive PR (Microchem S1813) is spin coated on the wafer with following recipe; spin speed of 500 rpm with ramping rate of 100 rpm/s for 5s; ramping with 900 rpm/s to 3000 rpm for 30s. This results in a uniform 1.2 μm thick PR layer. The glass substrate with the coated PR layer is then baked at 120 ^{0}C for 2 minutes. The PR is then exposed to UV light with a dose of 140 mJ/cm^2 on the Backside-Aligner (OAI 806MBA) followed by a baking step at 115 ^{0}C for 1 minute 30 s. After that, the wafer is dipped in a developer (Microchem, MF-319) bath for 1 minute and then rinsed thoroughly with water and dehydrated. The resulted electrode pattern is checked under the microscope for accuracy. The wafer is then dipped in a mixture of Hydrochloric (HCL) acid, Nitric (HNO_3) acid and DI water (H_2O) (wt %- 20% HCl, 5% HNO_3, 75% H_2O or vol %- 8:1:15, HCl: HNO_3: H_2O) for 2.5 minutes at 55 ^{0}C to etch the conductive layer. After removing the PR layer with PR stripping solution (Remover 1165, Microchem), the wafer is dehydrated at 150 ^{0}C for 5 min. Next, to provide an insulation layer, a dielectric material (SU-8-5, Microchem) is spin coated on the wafer with following recipe; spin speed of 500 rpm with a ramping rate of 100 rpm/s for 5s; spin speed of 2000 rpm with a ramping rate of 900 rpm/s for 30s) resulting in a 5 μm thick uniform dielectric layer. It is then baked to harden the layer at 65 ^{0}C for 1 minute and then 95 ^{0}C for 3 minutes. For hardening the layer, it is exposed to UV light with a light dose of 140 mJ/cm^2 on the Backside-Aligner (OAI 806MBA). The wafer is then soft baked at 65 ^{0}C for 1 minute, 95 ^{0}C for 1 minute and hard baked at 150 ^{0}C for 5 minutes. A hydrophobic layer is then created by spin coating a 300 nm thick uniform Teflon layer with the following recipe: spin speed of 1000 rpm with a ramping rate of 300 rpm/s for 30s. For the top chip, an ITO coated cover plate is first cleaned thoroughly with non-halogenated hydrocarbons: Acetone, Methanol, Isopropanol and then rinsed with DI water. It is then dehydrated at

150 ^{0}C for 5 minutes. A 300 nm thick Teflon layer is deposited using the same recipe described before.

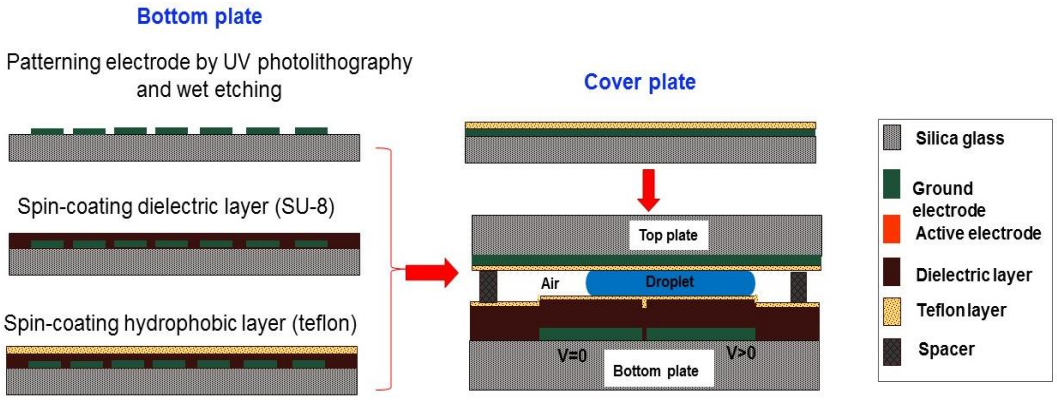

Figure 2-5 Process steps for fabricating EWOD device.

2.3.3 Experimental Setup

2.3.3.1 Device Assembly

The complete device assembly consists of a PCB board, a plexiglass holder, the EWOD bottom and top chip, four z-directional conducting strips as shown in Fig. 2-6. The EWOD bottom chip is attached to the plexiglass holder using tape. Small strips of Kapton tape (DuPont™ Kapton® HN polyimide film) are attached to the bottom chip to create the gap with the top chip. To accommodate the z-directional conducting strips, the plexiglass holder has via holes to hold them and make connection between the switches on the PCB board and the contact pads located on the bottom chip. Before doing the experiments, the reservoir is filled with the desired liquid and the top plate is placed on the Kapton tape strips therefore sandwiching the liquid between top and bottom chip. Finally, the assembly is connected to the switching circuit via data cables.

2.3.3.2 Device Control Flow

Figure 2-7 shows the control flow of the experimental setup. Firstly, the assembled device is connected to the relay board. Through a customized LABVIEW

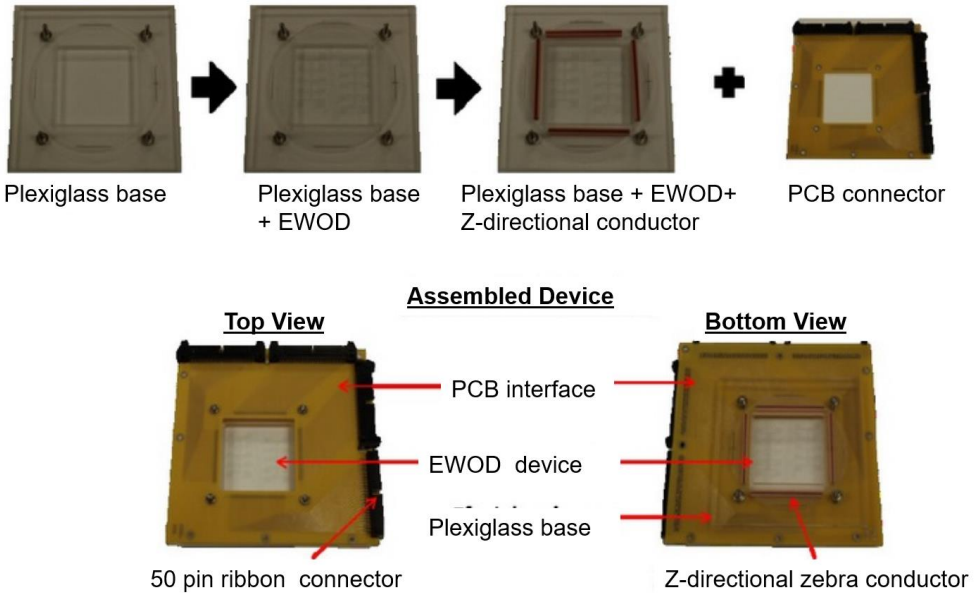

Figure 2-6 Device assembly.

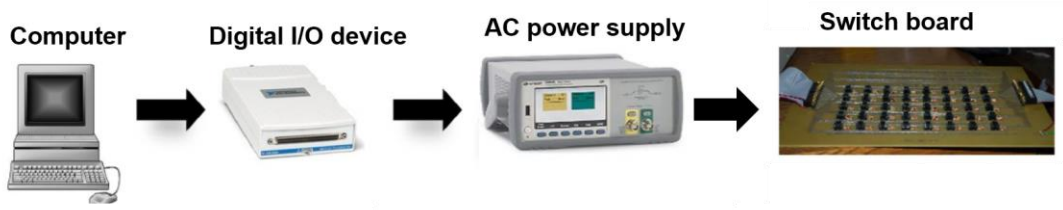

Figure 2-7 Device control flow.

program, instructions for switching the electrodes are sent to the switches. A voltage of 5V or 0V is supplied to each switch when the signal for switching on or off is sent from the computer through the Input /Output device and I/O connector accordingly. The

electrodes corresponding to a particular switch will be activated or deactivated according to the on or off status of the switches. A power source and voltage amplifier are used to amplify the supplied potential as shown in Fig. 2-7. A multimeter is also used to continuously monitor the applied voltage.

Chapter 3

Study of Droplet Velocity

In EWOD, a series of electrodes are activated in a timed manner and a discrete droplet is actuated along these sequentially 'fired' electrodes. The nature of the net electrostatic force on the droplet is not constant while a constant voltage is applied, because the actuation force depends on the dynamic shape of the droplet which keeps changing due to deformation during transition from the grounded electrode to the activated one [6]. Therefore, in practical cases, the velocity field of a droplet varies with time during its transition. In order to fully understand EWOD actuation, we need to study a complex unsteady problem. In some lab-on-a-chip devices utilizing EWOD, droplet speed needs to be maximized to enhance performance [27, 28-30]. For achieving maximum droplet speed, it is necessary to identify the parameters to favorably tune the basic forces of the system to indirectly control the speed. Some parameters such as liquid surface energy [33, 34], liquid viscosity [32], contact angle hysteresis [34], contact line friction [33, 34], dimensions [35, 36, 37] and shape of electrodes [38, 39, 40] droplet shape [38], gap between electrodes [35, 37] and the channel height [40] have been investigated numerically [37-42] and experimentally [40].

As already discussed, controlling droplet speed may become very crucial in many of the EWOD applications towards achieving the optimum device performance. However, to our best knowledge, among the studies already mentioned, none presented specific guidelines to accurately characterize and measure droplet speed. For example, in [35, 36], the droplet velocity was measured in terms of the switching speed - the distance travelled by a droplet during one switching period. However, this measurement method carries serious error unless switching time is carefully controlled so that a droplet does not sit idly during a switching period. Therefore, a proper characterization of

switching time is required to estimate droplet velocity accurately [41]. It becomes very important since unlike in droplet motion in micro-channels where the pressure drop is kept regular, droplet motion in EWOD device is very discrete, periodic, and unsteady in nature because of repetition of voltage on and off. Therefore, our primary goal of this study was to establish a practical characterization method for droplet speed. Majority of previous studies in droplet velocities in an EWOD device have been focused in numerical studies and parameters that may have intrinsic restrictions in practical applications. Much less numbers of experimental studies have been reported regarding droplet speed in an EWOD device. Since electrode design is a convenient parameter to implement in any kind of practical application, we studied droplet velocity in an EWOD device with new electrode designs. In addition, we studied the effects of electrode operation sequence on droplet velocity. The main objectives of this study are the following:

a) Characterization of velocity measurement
b) Measure droplet velocity from a novel electrode design and operation sequence
c) Compare velocity enhancement and validate experimental results with theoretical modeling

3.1 Experiments

3.1.1 Novel Electrode Design and Operation Sequence

According to the rigid body model considered by Chatterjee et al [42], Bahadur and Garimella [38], both the droplet actuation force and the opposing forces during motion influence the droplet dynamics which depend on the shape of the droplet base area (i.e. contact area or footprint area). For example, average actuation force for a droplet with rectangular contact area will be greater than that of a droplet with circular

contact area. In case of a dynamic droplet, the shape itself is affected by the deformation the droplet undergoes and eventually it affects droplet velocity [33, 34]. We will later show in this study that droplet deformation can be controlled by designing and operating the electrodes in a certain way. Beforehand, droplet deformation will be briefly explained.

3.1.2 Droplet Deformation

According to Berthier et al. [43], electrowetting force always acts normally to the droplet meniscus in an outward direction, whereas dewetting force acts in an inward direction which is also normal to meniscus. Electrowetting and dewetting force per unit length of the meniscus can be expressed as followed:

$$f_{ew} = \gamma \ \cos\theta(V) \ \ and \ f_{dew} = \gamma \ \cos\theta(0) \tag{3.1}$$

where, γ is the liquid-gas interfacial tension, $\theta(V)$ is the contact angle corresponding to an applied voltage V, and θ (0) is the contact angle corresponding to a zero applied voltage. Figure 6 illustrates a dynamic droplet at an instant when the droplet partially wets an actuated ($V > 0$ applied) electrode and a grounded ($V = 0$) electrode. As shown in Fig. 3-1, electrowetting force on the leading meniscus tries to spread the droplet towards the electrode edges. At the same time, dewetting force acting on the receding meniscus tries to pull the meniscus in an inward direction. Special attention should be paid to the interface between actuated and grounded electrodes. In the grounded side of the interface, opposing dewetting forces squeeze part of the droplet inward (i.e. yellow arrows in Fig.3-1). On the other hand, in the actuated side of the interface, electrowetting forces let the meniscus spread outward (i.e. green arrows in Fig. 3-1). As a result, a neck is formed at the interface and a head and a tail are formed in a dynamic droplet. If a very high voltage is applied, the velocity of wetting meniscus is very high and the droplet may split into two. It is worth mentioning that the above explanation about deformation does

not take into account several important factors such as contact angle hysteresis, viscous, and shear effects. Our explanation of capillary line forces acting on the three phase contact line can explain deformation of the droplet footprint (base area of droplet on top and bottom surfaces) only, in terms of x-y curvature change. But EWOD droplet motion is a three dimensional phenomena and to get the complete picture of deformation, it might be necessary to consider the z-directional curvature change which might be affected by shear or contact angle hysteresis. However, since capillary number in the present study is less than one ($Ca \sim 4\times10^{-4} \ll 1$), deformation is mainly governed by the capillary forces and viscous effects may be neglected. Therefore, a 2-D model can predict the droplet deformation well enough. Also, for our present purpose, we are more interested in exploiting the idea of manipulating the capillary forces to enhance droplet motion.

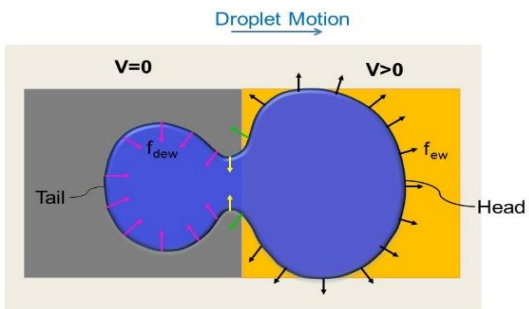

Figure 3-1 Droplet during transition from a grounded electrode to an activated one (Top view). Electrowetting force, f_{ew} (black arrows) and dewetting force, f_{dew} (pink arrows) on triple point contact line are shown.

As we can see from Fig. 3-1, if most of the meniscus remains on activated electrode, there will not be any neck formation and droplet meniscus will be pulled outward thus trying to overlap the hydrophilic surface of the activated electrode. Therefore, the droplet will manage to have almost a rectangular shape similar to the

shape of the activated electrode beneath it. According to the study by Bahadur and Garimella [38], this rectangular shaped droplet can theoretically give the maximum droplet velocity.

While keeping the above discussion in mind, we can assume that, electrode geometry can significantly affect droplet deformation. Having larger electrode widths has been found to cause more elongation where the droplet needs to travel same distance as the width of the activated electrode [44]. Conventionally, at the beginning of this transition, the droplet remains completely on a grounded hydrophobic surface. In our study, we tried to decrease the transition distance or the effective electrode width to reduce deformation. An array of slender electrodes was introduced for this purpose. In addition, different electrode operating schemes were tested to let a part of the droplet meniscus have wetting forces even in the beginning of the transition to obtain an almost rectangular shaped droplet profile to achieve a higher velocity.

3.1.3 Actuation Force as a Function of Transition Distance

According to the electromechanical model adopted by Bahadur and Garimella [38], actuation force for EWOD depends on the droplet shape as shown in Fig. 3-2. Square shaped droplet can have the maximum EWOD force and it is constant. Whereas, for circular or elliptical droplets, actuation force varies with the transition distance. Based on this we proposed a new electrode actuation method which can control the droplet shape as well as transition distance.

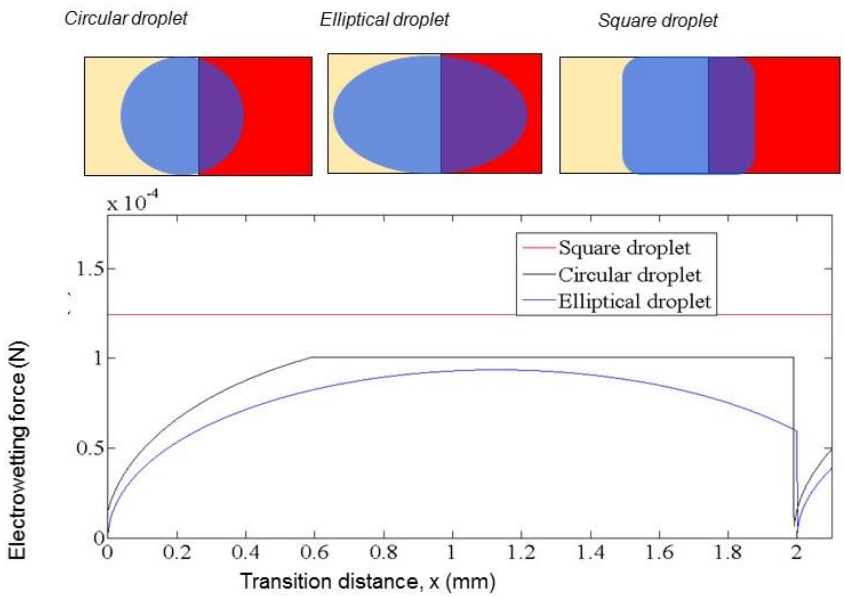

Figure 3-2 Actuation force as a function of transition distance for square, circular and elliptical shaped droplets.

3.1.4 Electrode Design and Operation Sequence

In order to achieve a higher velocity for a given voltage, we proposed of using an array of slender rectangular shape electrodes. The dimension of each electrode is 2 mm x 0.4 mm (Fig. 3-3(b) – 3-3(e)). For comparison purpose, we also fabricated square electrodes with the same length and width (2 mm × 2 mm) (Fig. 3-3 (a)). Further, in the case of slender rectangular electrodes, the number of simultaneously activated electrodes was varied to create variation in the initial actuation force and also to expose the droplet interface to different amount of electrowetting and dewetting forces at different locations in order to have different dynamic droplet shapes. Four different operation schemes were studied as shown in Fig. 3-3(b) – 3-3(e). The first scheme is named as 'S_L2'. 'S_L' refers slender electrodes and the '2' indicates two electrodes being activated

simultaneously. In this scheme, during each switching time, two strips of slender electrodes are activated. At the beginning of each switching time period, the droplet keeps in contact with one activated and four non-activated electrodes. So the total length of activated electrode is two electrodes width or 0.8 mm and total transition distance is one electrode width or 0.4 mm during each switching time period. Other sequences can be explained and named in the same manner in which total numbers of activated electrodes are varied but the transition distance is kept constant. In these cases, transition distance refers to the distance travelled during one switching time period.

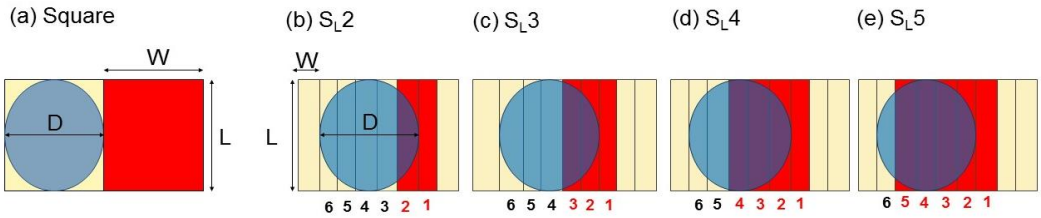

Figure 3-3 Schematic top view of : (a) Square electrode (b)-(e) Slender electrodes with various electrode operation schemes. L, W and D denote electrode length, width and droplet diameter, respectively. Red colored areas represent the activated electrodes.

3.1.5 Fabrication of EWOD Devices

The device fabrication recipe for the tests is similar to the one discussed in section 2.3.2. For this particular study, ITO electrodes were fabricated with the recipe described in chapter 2.

3.1.6 Test, Data Acquisition and Analysis

To test different designs of devices, a 400 nl of DI water droplet was placed in a device. The gap between top and bottom plates of the devices was kept at 100 μm. The droplet motion was recorded using a high-speed camera (Model: Miro M310, Vision

Research; frame rate: 1000 fps; resolution: 512 x 480) and later analyzed using Phantom CineViewer software. Details of velocity measurement are described in the next section [11].

3.1.7 Characterization: Defining Droplet Velocity and Minimum Switching Time

Since the aim of present study is to propose new electrode geometry to obtain faster droplet motion, it is necessary to have a clear definition of velocity that can be suitably measured in practical settings for comparison purpose. One definition found in other references is a 'switching speed' [35, 39]. A switching speed (v_s) is defined as the distance travelled during a switching period. One limitation of this definition is that v_s does not necessarily gives us the true speed during the transition because the droplet may actually complete its travel in much shorter time than the imposed switching period and sits idly during the remaining time of the period until the next electrode is activated. This means that droplet's true speed can be much faster than v_s. Therefore, it is important to control the switching time correctly. If our interest is to achieve the maximum speed for a given set of parameters including voltage, we need to set the minimum switching time (t_{min}) to activate electrodes so that the electrode next on the travel path of the droplet would be activated as soon as the droplet has completely moved onto current electrode. In this way, droplet motion will be continuous without any significant interruption and v_s will become close to the true speed of a moving droplet.

In this study, droplet velocity was measured experimentally. Figure 3-4 shows the parameters involved in the velocity measurement. A point on the droplet was first identified in a high-speed (1000 fps) camera images by analyzing frames. After every 50 frames for slender electrodes and 100 frames for square electrodes, the location of that particular point was identified and distance of the same point from the previous frame to the current frame was measured. Then the distance was divided by the time interval

between these two frames to obtain velocity of the particular point. Two points on the droplet were considered in droplet velocity calculation. The front most point on the droplet meniscus was designated as the droplet 'head (H)' and the back most point as the droplet 'tail (T)' (Fig. 3-4). For avoiding rigorous calculations, the average of head and tail velocities was considered as a rough estimation of the droplet velocity ($v_{droplet}$) of its horizontal motion:

$$\begin{aligned} v_{head}(t) &= \frac{\Delta H(t)}{\Delta t} \\ v_{tail}(t) &= \frac{\Delta T(t)}{\Delta t} \\ v_{droplet}(t) &= \frac{\{v_{head}(t) + v_{tail}(t)\}}{2} \end{aligned} \tag{3.2}$$

The time-average droplet velocity (v_{avg}) during the entire course of droplet travel will be:

$$v_{avg} = \frac{1}{t^*}\int_0^t v_{droplet}(t)dt \tag{3.3}$$

where, t^* is the time to reach the destination.

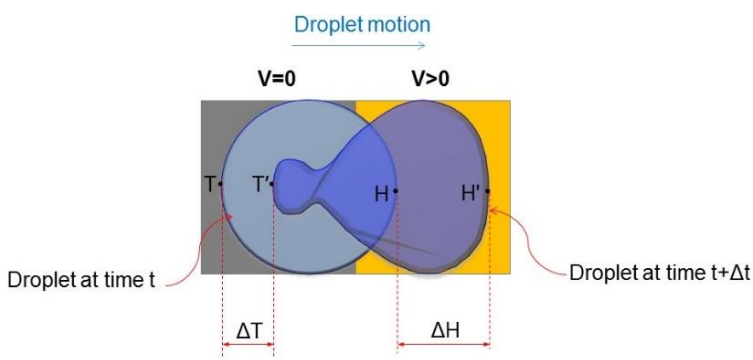

Figure 3-4 Measuring average velocity of a dynamic droplet. The droplet at left hand side represents a droplet at any time instant, t during transition from grounded electrode to activated electrode. The droplet at right hand side is the same droplet after time interval, Δt. T, T′, H, H′denotes two points designated as the droplet head and tail at these two different time instants, respectively. Orange colored surface is the activated electrode. ΔH and ΔT are the distances travelled by head and tail during Δt time, respectively.

3.2 Theoretical Model

3.2.1 Governing Equations for Rigid Body Model

Similar to the approach taken by [38], any deformation was neglected and the droplet was considered to behave like a rigid body. The droplet volume was same for each case and the droplet diameter was considered to be slightly larger than the electrode length. The droplet is considered as a single mass moving with EWOD actuation in an air medium. Any velocity or pressure distribution inside the droplet is neglected. The forces that oppose the motion are the drag force from air, shear caused by the top and bottom plates and the contact line friction force acting on the droplet meniscus at the solid substrate surface.

The actuation force is calculated according to electro-mechanical approach [38]. The reduced dielectric-liquid interfacial energies can be estimated from a capacitive circuit analysis where there are parallel plate capacitors arising in the dielectric layers as shown in Fig. 3-5(a). Here, d_1, d_2 are the top and bottom dielectric layer thicknesses, C_1, C_2 and C_3 are three capacitors. As in the most practical situations, where there is no top dielectric layer, the actuation force can be obtained using Eq. 3.4 as follows:

$$F_{EWOD}(\mathrm{x}) = \frac{k\varepsilon_o V^2}{2d}\frac{dA}{dx} \tag{3.4}$$

Where d is the dielectric thickness, k is the dielectric constant, V is the applied voltage, A is the overlapped area between the activated electrode and the droplet footprint on the surface. The details of this formulation can be found in reference [38].

One of the opposing forces is the drag produced by air medium. The force is derived for a cylindrical fluid body moving in a cross-flow field given by:

$$F_f = \left(\frac{1}{2}C\rho_f v^2\right)(2rd) \tag{3.5}$$

Here C is the drag coefficient, r is the radius, d is the height, and *v* is the velocity and ρ_f is air density.

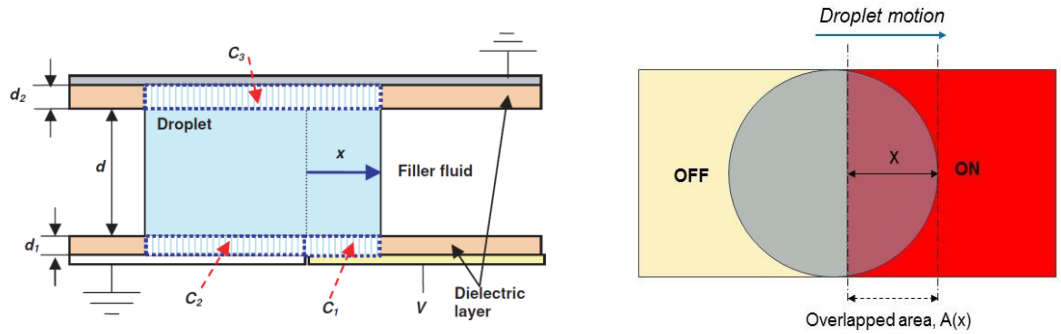

Shear

(a) (b)

Figure 3-5 (a) Schematic for calculating actuation force [28]. (b) Top view of droplet profile during motion

force is calculated with the assumption that no-slip conditions exist at the boundaries and a parabolic profile inside the droplet. The equation is thus:

$$F_w = \left(\frac{6\mu_1 v}{d}\right)(2\pi r^2) \tag{3.6}$$

Here, μ_1 is the dynamic viscosity.

Finally, the contact line friction is assumed to be a function of velocity similar to the approach taken by Ren et al. [34]:

$$\mathrm{F_{el}} = (\zeta \mathrm{v})(4\pi \mathrm{r}) \tag{3.7}$$

Here, friction co-efficient, ζ is an emiprical parameter.

The overall governing equation controlling droplet motion can be written as:

$$m\,\frac{d^2x}{dt^2} = F_{act} - F_{drag} - F_{shear} - F_{friction} \tag{3.8}$$

One modification was made before solving this equation. Instead of having a perfectly circular shaped droplet, a deformed droplet was considered as shown in the figure below. Each droplet was considered to comprise of an ellipse, a rectangle and a

half circle. The hydraulic radius from these approximations was calculated and used in the opposing force calculations in case of the radius, r. Finally, above equation was solved using MATLAB.

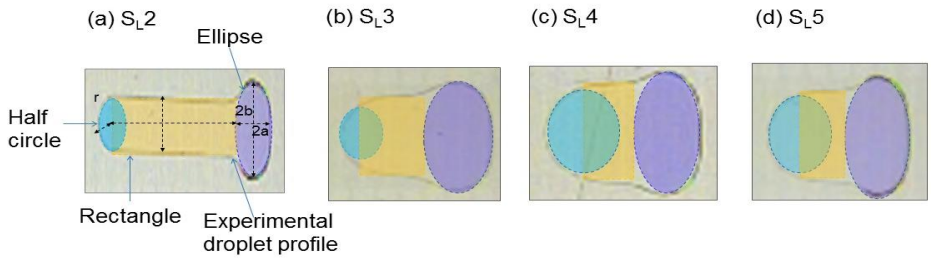

Figure 3-6 . (a-d) Approximate droplet shapes used for theoretical calculations of droplet motion on slender electrode arrays. For each sequence droplet footprint area consists of an elliptical front part (Shaded in violet), rectangular middle part (shaded in light orange) and half circular back part (Shaded in sky blue). Letters a, b denotes major and minor axis of the ellipse, L and W denotes length and width of the rectangle and r is the radius of the half circle.

3.3 Results and Discussion

3.3.1 Minimum Switching Time (t_{min})

Since t_{min} is unique for every case, different switching times were tested for a droplet to move over a distance of 16 mm. The smallest switching time for which the droplet could reach the destination without any interruption was considered as t_{min}. For switching times larger than t_{min}, the droplet completes motion earlier than the given time on each electrode and the motion is interrupted in each period. Whereas, if the switching times are smaller than t_{min}, the droplet would stop permanently after traveling some distance and will not travel further. This is because the droplet cannot complete its

transition over the current electrode and touch the next electrode within the switching time. The definition of switching speed using t_{min} (v_s = W/t_{min}) is close to the average droplet velocity (v_{avg}). It has to be noted that the resolution of switching time in our experiment was limited to 1 ms due to the facility capability. Therefore, it is probable that a droplet momentarily stops in each switching period before it starts moving again to the next electrode, which results in a slightly longer t_{min} measurement than it should be. So if we consider v_s to represent the droplet velocity, it can give slightly lower value of the best achievable speed. For an applied voltage of 150 V_{rms}, t_{min} for square electrode device was close to 100 ms. In the slender electrodes array device, t_{min} were 10 ms, 11 ms, 11 ms, and 10 ms for S_L2, S_L3, S_L4, and S_L5 schemes, respectively.

3.3.2 Droplet Velocity Measurement – Square Electrode

Droplet velocity ($v_{droplet}$) was measured as described in section 3.1.7. Figure 3-7(a) shows instantaneous velocity a droplet, $v_{droplet}$ on a square shaped electrode during t_{min} (≈ 100 ms). Droplet velocity gradually increases, reaches to the maximum value of 50 mm/s at the half period of transition and decreases gradually. The evolution of the droplet shape during t_{min} is shown in Fig. 3-7(b).

Initially, the droplet maintains a squared shape since the square electrode is turned on. Then around at 10 ms, it develops a neck along with a bulged head and tail and this shape continues to change until 30 ms. After 30 ms, there is no distinct neck and now the droplet starts to restore its initial shape. Finally, the deformation is very less between 70 and 100 ms. Note that, v_s and v_{avg} are the same for square electrodes case and it is because a droplet deforms and restores its shape again within one switching period.

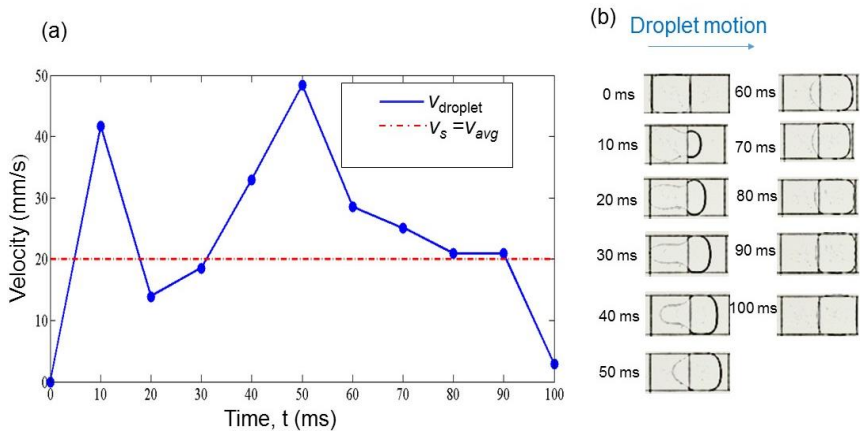

Figure 3-7 . (a) Droplet velocity profile on a square electrode during one switching period. Average velocity and switching speed (v_s) are equal and depicted in red dashed line. (b) Images of droplet shapes at different instants during t_{min} (= 100 ms) on a square electrode.

3.3.3 Droplet Velocity Measurement -Slender Electrodes

The droplet deformation patterns on slender electrodes are significantly different from the square electrodes case. Unlike the square electrodes case, a droplet does not restore its shape within one switching time, but continuously deforms while it transits over several electrodes until it reaches a certain amount of deformation. As a primitive indicator of deformation, the elongation of a droplet in the direction of motion was considered. By analyzing frames extracted from high-speed videos, the elongation at different frames was measured. The relative elongation with respect to the initial dimension of the droplet (for S_L2 scheme) was plotted in Fig. 3-8. When the switching time is almost equal to t_{min}, after the initial continuous deformation, the droplet stops deforming and continues to move with the final deformed shape. We call the initial distance having continuous deformation as the 'transition region' and the latter with no

further deformation as the ‘constant shape region’. The time to reach the constant shape region is transition time (τ). Droplet velocity, $v_{droplet}$ sharply increases during the transition region and reaches to a final value (final velocity, v_f) once it arrives in the constant shape region and maintains it till the destination (Fig. 3-8). As shown in the figure, a droplet in S_L2 scheme deforms very little while it goes through the constant shape region. This is true for all other schemes.

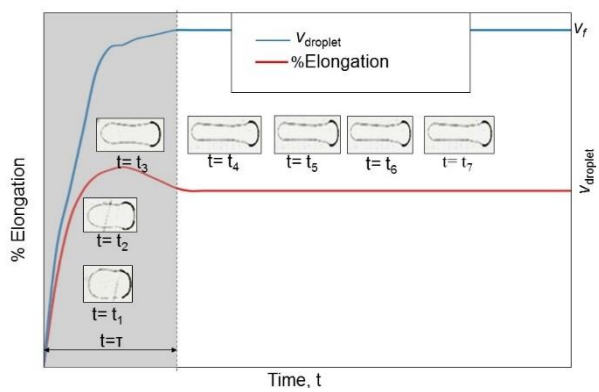

Figure 3-8 A representative droplet velocity ($v_{droplet}$) profile and % elongation vs. time for slender electrode arrays in SL_2 scheme. The shaded area represents the ‘transition region’ and the remaining area of the plot represents ‘constant shape region’. The inset photos show the droplet profiles at different instants of those two regimes.

The plots of $v_{droplet}$ in Fig. 3-9 give an overview of the droplet motion for different schemes of slender electrodes array. The inset photo of each plot is the droplet shape in the constant shape region. Firstly, $v_{droplet}$ tends to be less in the transition region than in the constant shape region due to significant deformations in the transition region. In present study, deformation is mainly controlled by operation schemes as discussed in section 3.1.4, which in turn controls the amount of actuation force. Scheme S_L2 provides the smallest part of the droplet circumference with the wetting force compared to the

other schemes and it is the opposite for S_L5. Hence, S_L2 has the greatest and S_L5 has the least elongation. Interestingly, S_L2 has the longest transition time, τ of ~300 ms. (Fig. 3-9). For S_L2 scheme, v_{avg} is 36.48 mm/s, while its final velocity (v_f) is 40 mm/s. If the droplet moves much longer distance in the constant shape region so that $t^* >> \tau$, v_{avg} will be as high as the final velocity (= 40 mm/s) which is almost twice of v_{avg} of the square electrodes case. For S_L3 (Fig. 3-9(b)), the elongation and τ are smaller than those of S_L2. The v_{avg} is 35.02 mm/s and the v_f is 36 mm/s. For S_L4, τ is almost same as that of S_L3 because the elongation of those two schemes is similar (Fig. 3-9(c)). Although S_L4 has the same v_f as that of S_L3, lower velocity during τ limits its v_{avg} over the 400 ms period to be 33.02 mm/s. The highest v_{avg} of 36.60 mm/s is observed in S_L5 (Fig. 3-9(d)). Similar to S_L2, v_f of S_L5 is about 40 mm/s but since τ in the case of S_L5 is smaller, its v_{avg} over the 400 ms is larger (36.6 mm/s). It is noted that the elongation in S_L5 is the smallest. Although we assumed the droplet did not deform in the latter part of the transition, in fact, there was minute instantaneous deformation which is random in nature depending on the local variations in the surface conditions. We neglected it as a significant factor to control droplet deformation. Table 3-1 below provides a summary of the experimental results for square as well as four different cases of slender electrodes.

To explain the reasons for getting higher v_{avg} for slender electrodes than for square electrodes, the first assumption made earlier in section 3.1.3 can be recalled here. We know that the actuation force in EWOD is a function of transition distance and the maximum actuation force can be achieved by operating the electrodes in a certain way as we did in case of the slender electrodes. EWOD actuation force will vary by droplet shape because of different gradients in overlapped area (dA(x)/dx), which is generally function of transition distance unless droplet is in a square shape [38]. As discussed in section Using MATLAB and the theoretical formulations based on a rigid

body model, we calculated the actuation force for a circular droplet for all of the experimental cases. Any deformation was neglected and the droplet was considered to behave like a rigid body. The droplet volume was same for each case and the droplet diameter was considered to be slightly larger than the electrode length. For the total actuation force calculation, we used area integral in MATLAB during a transition time of 35.67 ms for which a droplet travels 2 mm in a square electrode device. In the same period of time, droplets for other sequences experience different travelling distances. For example, in S_L5, a droplet completes more than five transitions equivalent to more than 2 mm (5 × 0.4 mm). Then, by assuming time averaged actuation force, we could roughly compare the actuation forces of different sequences. This is tabulated in Table 3-2.

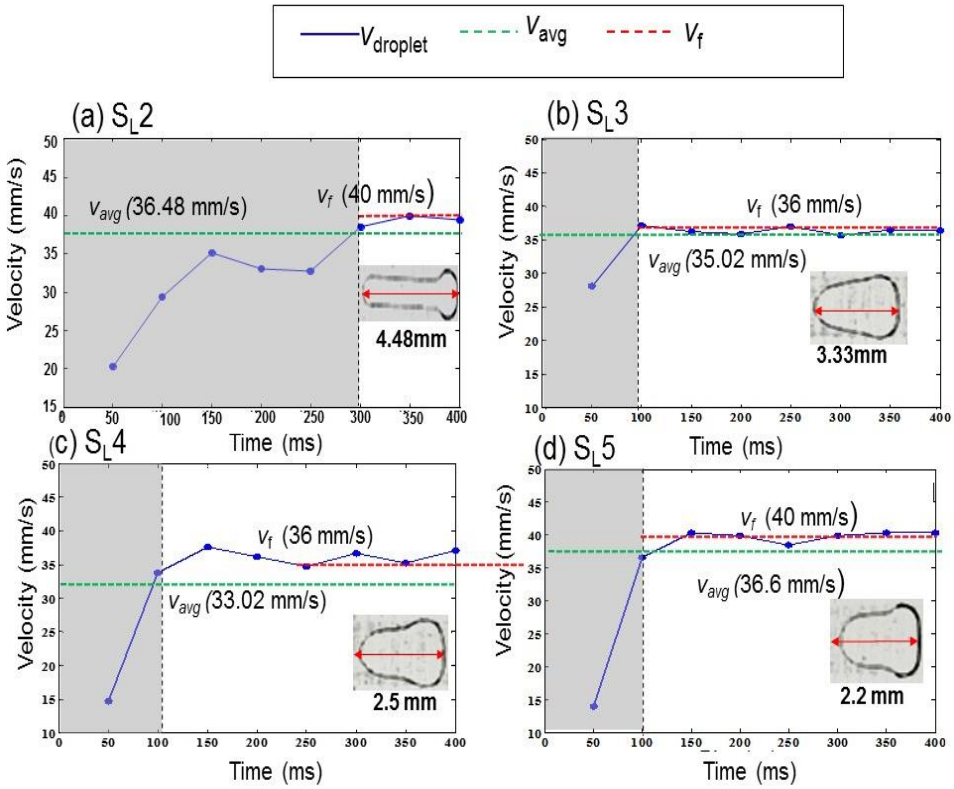

Figure 3-9 . Experimental droplet velocity profiles for slender electrode arrays. The insets show droplet shapes during constant deformation. The shaded regions on the plots depict the transition regions.

Table 3-1 Summary of Experimental Results.

	Minimum Switching time, t_{min} (ms)	**%Elongation**	**Transition time, τ (ms)**	**Final velocity, v_f (mm/s)**	**Average veloctiy, v_{avg} (mm/s)**
Square	97	–	–	–	20
S_L2	10	124	300	40	36.48
S_L3	11	25	100	36	35.02
S_L4	11	16.5	100	35.5	36.60
S_L5	10	10	100	40	33.02

Table 3-2 Percentage increase in actuation force of slender electrode sequences with respect to a square electrode

Operation sequence	**% increase in actuation force**
S_L2	16
S_L3	32
S_L4	29
S_L5	6

As seen in Table 3-1, all of the sequences of slender electrodes show higher time averaged actuation force in the given time period than the square electrode case. When the droplet starts to move, it has different overlapped area for square and also different schemes for slender electrodes. Compared to the square electrode case, the

initial actuation force for slender electrodes is much higher. In addition, since it transits only 0.4 mm (one electrode strip distance) during each transition, the overlapped area of droplet with the activated electrode changes very little during this time and so does the actuation force. If the droplet moves 2 mm distance, it will have the repetitive actuation force profiles corresponding to each switching period which happens several times as opposed to the parabolic profile of square electrode as shown in Fig. 3-10. When we calculate the time averaged actuation force for both cases, in general, we will always get higher actuation force as well as higher average velocity for slender electrodes which we derived from the experiments. One limitation of this theoretical calculation is that t_{min} for square electrode from this modeling (= 35.67 ms) is almost three times shorter than t_{min} from experiment (≈ 100 ms), which indicates an overestimated actuation force or underestimated opposing forces that we predicted using this model. This difference is due to the fact that for square electrode, droplet deformation was not considered in area calculation and was considered as perfectly circular. On the other hand, it is confirmed that, droplet deformation is negligible within constant shape region of S_L schemes although they are not necessarily circular or exactly square shaped.

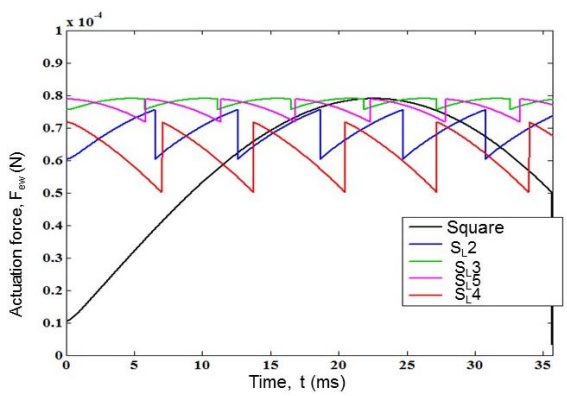

Figure 3-10 Actuation force (Few) with time on a circular droplet for various electrode operation schemes (Rigid body model).

By solving Eq. 3.8, actuation force, average velocity (v_{avg}) and minimum switching time (t_{min}) were calculated for the slender electrodes using the rigid body model. The estimated switching times were 9.94 ms, 10.257 ms, 11.33 ms and 9.98 ms, for S_L2, S_L3, S_L4, and S_L5, respectively. The estimations by the rigid body model are very close to our experimental results as shown in Table 3-3. So we can safely use the rigid body model results to explain higher velocities for different schemes of slender electrodes.

Table 3-3 Comparison between theoretical calculation (rigid body model) and experimental results for slender electrodes

Operation sequence	**Actuation force (μN)**	**Theoretical average velocity, v_{avg} (mm/s)**	**Experimental final velocity, v_f (mm/s)**	**Theoretical t_{min} (ms)**	**Experimental t_{min} (ms)**
S_L2	.575	41	40	9.94	10
S_L3	.563	40	36	10.257	11
S_L4	.4966	36.5	35.5	11.33	11
S_L5	.546	41	40	9.98	10

Now since the theoretical calculations give almost similar t_{min}, the velocity results should also be similar. As we can see in Fig. 3-11(a), the average velocity profiles for all the cases are different from each other depending on the shape of the contact area of the droplet with electrode. The time averaged velocity, v_{avg} calculated from the velocity plots in Fig. 3-11(a) shows very close match to the final velocities (v_f) observed in the experiments (Table 3-3). During the transport of the droplet over a distance of 2 mm, the theoretical time averaged velocity for S_L5 and S_L2 is maximum which is 41 mm/s

compared to an average velocity of 40 mm/s for S_L3 and 36.5 mm/s for S_L4. In experiments, we also get maximum average velocities for sequences, S_L2 and S_L5 with velocity averaging to about 40 mm/s in the constant deformation regions. For the other two sequences, the average is about 36 mm/s once the droplet travels beyond the constant shape region. So after modifying the droplet shapes, the rigid body model can predict the results acceptably well for the slender electrodes. The minute deviation from the experimental results is due to the difference between the approximated droplet shape from the actual droplet shape and also to the slight changes in shape during the motion in each switching period in the experiments that was neglected for simplicity in the theoretical calculation.

Next, time averaged actuation force is calculated and shown in Fig. 3-11(b) and also tabulated in Table 3-3. In general, the time averaged actuation force is higher for the sequence giving higher velocity except for S_L5 which gives less actuation force than S_L2 and S_L3 but has higher velocity than the two. This may be due to the fact that there might be some errors in the theoretical calculation resulting from both instantaneous deformations which we neglected and also inaccuracy in shape estimation during modeling. One observation is that the actuation force profiles are similar to the velocity profiles in Fig. 3-11(a). This means, if the droplet shape is constant or deformation is very less, droplet velocity is mainly governed by the actuation force which has been previously found in literature [33].

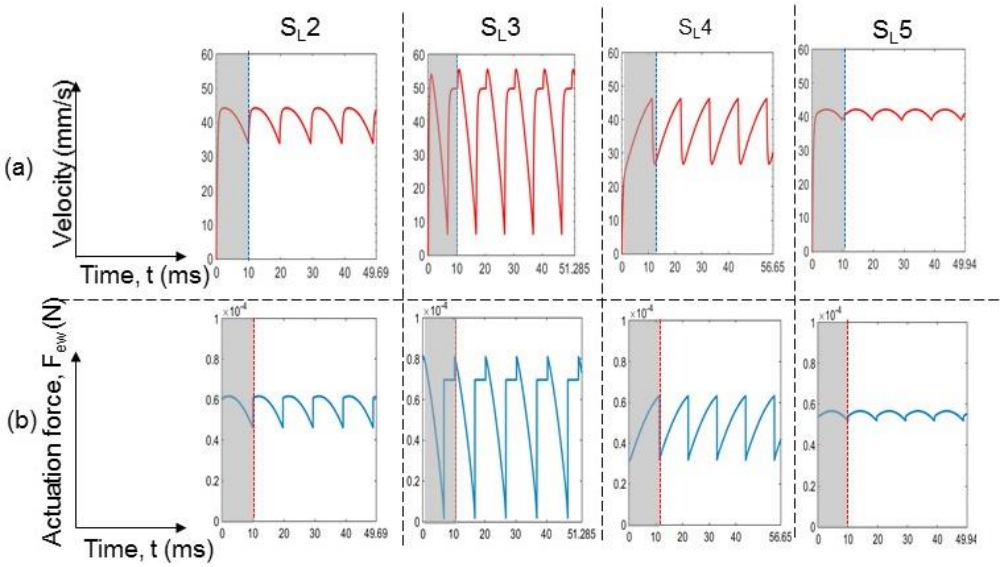

Figure 3-11 Theoretical (a) Velocity profiles and (b) actuation force vs. time, for all of the cases of slender electrodes during transition over 2 mm distance. The shaded regions correspond to one switching period for each case.

3.4 Conclusion

In this study, a new design of electrode geometry has been proposed and two times of velocity enhancement compared to the conventional square shaped electrodes have been demonstrated. The result has been validated and explained using theoretical modeling. Also, experimental protocols regarding controlling switching time for gaining optimum velocity has been discussed. Additionally, more practical definition for measuring droplet velocity has been presented.

Chapter 4

Three-Dimensional Numerical Modeling of Electrowetting on Dielectric Droplet Motion

4.1 Introduction

In recent years, the field of digital microfluidics have attracted many researchers in which discrete droplets are used instead of having continuous flows of liquid because of many of the advantages already discussed [45]. The use of multiple droplets acting like small microreactors offers an additional benefit besides portability and minimal operation cost due to miniaturization. As each droplet is spatially confined, a large number of experiments can be performed on a single chip surface giving rise to increased possibilities in multiplexing. In particular, efficient and cost-effective lab-on-a-chip devices are in great demand, as they allow for highly repetitive laboratory tasks to become automated with the introduction of miniaturized and integrated systems [46]. In many of the digital microfluidic applications [27, 29, 30], controlling droplet speed is crucial. For this reason, we studied dynamics of droplet motion using experimental tools. We developed a complete set of guidelines for measuring velocity and in order to have a better understanding of the physics of the motion, we developed a theoretical model as well. The model could support our experimental findings and explain certain behavior of moving droplets for a set of parameters. However, there was some limitations of the model. First of all, droplet deformation was neglected which is in actual scenario, is a critical aspect of motion dynamics. Secondly, droplet velocity was measured considering only three points inside the fluid body and was considered to be uniform throughout the rigid body which is very different in real situations. Electrowetting force acts non-uniformly on the droplet meniscus which results in different velocities at different locations in the droplet. Thirdly, pressure and velocity are two important parameters in any fluid motion which were not measurable using the theoretical modeling or experimental tools. All of

these limitations can be overcome if we have a numerical model of EWOD droplet motion. Therefore, our objective of this study is to:

- Develop a numerical model of EWOD droplet motion using Finite Element Method

4.2 Theory

4.2.1 EWOD Actuation

EWOD principle has been already discussed in section 2.1. Here only the actuation principle for droplet transport will be discussed. One way to express the net EWOD force is in terms of Laplace pressure difference (see EWOD schematic in Fig. 4-1). If a droplet of conductive liquid is placed partially on an activated electrode (V>0), the asymmetric radius of curvature of the droplet meniscus resulting from the different contact angles on trailing and leading meniscus of the droplet will create pressure difference on two sides of the droplets which can be realized from Young-Laplace equation [47, 48]:

$$\Delta P = \sigma \left[\frac{\cos\theta_{on} - \cos\theta_{off}}{h} + K_{xy}(off) - K_{xy}(on) \right] \tag{4.1}$$

Where K_{xy} is the curvature of the droplet on xy plane and h is the channel height for a parallel plate EWOD setup. Now this pressure difference will create a net driving force which will move the droplet.

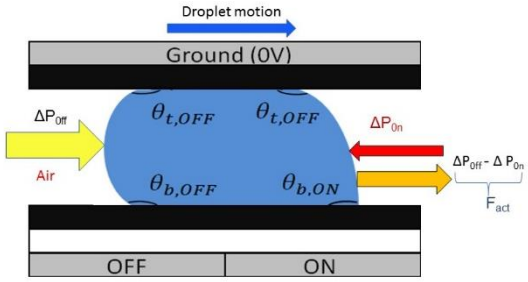

Figure 4-1 Schematic for EWOD droplet actuation. ΔP is the Laplace pressure difference between advancing and receding menisci on activated and deactivated electrodes.

In this definition, electrowetting effects are considered to change the droplet morphology which results in contact angle and change in the radius of curvature locally. This leads to the disruption of the initial equilibrium and forces the droplet to move until it finds the new equilibrium which the droplet basically does when it reaches to the edge of an activated electrode. Some of the numerical studies performed on EWOD droplet motion have used this description of electrowetting actuation [48, 49] and we will follow the same principle in our model setup.

4.3 Problem setup

Figure 4-2 illustrates the problem setup for our study. A rectangular region filled with air was considered to be the fluid flow domain which also contained a sandwiched water droplet. Two square shaped surfaces next to each other on the bottom plate were designed as the transporting electrodes. The initial droplet was sitting on one of the electrodes while touching the edge of the target electrode. Since the channel height is very small (100µm), the z-directional curvature of the initial droplet was neglected and the initial droplet was considered to be cylindrical. Also, since we are incorporating the effects of electrowetting through the change in contact angle for an applied voltage, we decoupled electrostatics from our problem and the problem became solely a fluid flow problem.

The following geometrical parameters were used for modeling and are listed in table 4-1:

Table 4-1 Geometric dimensions

Parameter name	**Dimension (mm)**
Electrode dimension	2×2
Channel height	0.1
Droplet diameter	2

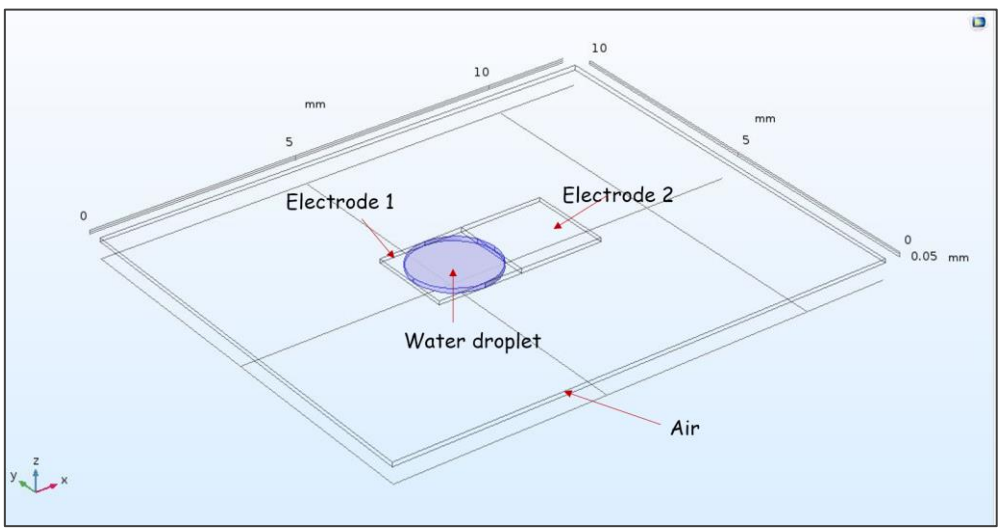

Figure 4-2 Geometry of droplet flow model.

4.4 Solving with COMSOL Multiphysics

COMSOL Multiphysics is a simulation software which uses Finite Element Methods to solve various physical phenomena numerically. COMSOL Multiphysics 5.0 was used to solve the problem described in section 4.3. To shorten the computational time and reduce computational resources, electrowetting effect in the fluid flow dynamics

was directly introduced through Young-Lippman equation (Eq. 4.1). The fluid flow physics was therefore decoupled from the electrostatics. For solving the fluid flow dynamics, both Two-Phase Flow, Phase Field and Two-Phase Flow, Level Set methods were used.

4.4.1 Governing equations

For solving the velocity and pressure field in the fluid domain, continuity (Eq. 4.3) and momentum (Eq. 5.4) equations have been solved assuming incompressible, constant property two phase flow:

$$\nabla . u = 0 \tag{4.3}$$

$$\rho\left(\frac{\partial u}{\partial t}\right) + (u.\nabla)u = \nabla.[-\mathrm{PI} + \mu(\nabla \mathrm{u} + (\nabla \mathrm{u})^{\mathrm{T}})] + \rho g + \mathrm{Fst} \tag{4.4}$$

Here, ρ is the density of fluid, u is the velocity vector, μ is the fluid dynamic viscosity, t is time, P is fluid pressure, g is the gravitational acceleration, Fst is the surface tension force and I is the identity matrix [48]. Further surface tension force Fst is defined as non-zero only at the interface using the following expression:

$$Fst = \Delta.\sigma(I - (nn)^T)\delta \tag{4.5}$$

Where σ, I, n and δ represents co-efficient of surface tension, interface normal, identity matrix and direct delta function respectively.

Next to track the interface of the two immiscible fluids, advection equations of the respective functions (e.g. phase field variable or level set variable) should also be solved along with the Navier-Stokes equations.

4.4.2 Convection of the interface

4.4.2.1 Phase field method:

In the phase field method, the two-phase interface dynamics is solved by using Cahn-Hilliard equation [50, 51]. The equation tracks a diffused interface separating the two phases. In the interface, the dimensionless phase field variable, ϕ goes from −1 to 1. For the two phases involved, the function takes the value of less than or greater than 1 as depicted in Fig. 4-3.

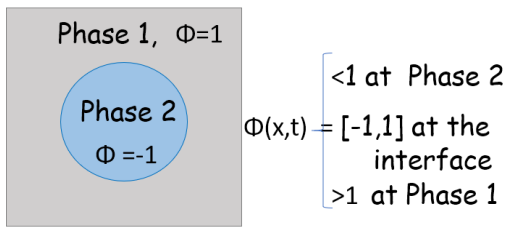

Figure 4-3 Variation of phase field variable, ϕ.

When solved in COMSOL Multiphysics, the Cahn-Hilliard equation is split up into two equations:

$$\frac{\partial \phi}{\partial t} + u.\nabla\phi = \Delta.\frac{\gamma\lambda}{\varepsilon^2}\Delta\Psi \tag{4.5}$$

$$\Psi = -\Delta.\varepsilon^2\Delta\phi + (\phi^2 - 1)\,\phi \tag{4.6}$$

where u is the fluid velocity, γ is the mobility, λ is the mixing energy density and ε is the interface thickness parameter. The ψ variable is referred to as the phase field help variable. The following equation relates the mixing energy density and the interface thickness to the surface tension coefficient:

$$\sigma = \frac{2\sqrt{2}\lambda}{3\,\varepsilon} \tag{4.7}$$

Typically the interface thickness parameter is set to $\varepsilon = h_c/2$, where h_c is the characteristic mesh size in the interfacial region. The mobility tuning parameter, γ

determines the time scale of the Cahn-Hilliard diffusion and can be chosen according to the physical phenomena under consideration. It must be large enough to retain a constant interfacial thickness but small enough so that the convective terms are not overly damped. By default, it is taken as, $\gamma = \varepsilon^2$, as an initial guess.

In the phase field method, the volume fractions of the individual fluids are-

$$Vf1 = \frac{1-\phi}{2}, \qquad Vf2 = \frac{1+\phi}{2} \tag{4.8}$$

To smooth out any discontinuity across the interface, the multiphysics coupling feature modifies the density and the viscosity of the mixture as the following:

$$\rho = (\rho_{water} - \rho_{air}) \times \phi_{water} \ + \rho_{air} \tag{4.9}$$

$$\mu = (\mu_{water} - \mu_{air}) \times \emptyset_{water} \ + \mu_{air} \tag{4.10}$$

where the single phase water properties are denoted water and the air properties air.

4.4.2.2 Level set method

Level set method is a simple and versatile method for computing and analyzing the motion of an interface in two or three dimensions [51, 53]. It uses a continuous auxiliary function (level set function), ϕ, over the whole computational domain, and represents the interface as the zero level set of this higher dimensional function. The level set function can be coupled to Navier-stokes equations to be advected with a background flow field, thus propagating the interface exactly as the zero level set of ϕ.

If two phases comprise of water and air, the level set function can thus be thought of as the volume fraction of water. The transport of the fluid interface separating the two phases is given by-

$$\frac{\partial \emptyset}{\partial t} + u.\nabla\emptyset = \gamma\nabla.\left(\varepsilon\nabla\emptyset - \emptyset(1-\emptyset)\frac{\nabla\emptyset}{|\nabla\emptyset|}\right) \tag{4 .11}$$

Here, ε parameter determines the thickness of the interface. If any kind of stabilization technique is used for the level set equation, it is better to assume interface thickness, ε = $h_c/2$, where h_c is the characteristic mesh size in the region passed by the interface. A reinitialization step is performed to keep ϕ as a signed distance function near the interface while keeping the original zero level set unchanged. The γ parameter determines the amount of reinitialization. A suitable value for γ is the maximum velocity magnitude occurring in the problem.

In level set method, interface evolution is captured using the level set function, which is a signed distance function relative to the interface. evolving interface naturally; the position of the interface at time *t* is given by the zero level set ϕ (x, *t*) = 0 of the evolving level set function. This set does not need to be connected and can break and merge as *t* advances. Moreover geometrical quantities, such as the unit normal ***n*** and the curvature κ can be easily determined using the level set function ϕ

$$\mathbf{n} = \frac{\nabla\emptyset}{|\nabla\emptyset|} \tag{4.12}$$

The multiphysics coupling feature defines the density and viscosity according to:

$$\rho = (\rho_{water} - \rho_{air}) \times \emptyset_{water} + \rho_{air} \tag{4.13}$$

$$\mu = (\mu_{water} - \mu_{air}) \times \emptyset_{water} + \mu_{air} \tag{4.14}$$

4.4.3 Modeling surface tension force

In the level set interface, the surface tension force is treated as a body force and defined by the following equation:

$$Fst = \nabla.\mathbf{T} \tag{4.15}$$

$$\mathbf{T} = \sigma(\mathbf{I} - \boldsymbol{nn})^{\mathrm{T}}\boldsymbol{\delta} \tag{4.16}$$

Here, **I** is the identity matrix, **n** is the interface normal, σ is the surface tension coefficient (N/m), and δ is called the Dirac delta function that has zero values only at the fluid interface and has zeros everywhere else. When solving the Navier-Stokes equations, the above expression for surface tension has to be multiplied by a test operator and integrated over the computational domain. By integrating by parts, the derivatives of **T** can be moved to the test functions. This results in an integral over the computational domain plus a boundary integral of the form:

$$\int test(\boldsymbol{u}).[\sigma(\boldsymbol{n}) - (\boldsymbol{n}\cos\theta)\delta]\, dS = \pi r^2 \tag{4.18}$$

where θ is the contact angle. If a no slip boundary condition is applied, the boundary term vanishes because test(u) = 0 on that boundary, and contact angle cannot be specified. In that case, the interface will remain fixed on the wall. However, with the wetted wall condition, a small amount of slip is given to the wall and it is possible to specify the contact angle.

In the phase field method, the surface tension is computed using Eq. (4.18):

$$\mathrm{F_{ST}} = \mathrm{G}\nabla\emptyset \tag{4.19}$$

Where ∅ is the phase field parameter, and G is the chemical potential, where it is expressed by the following equation:

$$G = \lambda\left[-\nabla^2\emptyset + \frac{\emptyset(\emptyset^2-1)}{\varepsilon^2}\right] = \frac{\lambda}{\varepsilon^2}\Psi \tag{4.20}$$

where ∅ is the phase field parameter, and *G* is the chemical potential. In this formulation, surface tension force is computed as a distributed force over the interface using only *ψ* and the gradient of the phase field variable.

4.4.3 Initial conditions

All velocity components have been set to zero and pressure has set to be at atmospheric condition everywhere in the domain. Also, the initial interface between water and air has been specified.

4.4.4 Boundary condition at top and bottom surfaces

As shown in Fig. 4-4, the top and bottom surfaces have been treated with wetted wall conditions. Conventional no-slip conditions do not allow any motion of the interface. This restriction is overcome with the wetted wall condition where the interface is allowed to have some slip by adding a slip length and a friction force. Additionally, to calculate the surface tension force from Eq. 4.17, a contact angle is defined on the surface as shown in Fig. 4-5(b). The contact angle on the bottom and top surface have been specified as that of the contact angle of water on Teflon coated surface which is 114°. On the activated electrodes, modified contact angle was directly calculated from Young-Lippman equation corresponding to the applied voltage (Fig. 4-5(b)).

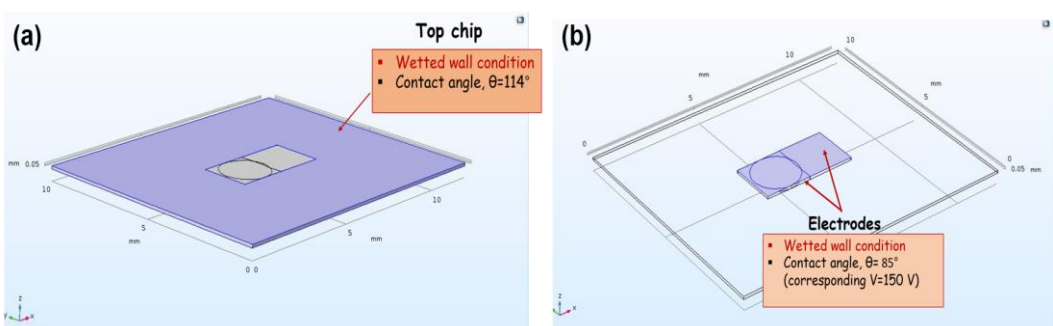

Figure 4-4 Boundary conditions on top and bottom surfaces.

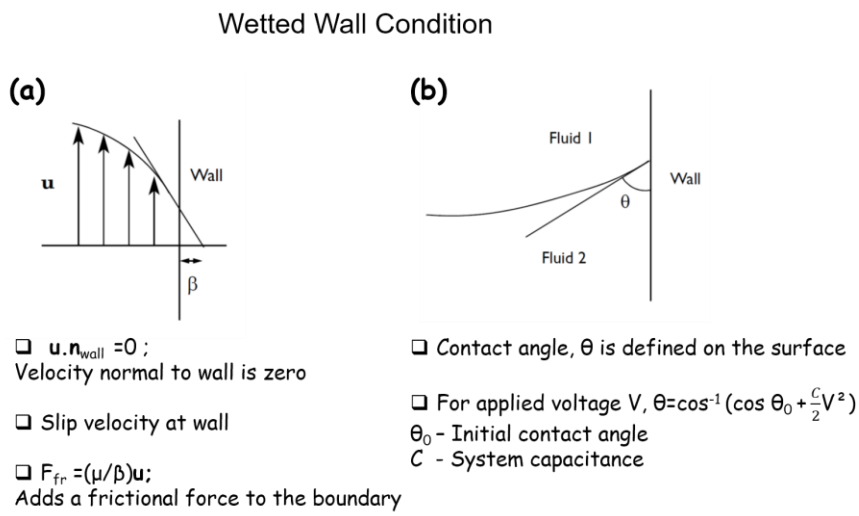

Figure 4-5 Definition of Wetted Wall condition.

4.4.5 Boundary condition on side boundaries

No-slip condition has been applied on four sides of the domain which makes all three velocity components to be zero at the wall (Fig. 4-6).

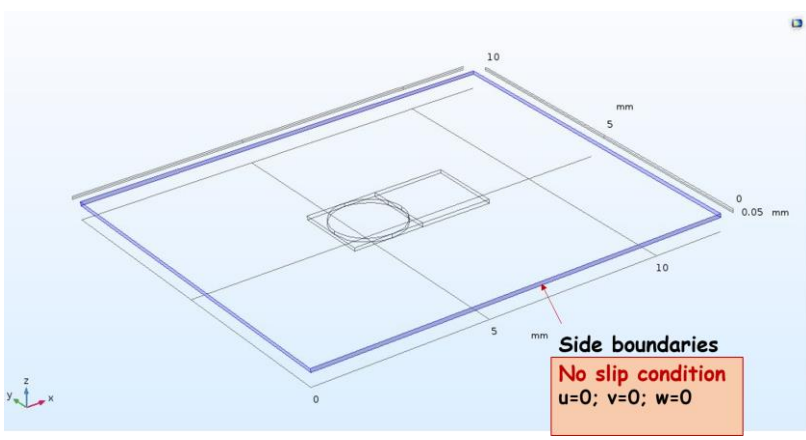

Figure 4-6 No-slip condition on side boundaries.

4.4.6 Meshing

Free tetrahedral mesh elements have been used in the computational domain. This mesh elements are unstructured. In the water domain and in the nearby region, fine

elements have been chosen and everywhere else normal elements have been used. After the meshing, total of 23, 45,593 elements have been created.

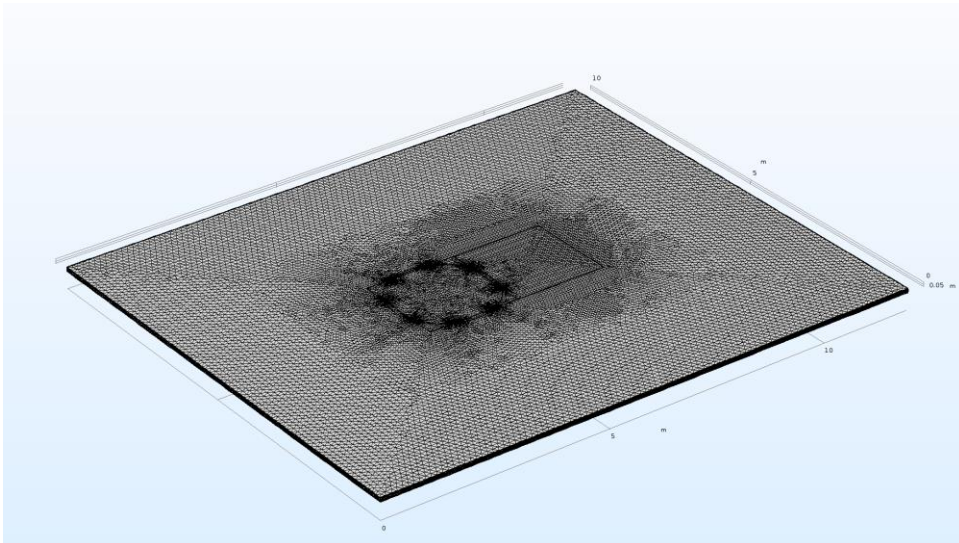

Figure 4-7 Meshed domain.

4.4.7 Solving the equations

After meshing the geometry, first to initialize interface position, an initialization step has been solved. Next, time dependent direct solver has been used to solve for the time dependent velocity, pressure and the interface tracking function. Values of some numerical parameters have been chosen by trial and error to expedite convergence. Table 4-2 shows the parameter values that were used in the simulation.

Table 4-2 Simulation Properties

Parameter name	**Parameter value**
Surface tension, σ	.072 [N/m]
Applied voltage, V_{ac}	150[V]
Initial contact angle,θ_o	118[degree]
Dielectric thickness, d	5[µm]
Dielectric constant, ε_r	2.5

4.5 Results and Discussions

First the fluid flow simulation was carried out both using phase field and level met methods. The results are slightly different in terms of mass conservation and droplet profiles. Conservative level set method was found to be highly efficient in conserving mass compared to the mass conservation in the phase field method. But the droplet profile was smoother in case of phase field method (Fig. 4-9). As shown in Fig. 4-8, along with the unusual droplet profiles there was some instability in case of level set method. These observations were consistent with that reported in [53]. The computational time for level set method was significantly larger than in the case of phase field method.

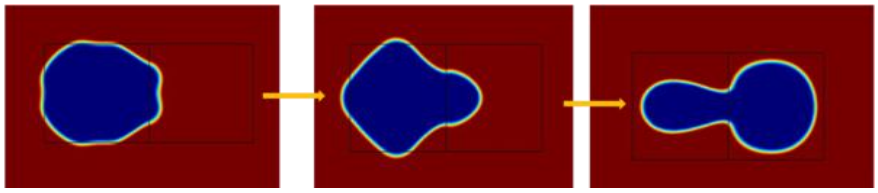

Figure 4-8 Droplet profiles in level set method at different time instants solved by level set method.

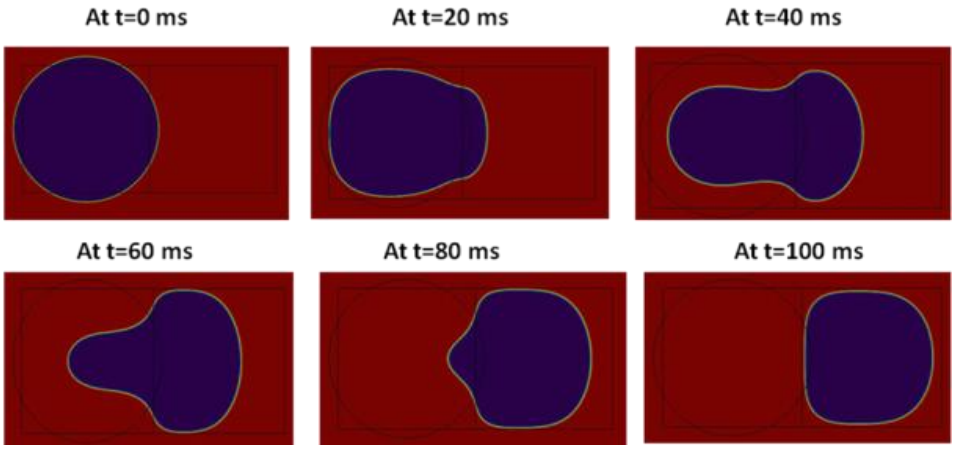

Figure 4-9 Droplet position at different time instants during motion solved by phase field method.

For phase field method, significant mass loss was observed. A parametric study was conducted for the numerical parameters including mobility tuning parameter (χ), interface thickness and initial time step to find out their influence on mass conservation. Among these parameters, mobility tuning parameter was found to have the most dominant effect as shown on mass conservation. As shown in Fig. 4-10. More mass loss is observed for lower values of the parameter. Compared to the lowest studied value of .001 of χ, the mass loss for the value of 1 was 21 % less. But this parameter also affected droplet velocity. To match our simulation results with that of the experiments performed in our group, a suitable value was finally used in the simulation with the expense of considerable amount of mass loss.

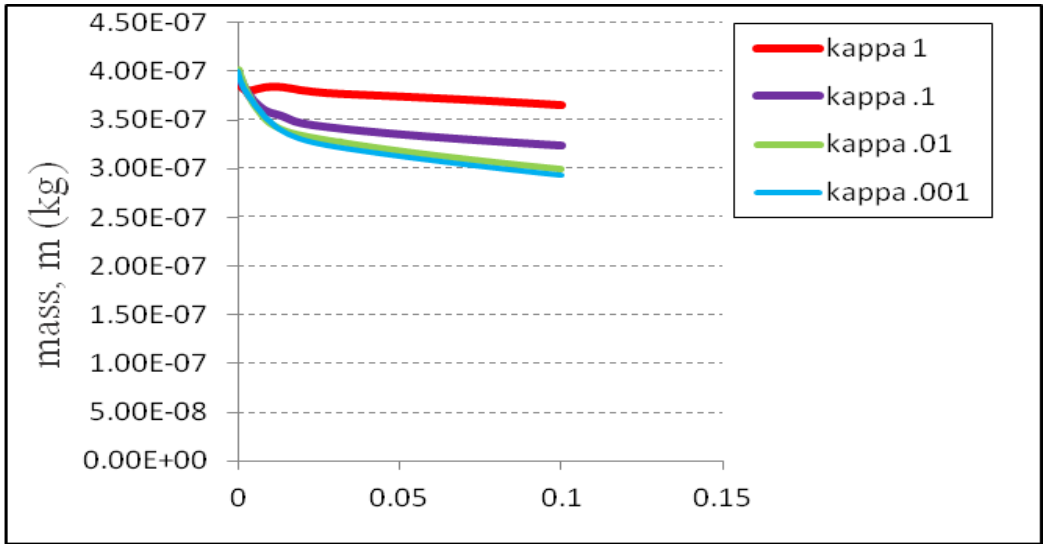

Figure 4-10 . Effect of mobility tuning parameter on droplet mass loss for Phase Field method.

For the same physical and geometrical parameters as of the experiments already mentioned in table 4-1 & 4-2, the droplet takes almost 90 ms to complete the transition from one electrode to another as shown in Fig. 4-9 which is slightly less than the experimental case which is about 100 ms. Unlike the level set method, phase field method is better in terms of maintaining smooth droplet profile. The comparison between the experimental and simulation results are shown in Fig. 4-11. The slight difference between the two profiles at the same time instant can be attributed to several factors. First of all, contact angle hysteresis and contact line friction was not included in our modeling which can have significant contribution on droplet deformation leading to different droplet shapes. Also mass loss may be another factor contributing to this difference. However, as already discussed, in spite of those limitations, our numerical modeling shows quite good agreement with the experiment.

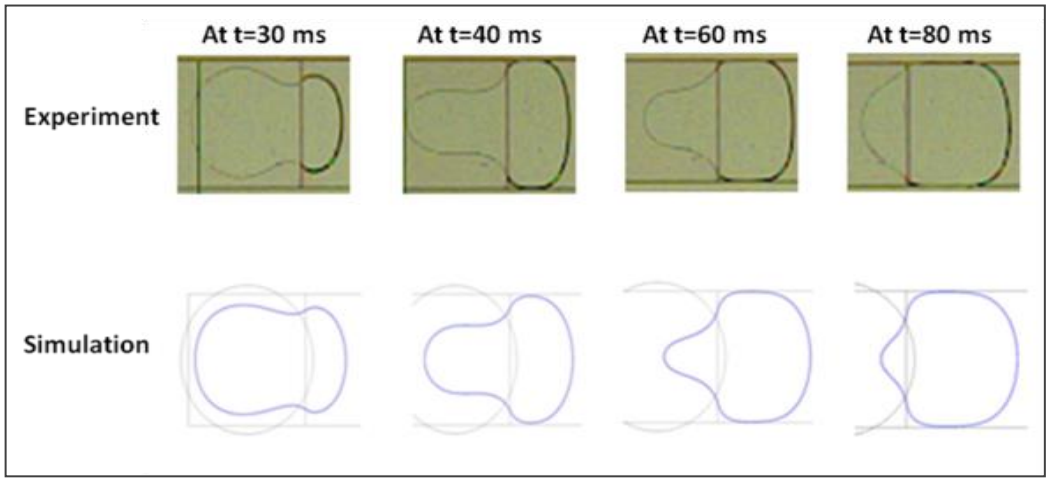

Figure 4-11 Comparison of droplet profiles from experimental and simulation at different time instants.

4.6 Conclusion

In this study, three-dimensional droplet motion in response to electrowetting force has been simulated using COMSOL Mutltiphysics. Our numerical results have been validated with experiments and they show good agreement with each other. We also compared two different interface tracking algorithms: phase field and level set method in terms of mass conservation efficiency. Additionally, we investigated the effects of mobility tuning parameter on mass conservation for phase field method. This model can be coupled to different physics interfaces including diffusion or evaporation to study different applications of electrowetting on dielectric (EWOD) applications.

Chapter 5

Characterization of Phase Separation of Multiphase Droplets on EWOD DMF

5.1 Introduction

Multiphase droplets involve two or more immiscible phases sharing a common interface with each other, typically surrounded by a third medium, which is immiscible to themselves as well as shown in Fig. 5-1. If the droplet medium is liquid, these droplets are called multiple emulsions. They are called aerosol droplets if they are suspended in a continuous vapor phase. In nature, multiphase droplets exist in multiphase processing, biological interactions within cells and atmospheric chemistry. The concept of multiphase droplet systems has been of interest, initially as a curiosity for almost a hundred years, but recent developments in droplet handling have re-kindled research into these multiphase droplet systems [54].

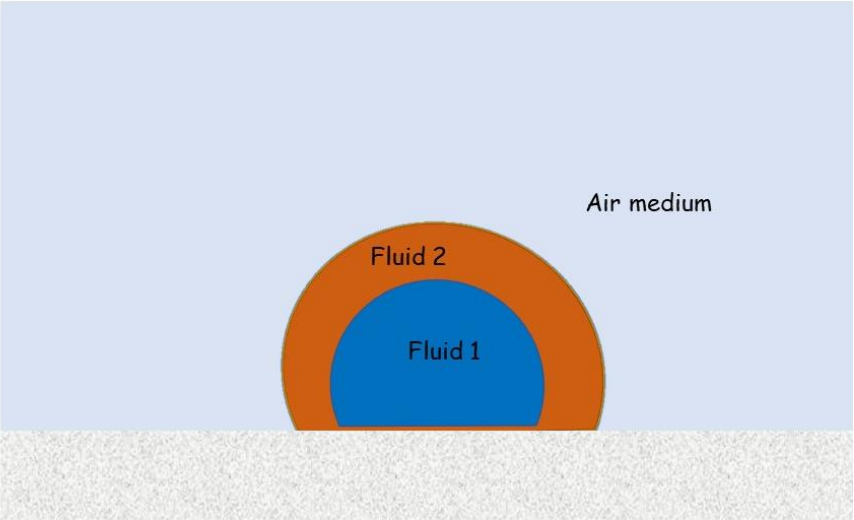

Figure 5-1 A compound sessile droplet on a solid substrate.

Different equilibrium geometric configurations of these droplets can arise which are governed by the minimization of the interfacial energy of the system. Often times, one phase is completely engulfed by the other phase which are called completely engulfing or core shell droplets as shown in Fig. 5-2. The non-spherical or partially engulfed droplets are sometimes called the “janus particles”.

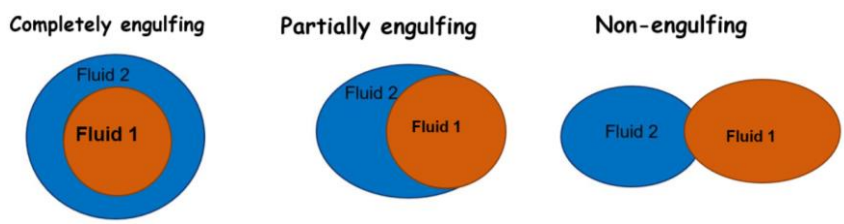

Figure 5-2 Different configurations of multiphase droplets.

The topology of a multi-phase droplet depends on the interfacial tensions involved. According to Gibbs free energy model, a core-shell droplet will be formed spontaneously if the change in Gibbs free energy, ΔG is reduced [54] as shown in Fig. 5-3. Here, Δ*G* is the difference between the interfacial energy of the formed multiphase droplet and the combined interfacial energies of the individual single droplets of the component phases as expressed in Eq. 5.1. The interfacial energies are the products of surface tension and surface area (Eq. 5.2). In these formulations, subscripts A and B denote components A and B of the multiphase droplets, γ is the surface tension co-efficient and *S* is the interfacial area.

$$\Delta G = G_{AB} - (G_A + G_B) \tag{5.1}$$

$$\Delta G = \gamma_{AB} S_{AB} - (\gamma_A S_A + \gamma_B S_B) \tag{5.2}$$

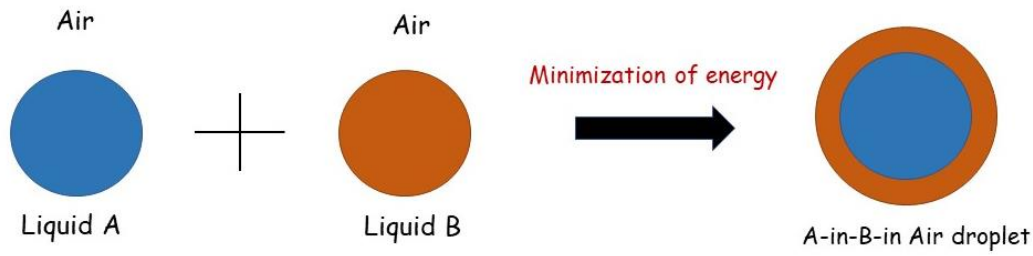

Figure 5-3 Formation of multiphase droplet in air.

A stability diagram has been formulated [45] which can be used as an indicator to predict a particular configuration. For a sessile multiphase droplet where the third immiscible phase is air, the determining factor for configuration is their interfacial tensions. If density difference exists between the phases, micro-gravity conditions can be a determining factor in obtaining the equilibrium structure. However, if all the phases are liquid, there exist additional degrees of freedom which allow the fluids to have rotational turning. In those cases, the stability of these droplet systems depend on the volume ratio of the phases present.

For a sessile multiphase droplet, depending on the values of the interfacial tensions, the following three scenarios can happen:

- *Complete engulfing:* droplet of phase A is entirely encapsulated by the droplet of phase B ($\gamma_A > \gamma_B + \gamma_{AB}$) or vice versa ($\gamma_B > \gamma_A + \gamma_{AB}$); For example, a water-in-oil droplet can form naturally due to the described condition but by adding surfactant into water, the configuration can be reversed.
- *Non-engulfing*: droplets of phases A and B are separated by the external phase ($\gamma_{AB} > \gamma_A + \gamma_B$);

- *Partial engulfing*: droplets of phases A and B have a common interface and are both exposed to the external phase (none of the above inequalities hold).

For the case where the multiphase droplet is sandwiched between two parallel plates, the shape of the surface is affected by the contact angle of the liquids on the substrate and the spacing between them. It has been reported that, for a water-in-oil droplet in the parallel-plate structure, there are two possibilities of the configuration where the change in Gibbs free energy is negative. In the first configuration, water directly wets the solid (Teflon) surface and in the second configuration, oil forms a thin film underneath the inner water droplet as shown in Fig. 5-4 which is more favorable.

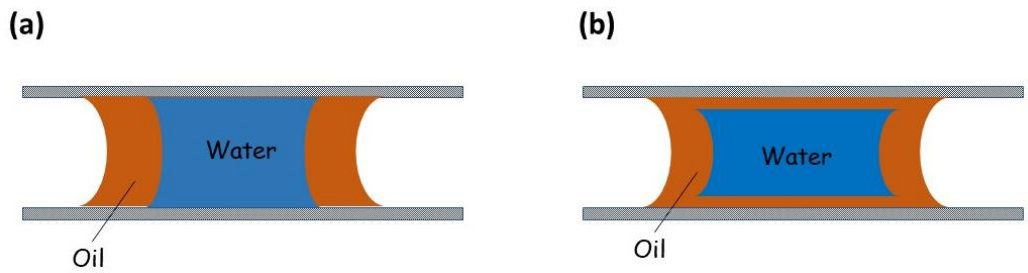

Figure 5-4 Multiphase droplet in parallel plate device. (a) Water rests directly on Teflon surface. (b) There is a thin layer of oil beneath water on the Teflon surface.

Many studies have been conducted to understand the equilibrium configurations of multiphase droplets [54-59]. Thermodynamically, droplets prefer the configuration which allows them to be in minimum energy state as discussed earlier. But kinetics during the formation process can also play an important role. Especially when the driving force is small, kinetic factors such as viscosity may play the dominant role instead of the thermodynamic effect, making a thermodynamically non-engulfing droplet becoming partial-engulfing [60]. The structure of microdroplets plays significant roles in their

applications. For example, the core-shell structure can encapsulate and protect active ingredients and deliver them to the position with lesions [61]. Partial engulfing droplets are desirable for producing particles with two distinct sides such as the Janus particles which could be used as emulsion stabilizer and building block of electronic paper [62]. The inner phase with active ingredients could also be released from the outer phase by the dewetting process, forming a non-engulfing structure [60].

5.1.1 Advantages and Applications of Multiphase Droplets

Different morphologies of multiphase droplets can offer unique capabilities which can be utilized in different applications. For example, the engulfing states can provide encapsulation for active compounds for controlled release through a polymerized shell which can be used in drug delivery [63]. Most of the times, the shells are made up of biodegradable polymers or hydrogels which degrade inside the body through which they can release the drug. Stimuli responsive microgels can be designed using physicochemical motifs, which are able to respond to pH, temperature, electric field, or glucose changes, and provide an intelligent release of drugs [64]. Recently, micron-sized oil-in-water droplets were considered as hydrophobic drug carriers for efficient drug encapsulation, long-term storage, and sustained drug release [65]. Water/Oil/Water (W/O/W) emulsions stabilized with phospholipid surfactants can be formed using the typical capillary methods for creating multiple emulsions in microfluidics [66]. If a volatile organic compound is chosen as the oil phase for the emulsion, the phospholipids adsorbed to the two surfaces are brought into contact as the oil phase is evaporated, and thus, a vesicle is formed (Fig. 5-5 (a)-(c)). Vesicles are a promising application of multiphase droplets which may enable applications including drug delivery. In all the above studies, microfluidic flow-focusing devices were used to generate multiphase

droplets where the droplet size was tailored by varying the flow conditions. Furthermore, the emulsification process can be controlled so as to formulate customized templates for micro-particles which have potential applications in pharmaceuticals as well as cosmetics and food industry as shown in Fig. 5-6.

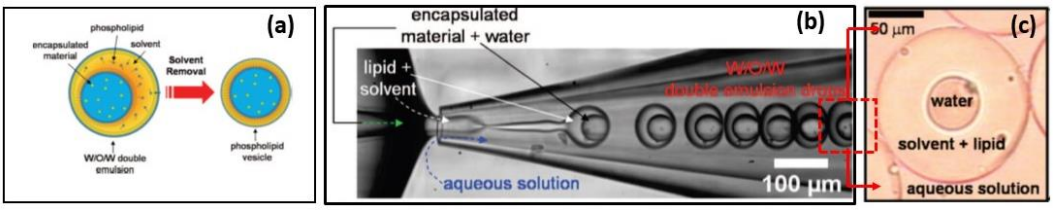

Figure 5-5 Formation phospholipid vesicles from templating multiphase droplets. (a) Preparation of phospholipid vesicles using double emulsion as templates. (b) Formation of phospholipid-stabilized W/O/W double emulsion in a glass microcapillary device. (c) Optical micrograph of the double emulsion collected. The double emulsion drops have an aqueous core surrounded by a solvent shell containing phospholipid [65].

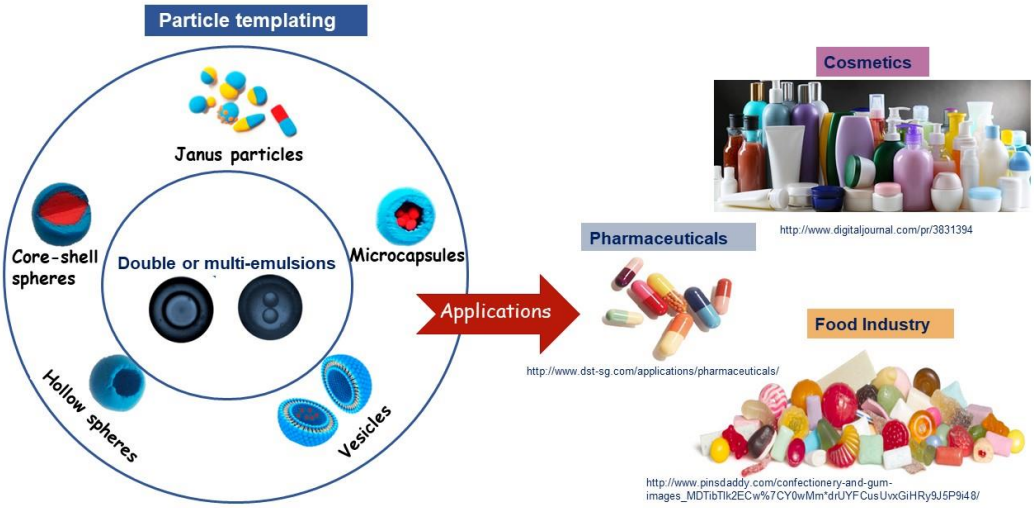

Figure 5-6 Applications of multiphase particle templates.

Multiphase droplets can be used in various biological applications. Encapsulation of living cells may enhance their viability [67]. It is also possible to encapsulate microorganisms, enzymes or blood proteins where the shells can act as protective and isolating vessels [56]. Multi-phase droplets can be used as microreactors [68]. Zahra et al. [68] demonstrated the capability of biphasic droplets for on-drop chemical separation and sensing. They chose ionic liquids as functional fluids whose chemical and physical properties can be tailored to be task-specific, and outlined how aqueous–ionic liquid multiphase droplets can be generated with tunable structures through appropriate fluid selection and device operation. They also demonstrated and proposed potential analytical applications—separation of a binary aqueous mixture of organic dyes and dynamic pH sensing (Fig. 5-7).

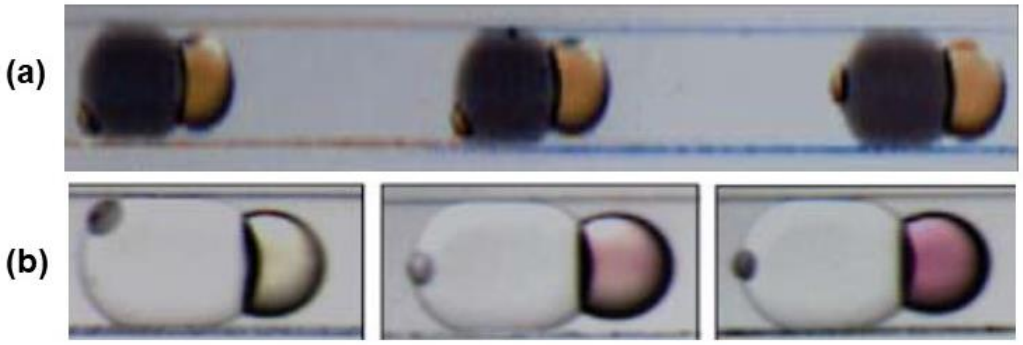

Figure 5-7 Stereomicroscopic images of selective liquid–liquid extraction of orange II out of an aqueous binary mixture with Methyl Blue into the ionic liquid compartment along the microchannel (b) Stereomicroscopic images illustrating on-drop pH-sensing showing the ionic liquid compartment gradually changing color (from yellow to deep pink) as it translates along the length of the microchannel [68].

5.1.2 Multi-phase Droplets in Droplet Microfluidics

Most of the applications of multiphase droplets discussed in the last section are performed in microchannels. In droplet microfluidic platform, multiphase droplets are surrounded by another liquid medium which carries them to the target locations. This carrier liquid is driven by the pressure difference created in the channel upstream and downstream by pumps. The conventional multiphase droplet generation techniques include complex coacervation, internal phase separation, layer-by-layer electrostatic deposition, interfacial polymerization, spray drying and emulsification [70]. Researches have studied device geometry, flow conditions and kinetics to manipulate droplet dimension, size distribution and configurations of the phases [69 -75]. The most common devices for microfluidic production of complex droplets are coaxial assemblies of glass capillaries and planar microfluidic devices. Planar (two-dimensional (2D)) microfluidic devices are usually fabricated by soft lithography mainly from poly(dimethylsiloxane) (PDMS) elastomer. Because of the rectangular shape of the channels, the continuous phase cannot completely surround the dispersed phase during the drop generation process. For the fabrication of glass capillary devices, it is required to taper a number of round glass capillaries and align them within a square capillary or a larger round capillary. Glass capillary devices have superior optical and chemical properties and offer straightforward surface functionalization, but are difficult to be parallelized for higher production rate of droplets [72, 73].

The droplet formation in continuous microfluidic devices occur mainly in three flow regimes: dripping, jetting and squeezing [72] (Fig. 5-9). The drop formation mechanism in each regime is different and governed by interaction of several forces, such as interfacial, viscous, inertial and gravitational. Typically, the effects of gravity on

drop formation can be neglected if the characteristic length, i.e., the drop diameter, is in the micrometer range (less than 1 mm).

In the dripping regime, inertial force is negligible and interfacial force is dominant. Interfacial force tends to pull back the forming drops towards the injection nozzle orifice. The drop formation begins when the viscous force exceeds the pinning force arising from the interfacial force and drops are formed very close to the orifice of the injection capillary. The jetting regime is characterized by formation of a long jet that eventually breaks into drops further downstream from the orifice. In squeezing mode, the shear force exerted by the continuous phase is much smaller than the interfacial force; hence, the forming dispersed phase drop keeps growing until it almost fills the entire main channel.

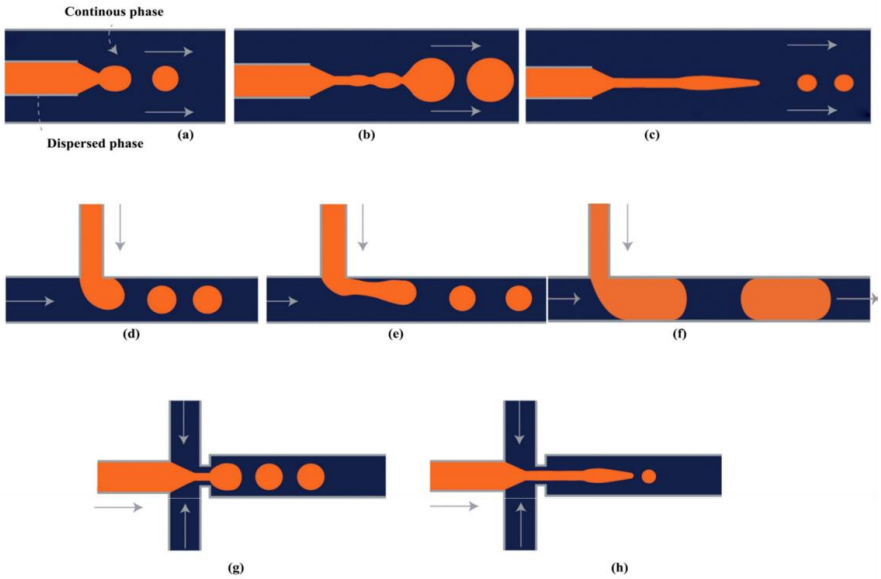

Figure 5-8 A droplet breakup in each of the three main microfluidic geometries used for droplet formation; (a–c) show dripping, widening jetting and narrowing jetting respectively in co-flow drop makers; (d–f) show dripping, jetting and squeezing in T-junction; (g,h) show dripping and jetting in flow-focusing drop maker. The orange and dark blue colors represent the dispersed phase and continuous phase respectively [72].

Multiphase droplets can be formed in either one or two consecutive emulsification steps. Nie et al [77] used a single step emulsification approach to form double emulsion by using a double flow-focusing unit as shown in Fig. 5-9. The central innermost channel was used to supply the core fluid and the other two outer central channels were used to supply the shell liquids. The aqueous continuous fluid was introduced from two side channels. A multiphase jet was formed from the inner and the middle fluid. This jet was then focused in the orifice and due to the jet instability multiphase droplets were formed in the downstream chamber.

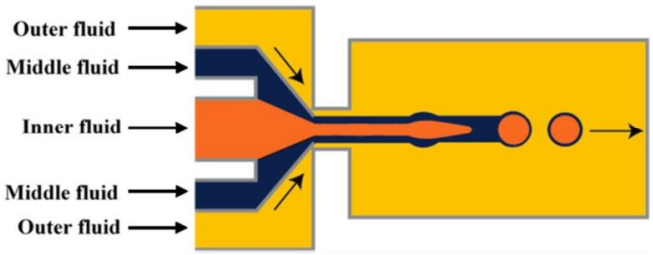

Figure 5-9 Schematic of production of multiphase droplets in microfluidic flow focusing planar device with co-flow flow focusing geometry [77].

A two-step emulsification approach was used by Okushima et al. [78]. They used a pyrex glass chip with two serial T-junctions. The wettability of the two junctions were different. In the first hydrophobic junction, water-in-oil single phase droplets were produced. The droplets then enter the second hydrophilic junction where water was supplied though the outer channels to form water-in-oil-in-water double emulsion droplets (Fig. 5-10).

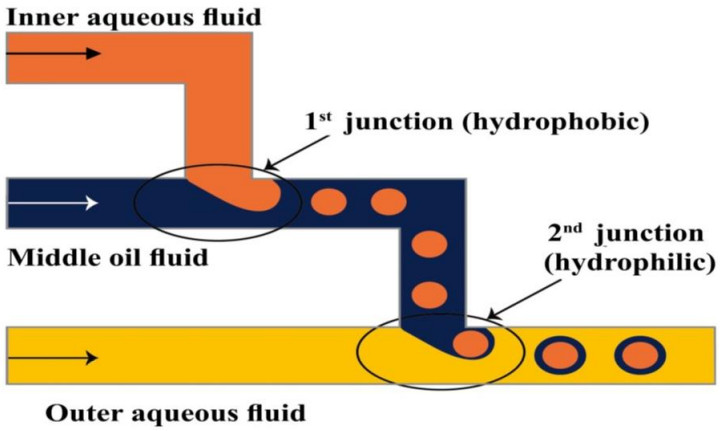

Figure 5-10 Production of W/O/W emulsions using two serial T-junctions with different wettability [78].

Multiphase droplets have been studied in droplet microfluidics with the most focus given on droplet generation strategies and various applications. Once formed, the droplets are transported by pressure driven flows in the channel and taken to the targeted locations for further manipulation like sensing. In some of the applications mentioned in our previous discussion, an additional operation is needed which is the breaking up or separation of the droplet phases. Very few studies can be mentioned in that respect [79-84]. In those studies, different approaches have been taken to either avoid or induce separation. For example, Jiang Li et al., studied the break up of multiphase droplets in a tapered nozzle [80]. In this study, multiphase droplets were moved through a constriction to mimic the motion of cells or other agents carrying drugs through constricted arteries or veins in biological systems or the extraction of oil/gas from underground through porous media in extraction processes. Their motivation was to find the controlling parameters for the droplet breakup which is an important phenomenon in the mentioned situations. They found that, due to very small Capillary number, ($Ca \ll 1$), surface tension stress was dominant over viscous stress, causing Rayleigh Plateau capillary instability which is the likely reason for the breakup of the shell. They investigated the role of shell thickness,

diameter ratio of the core to the orifice and the tapered angle in the droplet breakup dynamics. Haosheng Chen et al. [84] also conducted experiments to investigate droplet breakup in a constricted glass capillary channels (Fig. 5-11(a)). They made separate capillary tubes to first generate the droplets and later to break them up. The tubes were connected to each other. After flowing through the breakup device, the droplet showed four different breakup behaviors for different flow conditions and geometry. Therefore, they proposed a diagram to predict the breakup outcomes based on the capillary number of the flow and the droplet-to -nozzle diameter ratio (Fig. 5-11(b)-(c)). The diagram shows that, there can be four regions where the complete release of the core happens in two of them. In one case, the shell breaks up and residue from the shell is left with the core. In the first regime, the droplet does not breakup

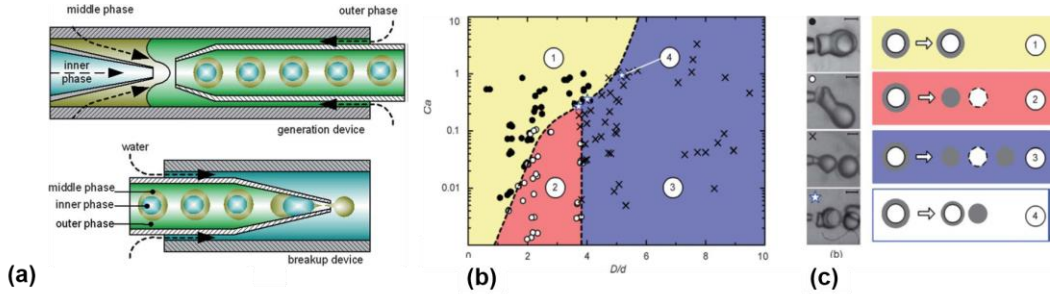

Figure 5-11 (a) Schematic of the microfluidic device used for forming (top) and breaking up multiphase droplets. Here inner phase is water (W), middle phase is oil (O) and the outer phase is water (W). (b) A phase diagram of diameter ratio D/d and different capillary numbers Ca. (c)The sketches on the right illustrate the behavior in the four regimes respectively. The filled gray circles represent the middle oil phase (O), the white circles represent the inner droplet, the black continuous lines represent the interface between the inner aqueous phase (W1) and the middle oil phase (O), and the dashed lines represent the imaginary surface of the inner droplets after release [84].

Khan et al. [85] studied the dynamical behavior of gas-water multiphase droplets in a microchannel flowing through an oil medium. They observed interesting behaviors of the droplets when they entered a junction of multiple channels or a branching point. They observed the droplets to separate or split in transit through junctions. The drops separated when the constituent bubbles and drops were of smaller length than the diameter d of the bifurcation, as shown in Fig. 5-12(d)–(f), where a small loop is introduced in the flow path. Another interesting observation is that detached bubbles and drops do not always take the same arm of the loop, but instead consistently alternate between the two arms. In Fig. 5-12(g) symmetric splitting of bubble–drops are observed at a bifurcation, when the constituent bubble and drop are each larger than the junction diameter, d. They noted the similarity between features of multiphase droplet behavior at junctions to size-dependent single-phase drop splitting at junctions.

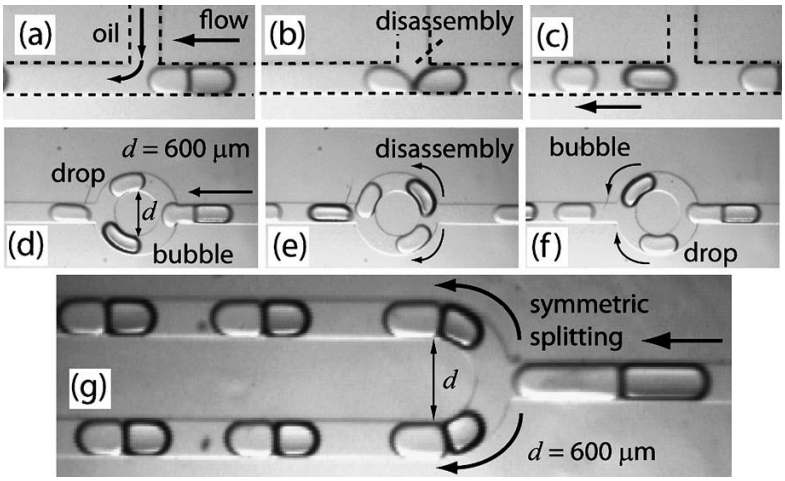

Figure 5-12 (a)–(c) Multiphase droplets can be disassembled into individual bubbles and droplets by transverse injection of oil into the flow channel. (d)–(f) Flow and disassembly at a loop in the flow path. (g) Splitting of multiphase droplets into equally sized daughter droplets at a bifurcation [85].

In droplet microfluidics, breakup of phases happens mostly due to shear stress. One way to achieve that is by creating a constricted exit or branched flow path. These are passive techniques of phase separation and can be controlled by changing device geometry or flow conditions. One study proposed to change the interfacial tensions of the phases by using thermo-capillary effects to achieve phase separation thermodynamically [83]. Other methods of phase separation in droplet microfluidics include controlling the wettability of phases [86], osmosis [87] and surface tension [88].

5.1.3 Multiphase Droplets in Digital Microfluidics Platform

Compared to continuous microfluidic devices, until now very few researches in digital microfluidics have focused on the generation methods of multiphase droplets. So far only one method of forming these droplets is reported which is very simple and does not require innovation in device geometry. In this method, two droplets which will later form the outer and inner phase in the multiphase droplet are generated individually in distinct reservoirs. They are then brought together in order to cause coalescence. Depending on the interfacial tensions, they can form completely engulfing or partially engulfing droplets.

As discussed in the last section, researchers have explored numerous capabilities of multiphase droplet systems in continuous microfluidic platform ranging from drug delivery to bio-chemical synthesis and reactions. Recently some of these applications have been realized into digital microfluidic platform. Compared to continuous microfluidics, one of the most interesting advantages of digital platform is the very high flexibility and dynamic reconfigurability that are achieved by using software-driven electronics to control the droplet driving forces. This also eliminates the need for both

permanently etched microchannels and complex mechanical components (pumps, valves, tubing, etc. [58]. Daniel Brassard et al. [14] proposed of using multiphase droplets for improving the operation of EWOD devices. By using a silicone oil shell around an aqueous droplet operated by EWOD forces, the contact angle hysteresis was shown to be decreased which increased the droplet velocity at a given applied voltage. Typically, if silicone oil is used as the surrounding medium, it poses several difficulties including increased viscous drag and difficulty in device packaging. The interfacial tension was also lowered by using oil shell which further decreased the required voltage to achieve a certain velocity. Thus, theoretically it is possible to reduce damage of the dielectric layer by cutting the need for high voltage operation and increase the overall life of the device. Another advantage that the oil shell can provide is that it can act as a shield to protect the inner core from evaporation and biofouling. In a separate study, reactions inside core-shell droplets were performed [89]. A viscous oil core was carried inside an aqueous droplet as a demonstration (Fig. 5-13). Organic cores of bromine in benzene (yellow colored) and styrene in benzene (gray in color) were carried in two different droplets having aqueous shells of 8% PVA solutions. The two droplets were brought together and manipulated by EWOD to have a collision. After they merged together, by successive stretching and relaxing of the fused droplet, the cores were mixed and the coalesced cores took part in bromination reaction. The change in the core color to become clear indicates the completion of reaction (Fig. 5-13(a)). They also demonstrated that gaseous chemicals in the cores of multiphase droplets with aqueous shells can also be manipulated by EWOD and react with other chemicals. Reaction between red blood cells (RBCs) and carbon monoxide (CO) bubbles were performed where the gas cores were carried inside 8% PVA aqueous solution. After the reaction was completed, CO poisoning of the RBCs was evaluated by using the sodium hydroxide (NaOH) test.

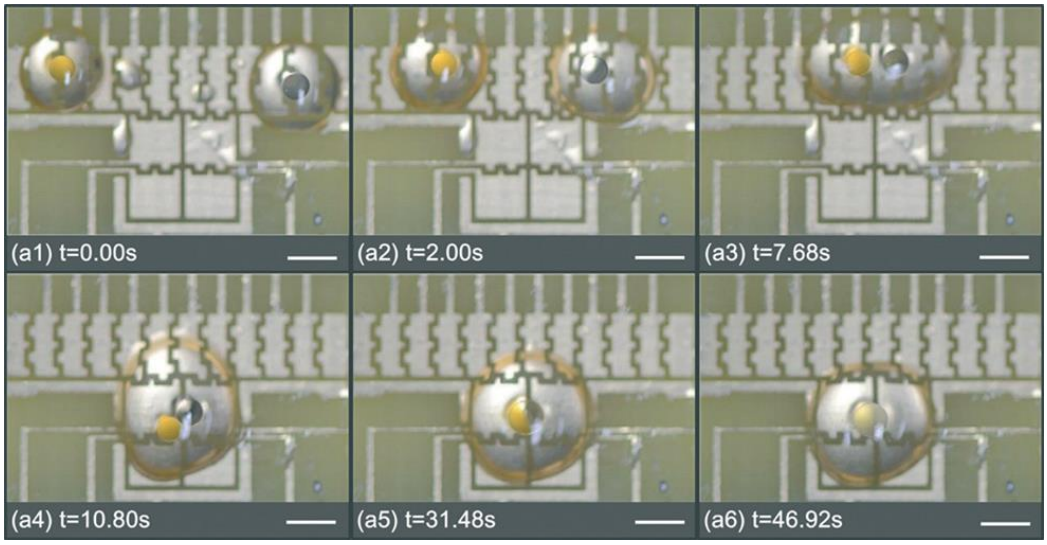

Figure 5-13 Manipulation of two compound drops with organic cores. (a1)– a3) The two drops were driven to collide and merged into one drop with two inner cores. The yellow core in the left drop is the solution of 0.2 M bromine in benzene, while the grey core in the right drop is the solution of 0.85 M styrene in benzene. (a4)–(a6). The stretch of the compound drop under the voltage pulses applied to the electrodes, and the two inner cores that have finally coalesced. Scale bars in the images are 2 mm [89].

Another study was conducted by Pavithra Wijethunga et al. [10], to perform liquid-liquid microextraction on EWOD DMF platform where an ionic liquid droplet and an aqueous solution droplet formed a multiphase droplet. One of the phases contained the extractant and after forming the multiphase droplet by bringing the individual droplets together, the extractant was extracted into the receiving phase. The extraction performance and kinetics were evaluated by an image-based concentration measurement technique. Compared to macroscale extraction process, this droplet based liquid-liquid microextraction approach can be integrated into lab-on-a-chip devices to provide fully automated, high-throughput extraction.

As discussed so far, most of the studies on multiphase droplets in digital microfluidics platform utilized the advantages and flexibilities of these droplets in various applications. The first study on multiphase droplet separation on digital platform was reported by Fan et al. [90], where a silicone oil-water core-shell droplet was separated by using dielectrophoretic and EWOD forces respectively. Although the volume of the water and oil phase were equal, residue from oil phase was left in the water phase. The next study by the same group utilized a new solution to achieve the complete separation. This time they submerged the water-oil compound droplet in hexane solution which dissolved the oil phase and the volatile dissolved solution was then evaporated leaving behind only the water droplet [91]. The main disadvantage of this technique is that it is not versatile. Silicone oil is not biocompatible and many applications may need a more suitable liquid to make a pair with water. Secondly, since the oil needs to be actuated by DEP, different voltages for EWOD and DEP are required which make system integration more difficult. Phase separation by splitting the droplet was reported by Pavithra et al [10]. This time, a water-ionic liquid multiphase droplet was separated using EWOD force. Similar to the method for splitting a single phase droplet, equal voltages were applied on two nearby electrodes touching two opposite edges of the droplet. The multiphase droplet was first elongated in the lateral direction and a neck was formed almost in the middle on the deactivated electrodes. Then gradually the neck became thinner and eventually broke up. After the separation, some residue was left in one of the phases. Although, the technique was same as droplet splitting, since the two phases have different fluid properties, the physics is different. For example, due to difference in the surface tension co-efficient, the actuation forces will be different for the same voltage. Again, due to different viscosities, the resulting viscous drag forces in two phases are different. Consequently, two ends of the multiphase droplet end up with having different advancing velocities. This leads the

necking to happen elsewhere other than the liquid-liquid interface and separation is completed with some residue in one of the phases.

5.1.4 Motivation and Objectives

Because of the versatility in the encapsulation and controlled release of active ingredients from the core, multiphase droplets have applications ranging from cosmetics, food processing, handling of hazardous materials, drug delivery etc. They can be used as carriers for cells in high throughput screening where droplets containing cells can be reinjected into another device for further manipulation such as sensing [90]. Multiphase droplets can also be used as vessels for chemical or biological synthesis. In drug delivery, controlled delivery of the ingredients can be ensured by the capability of the system to manipulate the droplet breakup [90]. In case of liquid-liquid microextraction processes [10], the final step is to separate the extracting phase from the donor phase to perform sensing or other operations on the chip. In synthetic biology or chemistry, the products from a reaction may need to be retrieved from the core of the core-shell droplet. Another example where the separation is important is the use of oil shells to enhance fluidic performance or reduce evaporation as discussed by Fan et al. [90]. In this case, removal of the oil shell may be required to obtain clear detection signals or rapid evaporation.

However, very few studies on deformation and break up mechanics of multiphase droplets have been conducted and most of them involved droplets in continuous micro channel environment or in a linear or extensional flow field in a viscous medium [79- 84]. In those studies, different approaches have been taken to either avoid or induce separation. But most of them utilized indirect ways to cause the breakup such as by using a constriction or a branching flow path.

Multiphase droplets have managed to receive a lot of attention from researchers from different fields and to use them in standalone lab-on-a-chip devices, all the basic fluidic handling techniques required in sample preparation steps and detection stages should be operable on them. Separation of phases is such a step which can be crucial for the performance and efficiency of certain processes in terms of cleanness in detection and reduction in sample waste. Although, some of the studies focused on understanding separation mechanism in channel-based microfluidics and they give some insights about the affecting parameters, none of them investigated the separation performance in terms of amount of residue formation. Also, the knowledge gained from those studies are not directly transferrable to digital microfluidics since the physics involved in the droplet actuation on digital platform is different than that of pressure driven flows in the microchannels. In order to transform digital microfluidics as a suitable candidate for many of the applications involving multiphase droplets, a robust phase separation technique needs to be established. The separation techniques mentioned earlier which require changing the thermodynamic equilibrium by changing interfacial tensions thermally, chemically or with other methods are not versatile and needs to be designed specifically to suit a particular application. Splitting the droplet mechanically using EWOD forces is the most simple and straightforward technique and generally applicable to most situations. But there has been very limited research to completely understand the physics of mechanical separation. Therefore, our first objective for this study is to have a comprehensive understanding of phase separation by applying mechanical force. Secondly, we aim to find the fundamental parameters and dimensionless numbers that govern the process. Finally, we will present some guidelines to design experiments to achieve better separation with minimal residue.

5.2 Theoretical Background

5.2.1 Droplet Splitting

Droplet splitting is a fundamental operation in digital microfluidic devices that is performed to generate daughter droplets from a parent droplet. The mechanism of droplet splitting has been shown in Fig. 5-14. The droplet is initially positioned in such a way that it covers two activated electrodes (Fig. 5-14(a)). As we can see, due to initial wetting, droplet takes the shape of two central electrodes and remains at equilibrium. Then two side electrodes next to the droplet are switched on while the central electrodes are switched off. As the droplet meniscus sees the active side electrodes, it is pulled toward them with a net force acting on the longitudinal direction. As a result, the droplet is stretched in the longitudinal direction. More and more liquid flows to the active electrodes and the amount of liquid at the middle keeps decreasing due to mass conservation. Simultaneously, on the central electrodes, hydrophobic contact angles are restored and

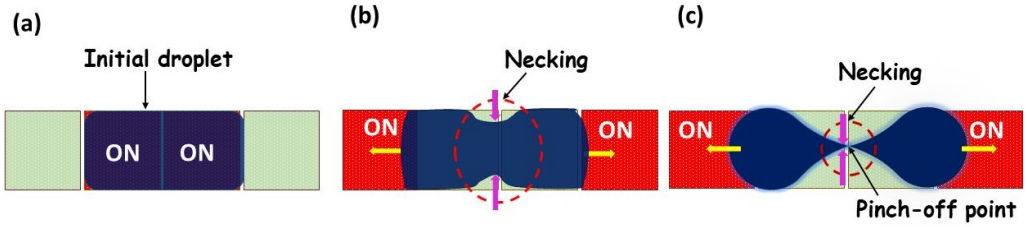

Figure 5-14 Droplet splitting process. (a) Droplet initially at rest at middle activated electrodes. (b) two nearby electrodes at each side is turned on and droplet is elongated; a neck is formed at the middle. (c) Necking continuous to become thinner and the droplet pinches off at the middle.

naturally dewetting of the meniscus starts to happen on the middle electrodes (Fig. 5-14(a)). This results in pulling the droplet meniscus inward. The net capillary force acts in

the transverse direction. The radii of curvature move toward each other making the middle part of the droplet narrower. This narrowing of the droplet is called the “necking”. The two oppositely directed radii of curvature keep moving toward each other until they meet and the very thin liquid bridge breaks at the pinch-off point (Fig. 5-14(a)). Thus, the single droplet becomes two droplets.

Many researches have been conducted to study droplet splitting on DMF platform [92-98]. A necessary condition for droplet splitting was formulated by Cho et al. [92] and it was concluded that for a given set of fluid properties and other system parameters, a smaller channel gap, a larger droplet size and a larger change in the contact angle enhance the necking of the droplet, hence helping the completion of the cutting process. Also, there should be a minimum voltage below which droplet splitting cannot happen. Bhattacharjee et al. [93] studied symmetric and asymmetric splitting. Symmetric splitting happens when the amount of liquid volume is same in two daughter droplets. When opposing pulling forces are created by applying equal voltages on electrodes with same dimensions, even then the left and right droplets have approximately 1% volume difference [95] which happens due to hydrodynamic instability [97]. Also, initially the droplet should have same amount of overlapping with the active electrodes on two sides to ensure symmetric initial condition. By changing the size of two electrodes or by applying different voltages at two sides, unequal sized droplets can be generated [93]. Assuming a proper initial condition, application of different voltages to the electrodes will generate liquid flows of unequal magnitude towards the energized electrodes. Liquid from the center of the droplet will flow towards the front causing the formation of a neck over the center electrode. Under the favorable condition resulting from the combination of the properties of liquid and solid materials and the geometrical parameters, due to resulting actuation forces from applied voltage, both sides of the

droplet continuously deform thus decreasing the width of the neck. Ultimately, the neck pinches off and two sister droplets of unequal volumes are created. If the actuation force from the electrode with lower voltage is not strong enough, the liquid flow rate to the corresponding direction gradually decreases and at one point, flow of liquid completely stops before the neck pinches-off. However, on the side of higher applied voltage, liquid continues to flow since the actuation force is stronger. The radius of curvature of the neck does not decrease anymore. As a result, liquid from the weak side flows back towards the neck in order to maintain the supply of liquid towards the stronger side. Eventually, the splitting of the droplet fails and the total liquid accumulates over the electrode with higher voltage [93].

5.2.2 Phase Separation

In this study, we are using the same principle that is being used for splitting a single phase droplet on EWOD DMF devices. Like splitting (Fig. 5-15(a)), when forces are applied from two sides, the droplet is stretched longitudinally and necking starts happening (Fig. 5-15(b)). But now the necking location and the interface position do not align with each other. Therefore, after pinch-off happens, there is some residue left in one of the phases. The difference between symmetric splitting and phase separation is that phase separation is an asymmetric process. As we discussed in the last section, in this case, actual scenario for phase separation is inherently asymmetric because of many reasons. The first factor contributing to the asymmetry is the difference in the amount of actuation force which can be expressed by the electrowetting number, $E=\frac{\varepsilon o\ \varepsilon}{2d\sigma}V^2$. For a given set of device parameters, electrowetting number can vary due to different voltages, (V) or different surface tensions (σ). Between two droplets having either one of them different, the droplet with higher electrowetting number will have higher actuation force

which will drive it at higher speed [100]. In case of multiphase droplets, if same voltages are applied on two sides while their surface tensions being different, the electrowetting numbers will still be different. On the other hand, if surface tensions are same but different voltages are applied, the electrowetting number will be different. But generally, the phase with higher electrowetting number will try to move at faster speed since more actuation force will work on its advancing meniscus. Because of the velocity mismatch, the alignment of the location of the pinch-off point and the interface gets affected.

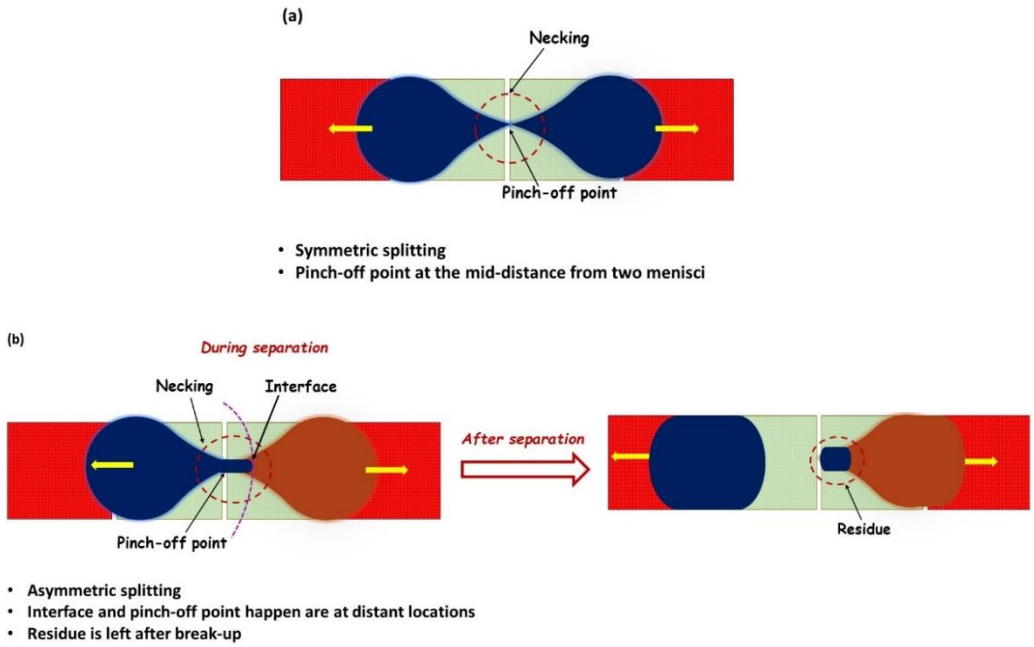

Figure 5-15 (a) Splitting of a single phase droplet. (b) Phase separation of a multiphase droplet.

The second asymmetric condition comes from different amount of deformation of the two phases. During splitting process, liquid flows towards energized electrodes in response to the electrowetting force. The droplet interface undergoes deformation and the deforming interface has to overcome a competition between surface tension and viscous forces. While viscous forces tend to favor the meniscus to deform, surface tension forces do the

opposite. Due to the surface tension force, droplet meniscus tries to maintain a spherical shape. Capillary number is an estimation of the relative strength of these two forces where Ca=$\frac{\mu \mathbf{U}}{\sigma}$ where σ is the surface tension co-efficient, μ is the viscosity and U is the velocity. Higher capillary number is related to a large amount of deformation and vice versa. There is a critical capillary number below which splitting does not happen although necking is present [93]. In case of multiphase droplet, the two phases have different Ca and they deform differently. Therefore, necking happens asymmetrically on an off-center position from the middle axis which is perpendicular to the interface at the neck. The third asymmetry comes from hydrodynamic instability because of which more liquid flows to one side [97]. It has been reported that, increasing the applied voltage in small increments can reduce hydrodynamic instability. This instability can also be reduced by reducing inequality of the applied force inside the fluid body which can be done by maximizing the wetting and minimizing dewetting which will be discussed further.

There is an additional challenge for phase separation. As mentioned earlier, multiphase droplets prefer to remain at equilibrium with the minimum energy configuration. Based on the ratio of their interfacial tensions, a stability diagram has been proposed which can be divided into four regions as shown in Fig. 5-16 (b) [56]. The two axes of the diagram represent the ratio of interfacial tension of each phase with the third or surrounding phase. These two ratios dictate thermodynamic preference for a specific configuration. For example, if both the ratios have values less than 1, droplet will prefer to be non-engulfing where phases exist as distinct droplets instead of pairing up to form one droplet with multiple phases. Which means, for completely engulfing or partially engulfing droplets, complete separation will only happen when both interfacial tension ratios become smaller than 1. So, this preference for maintaining equilibrium with a certain configuration acts as a constraint which should be overcome to achieve complete phase

separation. One way of doing that is by changing the surface tension ratios as proposed by Lavrenteva et al. [83]. In the theoretical study conducted by Lavrenteva et al. [83], partially engulfing non-isothermal droplets composed of two immiscible fluids were modelled to propagate in a temperature gradient field by thermocapillary migration. This concept can be described using Fig. 5-17. As the droplets moved along the direction of temperature gradient, the surface tension of the inner interface (interface between two droplet forming fluids) increased. The surface energy increased as well since, interfacial energy or Gibbs energy, G is the product of the surface tension, σ and the interfacial area, A and expressed by $(G = \sigma A)$. Now, since σ increases, surface area has to decrease to decrease surface energy according to energy minimization principle. As a result, in response to the increased interfacial tension of the inner interface, the same interface starts to shrink to minimize area, A and eventually vanishes, thus separating the two phases completely (Fig. 5-17).

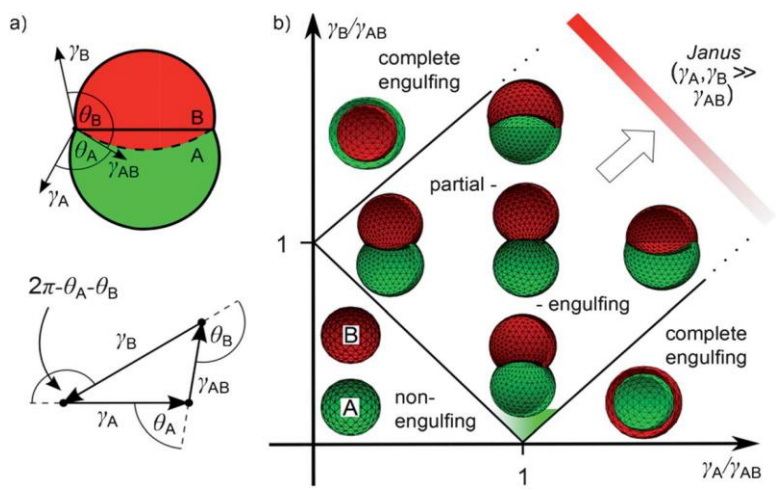

Figure 5-16 (a) Sketch of a double droplet with indicated contact angles θ_A and θ_B and the Neumann's triangle. (b) Stability diagram representing the possible morphologies of a double droplet of phases A and B in the case where V_A=V_B [56].

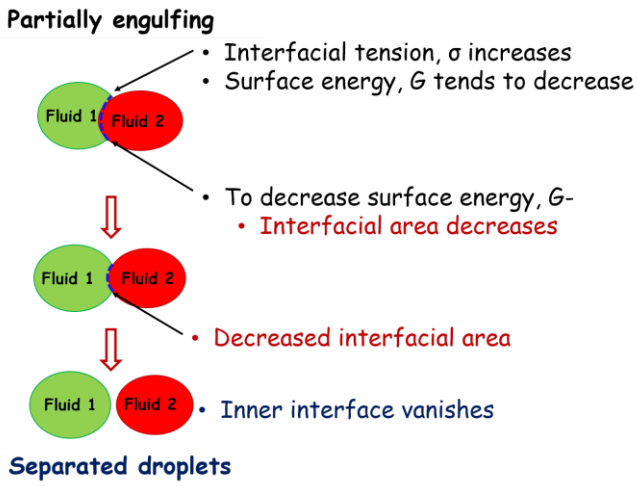

Figure 5-17 Demonstration of phase separation by increasing the interfacial tension. To minimize surface energy, surface area decreases and eventually vanishes altogether which separates two phases.

In our study, by applying mechanical force, we try to move two phases in the opposite directions. Fluids from the middle part of the droplet goes to two ends and necking happens. Interface between two phases resides in the middle region and since this region gradually gets depleted of liquid and the interfacial area shrinks. Until the pinch-off point, the interface keeps shrinking but it does not vanish completely because of the thermodynamic constraint that is present in the system due to the constant interfacial tensions of the fluids. Our objective is to find out the correct set of parameters so as to maximize the shrinking of the interface by aligning it with the pinch-off point which is the ultimate condition of minimizing the residue.

5.3 Experimental Details

5.3.1 Device Fabrication

A conventional parallel plate EWOD DMF device was used for the experiments. The device design, fabrication process and the experimental setup have been already discussed in chapter 2.

5.3.2 Operating Conditions and Working Fluids

Multiphase droplets were formed from the aqueous solution of glycerol and a room temperature ionic liquid (1-butyl-3-methylimidazolium hexafluorophosphate ([bmim][PF6])). We will refer them as 'AQ' and 'IL' from now on. Details about these two liquids are presented next.

Ionic liquid (IL): Ionic Liquids are ionic, salt-like materials that are liquid at below 100 °C. These liquids have lower melting points, sometimes below 0 °C. They can remain in liquid state over a wide temperature range (300–400 °C) from the melting point to the decomposition temperature of the Ionic Liquid. The strong ionic (coulomb-) interaction within these substances results in a negligible vapor pressure (unless decomposition occurs), a non-flammable substance, and in a high thermally, mechanically as well as electrochemically stable product. In addition to this very interesting combination of properties, they offer other favorable properties: for example, very appealing solvent properties and immiscibility with water or organic solvents that result in biphasic systems [101]. Some of the advantages of Ionic liquids are listed below:

- They can be synthesized by combining thousands of organic cations and anions with different functional groups. Because of this reason, the physical and chemical properties of ILs can be tailored by selecting the proper ions and changing the functional groups according to specific application.

- Very low vapor pressure. Because of this, they are able to retain constant concentration
- Non-flammable
- Bio-compatible, non-toxic and environment friendly
- Thermally stable
- Immiscible with water; suitable for bi-phasic systems
- High electro-elasticity
- Interesting solvent properties

Because of their unique properties, they have been used in various chemical and biological processes. They have been used as electrolytes in batteries and fuel cells. Recently they have been used as thermal fluids because of their high thermal stability and heat capacity. Figure 5-18 lists various applications of ionic liquids [101].

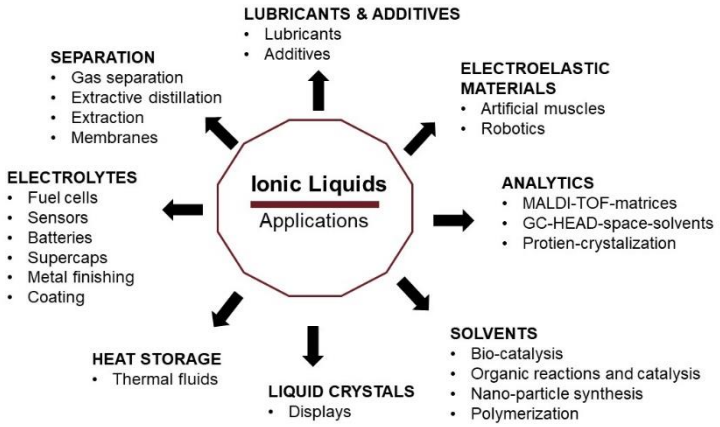

Figure 5-18 Applications of Ionic liquids.

The ionic liquid we used is called the BMIM-PF_6 which is a viscous, colorless, hydrophobic and non-water-soluble ionic liquid with a melting point of -8 °C. Together with 1-butyl-3-methylimidazolium tetrafluoroborate, BMIM-BF_4, it is one of the most widely studied ionic liquids. It is known to decompose very slowly in the presence of water [102]. The chemical structure is shown in Fig. 5-19. It consists of BMIM cation and PF_6 anion.

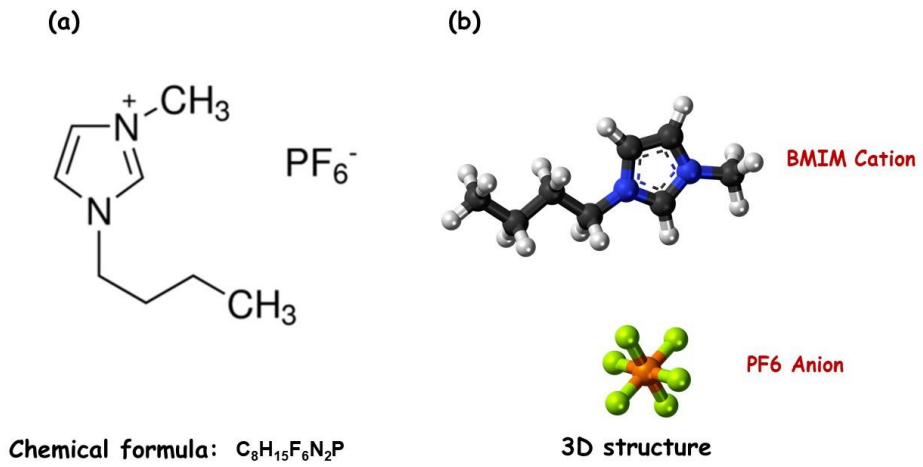

Figure 5-19 Chemical formula of ionic liquid BMIM-PF_6 [102].

Aqueous solution (AQ): To make the aqueous solutions, glycerol was mixed with DI water at 5 different concentrations to get 5 combinations of compound droplets with different viscosity ratios while keeping the surface tensions constant as presented in Table 5-1.

Table 5-1 Properties of liquids used in the experiment*

Liquid	Glycerol % in DI water	Density (g/ml)	Viscosity (mPa.s)	Viscosity ratio with IL(μ_{IL}/μ_{sol})	Surface tension (N/mm)

Solution 1	0	0.05161	1.005	230	72
Solution 2	30	1.04347	2.50	92	
Solution 3	40	1.03945	3.72	62	65.9
Solution 4	80	1.0175	60.1	4	64.3
Solution 5	90	1.0109	219	1.05	64.3
Ionic liquid (BMIM PF6)	-	1.360	231	-	44.8

* Properties are taken at room temperature and pressure (20° C, 1 atm) [103].

Other operating conditions: Both liquids were dispensed into reservoirs and top plate was kept on top of the spacers thus completing the sandwiched device assembly. The gap between top and bottom plates of devices was kept at 100 μm for all cases. A voltage of 110 V and 130 V at 1 KHZ frequency was applied. During the tests, a Hirox camera was used and videos were captured for visualization and further analysis.

5.3.3 Preparing the Multiphase Droplet

First a multiphase droplet was formed by merging two individual droplets. Two separate reservoirs were reserved for generating individual droplets of aqueous solution and ionic liquid. Droplets were first generated and then taken to the middle portion of the device to merge together and form the multiphase droplet. After that, appropriate actuation schemes were utilized to separate the multiphase droplets. One requirement that needs to be fulfilled for maintaining consistency in the test results was to keep the same volume of two phases. For this reason, L-junction reservoirs were used to generate the individual droplets. L-junction reservoirs can provide better consistency and accuracy in the volume of the generated droplets [95]. The details of the droplet generation steps can be found in [95]. After generating two droplets from two reservoirs, they were

brought in the splitting section and merged together. Multiphase droplets were spontaneously created and remained there until the next operation.

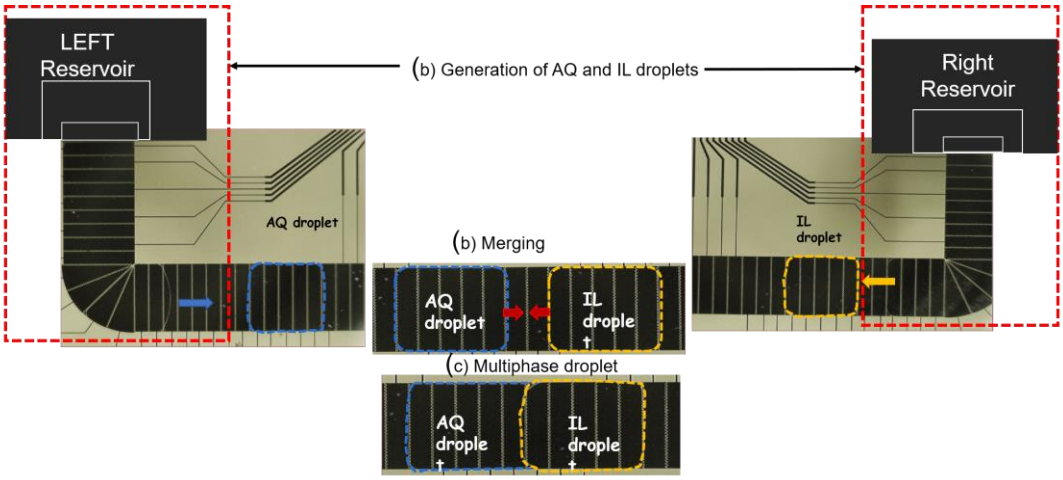

Figure 5-20 (a) Generation of AQ and IL droplets in separate reservoirs. (b) Merging the generated droplets. (c) Multiphase droplet.

Figure 5-20 shows the snapshots of the multiphase droplet formation from experiments. First an Aqueous droplet (AQ) is formed on the left reservoir and an ionic liquid droplet (IL) is formed on the right reservoir (Fig. 5-20(a)). These two droplets are then transported toward each other until they merge (Fig. 5-20(b)). After they came into contact, they were kept in their places while they spontaneously formed the multiphase droplet (5-20(c)).

5.3.4 Data Acquisition and Analysis

Images were extracted from the captured videos and using ImageJ software (NIH), droplet volume, velocity, droplet footprint perimeters were measured. These parameters were further used to calculate different dimensionless numbers.

5.3.4.1 Measuring residue volume

Residue volume is calculated as a percentage of the other phase in the primary phase after the phase separation. To get this value, initial and final volumes of both the phases were measured. The difference in the two volumes in the residue forming phase is the total residue. By using ImageJ, droplet footprint area was first calculated and then volume was derived by multiplying the area with the height of the channel gap. Finally, residue performance was evaluated in terms of residue percentage. A lower number was related to better separation performance.

5.3.4.2 Measuring Velocity

For measuring velocity, *v,* a point on the advancing meniscus of each phase was identified. After Δt time, the distance travelled by the those two points, *d* was measured and following equation was used to calculate droplet velocities:

$$v = \frac{d}{\Delta t} \tag{5.3}$$

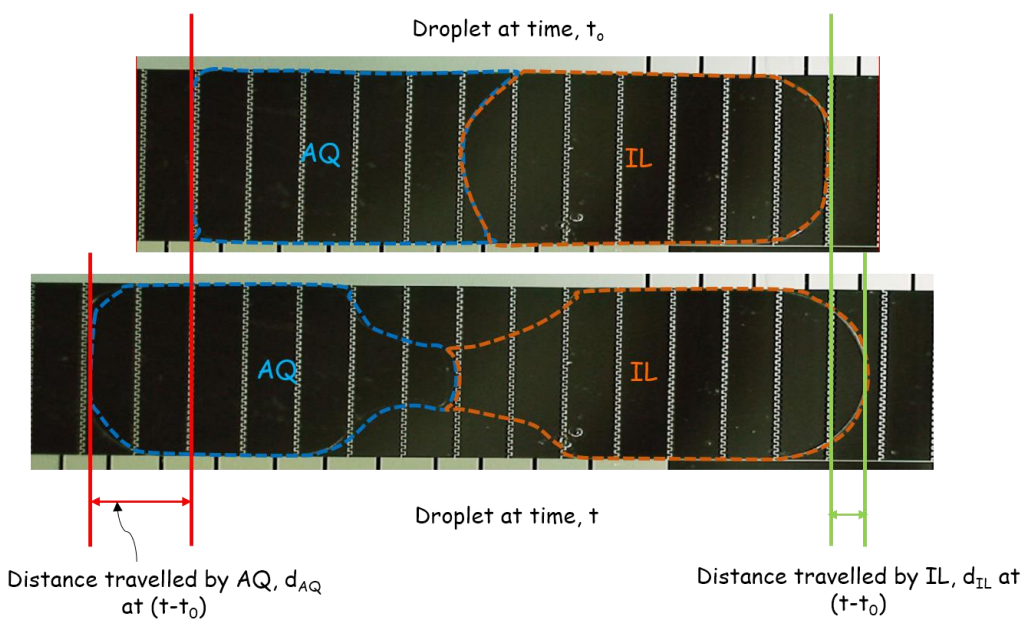

Figure 5-21 Velocity measurement of AQ and IL phase.

Since, the two phases deformed differently and they shared an interface, only one point on the advancing meniscus of each phase was considered to calculate their respective velocities. So, the phase velocities in this study is basically the velocity of the interface facing the activated electrodes. After finding the instantaneous velocities for each phase, time averaged velocities were calculated. Later they were used to calculate time averaged values of other dimensionless numbers including Capillary number, Ca.

5.3.4.3 Measuring Capillary Number, Ca

Capillary number, Ca=$\frac{\mu \mathbf{U}}{\sigma}$ measures the relative strength of viscous force to surface tension force, where μ is the viscosity, σ is the surface tension between the droplet and the medium, U is the velocity. Unlike the continuous microfluidics, measuring capillary number is complicated in digital microfluidics mainly because of two reasons. Firstly, the motion is strictly discrete in nature. Secondly, droplet undergoes deformation. As a result, velocities at each point inside the droplet vary a lot both in temporal and spatial manner. To simplify the calculation, instantaneous velocities of the droplet fronts along the longitudinal centerline at right and left sides comprising of two distinct phases were measured. This measurement technique is very similar to the one reported by Bhattacharjee et al. [93]. After measuring the instantaneous velocities, time averaged values were calculated and based on that, Ca numbers were calculated for respective phases.

5.3.4.4 Deformation number, D

In the literature, deformation has been quantified using a number known as the deformation number, D [79]. In all cases, the deformed droplet has been considered as an ellipse and the ratio of the length of major and minor axis have been used as an

estimate for D. In our study, the droplet deviates significantly from an ellipse and takes an irregular shape. For this reason, assuming it to be an ellipse will give inaccurate deformation number. Therefore, we redefine the deformation number as the following:

$$D=\frac{\text{Perimeter of deformed droplet,P at time t}}{\text{Perimeter of undeformed droplet,}P_o\text{ at t=0}} \tag{5.4}$$

Using the above expression, deformation number for both phases were calculated by measuring the length of the perimeter for each one (Fig. 5-22). As before, we measured the perimeters of each phase at initial time t when they are undeformed. After Δt time, we measured the deformed perimeters for both phases and take the ratio respective to the initial perimeter for each phase. This gave us the instantaneous deformation number, D after Δt time. We repeated this step until the phases separated. From the instantaneous deformation numbers and total time of the process, time averaged deformation number was calculated.

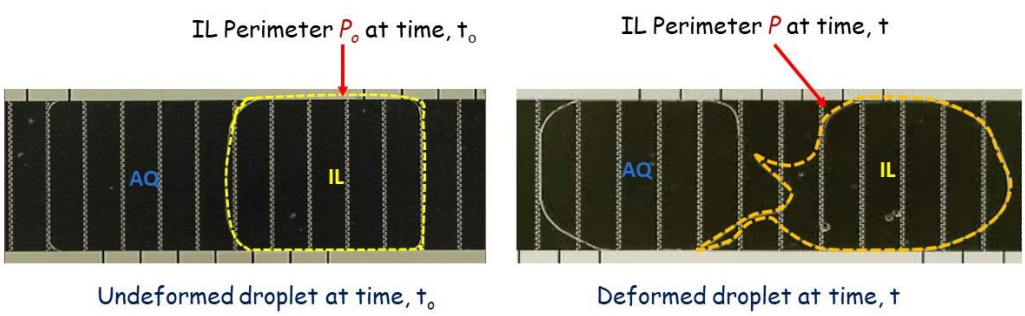

Figure 5-22 Measuring perimeter for calculating deformation number. Perimeter at time to is denoted as Po and perimeter at time t is P. Deformation number, D is calculated as, $D=\frac{P}{Po}$.

5.3.5 Characterization Parameters

Tests were performed to understand the effects of different experimental parameters on separation. Both fluid parameters and splitting technique were considered. Below are the parameters that were studied in details to understand asymmetry of splitting in case of multiphase droplets.

5.3.5.1 Actuation schemes

We discussed about droplet deformation in our previous publication [12]. Our findings suggested that, besides the viscous forces, contact line pinning, and contact angle hysteresis, the way that the force is applied on the droplets to actuate them has a significant role on how they would deform. Wetting force stretches the droplet meniscus towards active electrode (V>0) until it overlaps with the whole surface and dewetting force (capillary force) naturally pulls the meniscus inward on ground electrodes. Droplet transitioning from active to ground electrodes deform because of the contact with both active and ground electrodes. By minimizing the overlap of droplet footprint with any ground electrode, deformation can be minimized. Dewetting length is the length along the droplet portion which experiences dewetting and it is taken in the direction of droplet bulk motion (Fig. 5-23(a)). In case of phase separation, we call it the separation length, L_s which is the total length of dewetting in the neck region during pinch-off and corresponds to the length of the central deactivated electrodes. Previously, we were able in controlling deformation by shortening the dewetting length at each transition sequence [12]. For splitting purpose, wetting forces are applied on the meniscus fronts of two separating phases while at the middle, the droplet experiences de-wetting which induces shear stress and initiates necking. Splitting involves a large amount of deformation and we hypothesize that by controlling the amount of the exposure to dewetting forces in the droplet mid region, it is possible to change the dynamics of necking and outcome of the

separation process. As shown in Fig. 5-23(b), separation length is the distance that two phases will move apart after they have been separated from each other which is analogous to the cutting length for splitting. This is equal to the summation of the dewetting lengths for the two individual phases at the moment of separation.

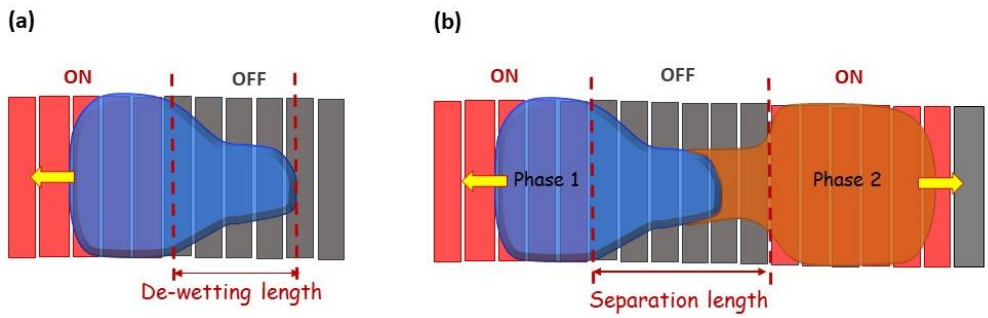

Figure 5-23 De-wetting length of a droplet transitioning from ground electrodes to active electrodes. (b) Separation length of a compound droplet during phase separation process. The arrows show the direction of fluid motions. RED colored regions represent active electrodes and the GREY regions depict grounded electrodes.

In context of tuning the separation length, we introduce different schemes. Conventionally, droplet spitting has been performed by using square shaped electrodes and separation lengths are always even multiples of the dimension of a square electrode. So, we consider this as our reference and term it as “SQ” method.

We step down the separation length in SL schemes with using slender electrodes where the electrodes are rectangular strips with much shorter width, w. Width, w of a square electrode comprises of five slender electrode widths combined. We start with switching off two electrodes at the middle in the first sequence and turn on one electrode on each side of the droplet. We keep adding the grounded and active electrodes by two in each sequence. We name this scheme as SL1.

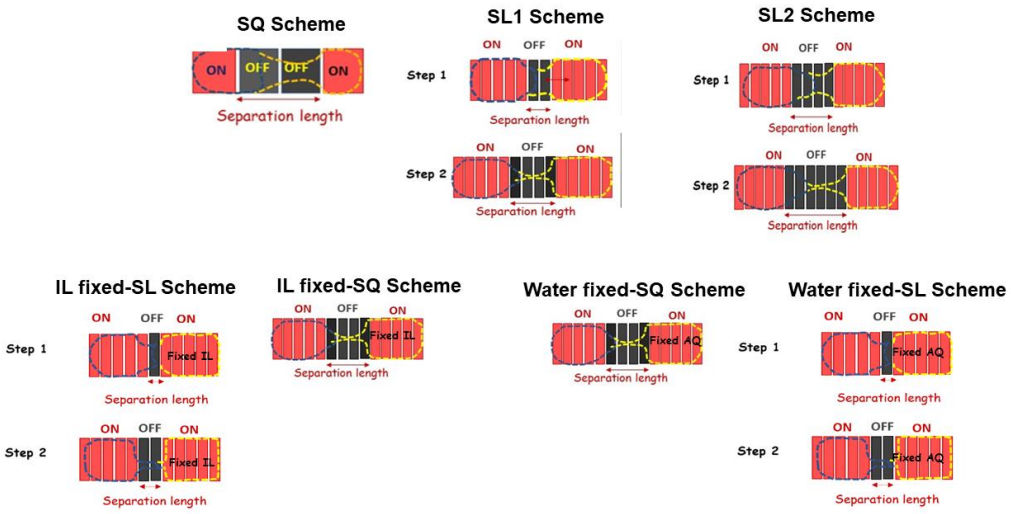

Figure 5-24 Different actuation schemes for separation.

We define SL2 schemes where total of four electrodes are turned off and four electrodes are turned on at each sequence. This is repeated until the pinch-off happens. We also introduce IL fixed-SL, IL fixed-SQ, water fixed-SL and water fixed-SQ scheme where one phase is kept still and the other phase is being pulled by using either SQ or SL1 scheme.

5.3.5.2 Viscosity ratio, λ

Another important parameter that can change the deformation dynamics as well as the necking mechanism is the viscosities of the fluid phases involved. In our study, the viscosity of ionic liquid (IL) phase was kept constant while we changed the viscosity of the aqueous solution (AQ) phase. Five different viscosity ratios were considered, ranging from 1 up to 230.

5.3.5.3 Applied voltage, V

During separation, velocities of the interface play role in necking. In our experiment, velocities were directly controlled by varying the applied voltage. 110V and

130V were used. Applied voltage affects droplet velocity since different actuation forces result from different voltages. Both Capillary number, Ca and Electrowetting number, E can vary with varying voltage. Table 5-2 lists all the experiments that we performed by varying the three characterization parameters.

Viscosity ratio	Both phases move						One phase fixed							
	SQ		SL1		SL2		IL fixed-SL		IL fixed-SQ		Water fixed-SL		Water fixed-SQ	
	110V	130V	110V	130V	110V	130V	110V	130V	110V	130V	110V	130V	110V	130V
1														
4														
62														
130														
230														

5.4 Experimental Observations

5.4.1 Effects of actuation schemes

5.4.1.1 Both phases are pulled apart

SQ Scheme: De-wetting length or cutting length, L_s has two effects-droplet morphology is affected [12] and velocity of the two phase-fronts are influenced. Consequently, phase dynamics give rise to variation in the location and time of the neck formation and eventually the performance of separation. Keeping the viscosity ratio equal to 1, the factor contributing to differences in the dynamics is the separation distance that allows the droplet to get stretched within a limit. As can be seen from Fig. 5-25 (TOP), both of the phases are more elongated with the SQ scheme, where additionally the

chance for hydrodynamic instability to play role in asymmetric positioning of the "separation point" is comparatively more than in the case of SL schemes.

For the SQ scheme, the phases are allowed to be elongated over a separation distance of 4.8 mm at one sequence. Because of higher value of capillary number of the IL phase which results from higher velocity of the phase-front and lower surface tension (λ=1; (σ_{IL}=.05 N/m) <(σ_{AQ}=.069 N/m), IL phase deforms more than AQ phase. While IL phase-front moves rapidly to the active electrodes on right, AQ phase moves very slowly toward left active electrodes. Higher velocity of IL phase (v_{IL}/ v_{AQ} ~3) is resulted from higher electrowetting number (E_{IL}/E_{AQ} ~1.4). Velocity gradient inside the IL phase is very high because of the apparently zero velocity at the interfacial region and high velocity at the leading meniscus. Very large deformation is thus a consequence of both large Ca and large velocity gradient. As discussed earlier, necking is initiated by the concave radius of curvature of the meniscus formed by the de-wetting on separating electrodes. Higher electrowetting number, E facilitates the neck formation [93, 100] and as observed in our experiment, neck is favorably formed in the IL phase which is highly deformed and have higher Electrowetting number, E. These observations are repeated in all other cases except for few which will be discussed later. Unequal Electrowetting and Capillary numbers cause different amount of deformation in both of the phases and adversely affect the symmetric splitting. As a result, separation happens at an off-center position away from the interface and residue is left from IL phase into AQ phase as shown in Fig. 5-25 (top (vi)).

SL1 scheme: For SL1 scheme, the separation length, L_s is ~2.4 mm. Because the separation distance is increased in steps with increments of 1.2 mm, deformation and velocity are mechanically controlled. The effects are obvious in Fig. 5-25 (middle). This time, deformation of IL phase is less and velocity gradient is reduced. Still, average

velocity of the IL front is 3 times that of AQ, and Ca is also higher. Therefore, the neck forms on IL phase although it is now much closer to the interface and asymmetry of necking is minimized. The amount of residue is comparatively less from the previous case (Fig. 5-25(middle (vi)) and Fig. 5-25 (top.vi)).

For scheme SL2 (Fig. 5-25 (bottom)), although the final separation distance is same as that of SL1 (2.4 mm), the electrodes (4 slender electrodes) forming the separation length are turned off simultaneously. So, deformation is less controlled and chances for hydrodynamic instability is more. Compared to SL1 case, higher velocity gradient is observed between the frontal region and back region of the IL. However, the deformation is still better controlled than SQ case, and the necking also happens more symmetrically than SQ scheme. The amount of residue is less than SQ scheme but more than SL1 scheme.

5.4.1.2 One phase is kept still

Based on the above observations, it is evident that the different schemes were able to provide different separation lengths and ways to vary deformation and velocity gradients inside particular phase. For all above cases, IL phase experiences more deformation. Therefore, another technique is introduced where the IL phase is kept still in its initial position so that its shape is retained (Fig. 5-26). Now the AQ phase is pulled to the left side by providing separation length by using SL1 scheme. In these situations, necking now happens very close to the interface producing little amount of residue. Necking happens on AQ phase, since it is the only phase being deformed. AQ inherently has lower capillary number and lower electrowetting number as mentioned before.

The scenario for SQ scheme is repeated for the case when IL is being held in the initial position and AQ phase is moved by electrowetting force. In terms of symmetry of

necking, it is poorer compared to the previous one, but still the separation performance is better than SQ scheme because of smaller separation length ($L_{s(Fixed\ IL\text{-}SQ)} < L_{s(SQ)}$).

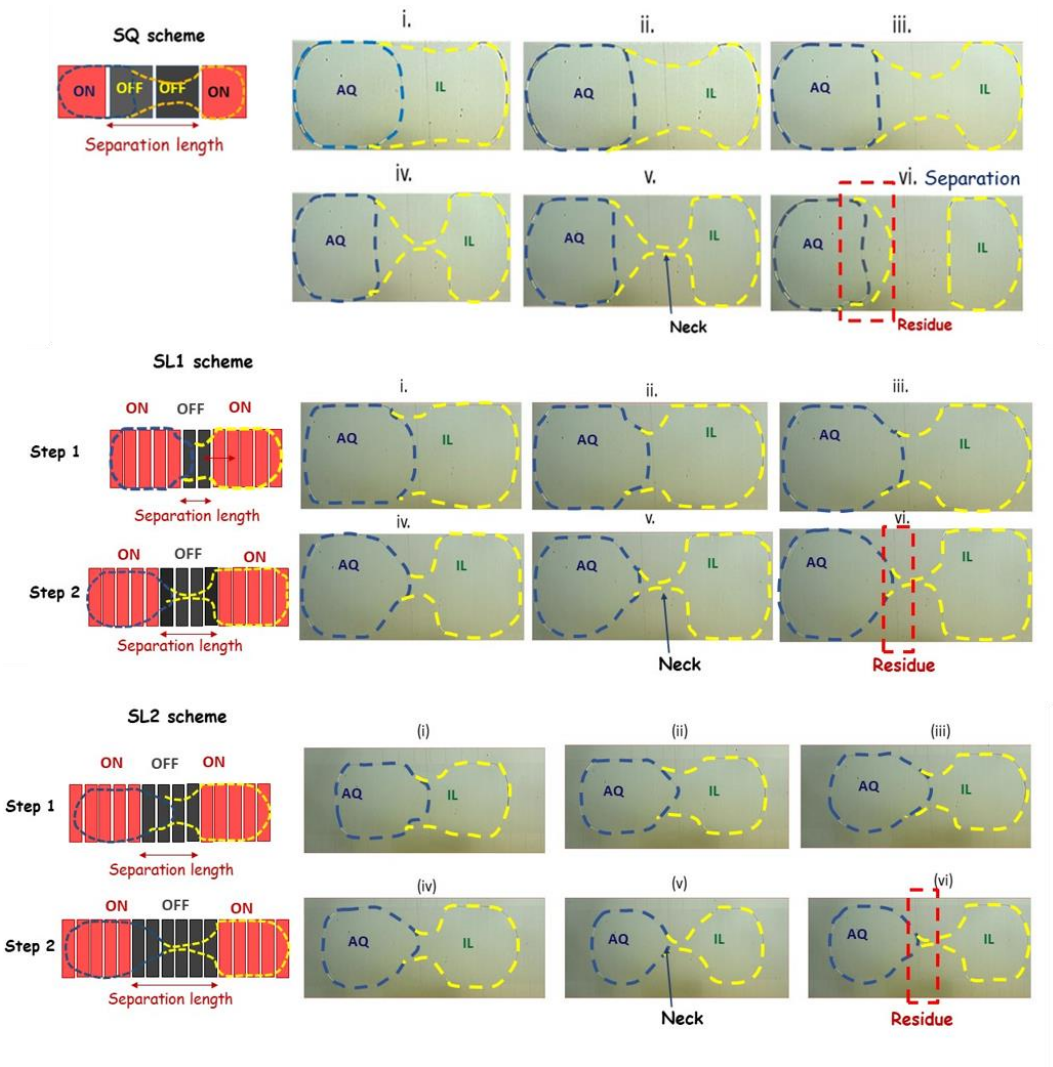

Figure 5-25 Profiles of deformed droplet at different time instants until the moment of separation. Top: SQ scheme, Middle: With SL1 Scheme and Bottom: With SL2 scheme. IL phase is on the RIGHT and AQ phase is on the LEFT always.

Results were not favorable in terms of separation performance when AQ phase was kept fixed at its initial position. Because IL phase was the neck forming face, no matter what scheme was used (SQ or SL), deformation was more than the case of AQ being the neck forming phase. Nevertheless, separation was better for AQ fixed-SL scheme than that of AQ fixed-SQ scheme than that of AQ fixed-SQ scheme.

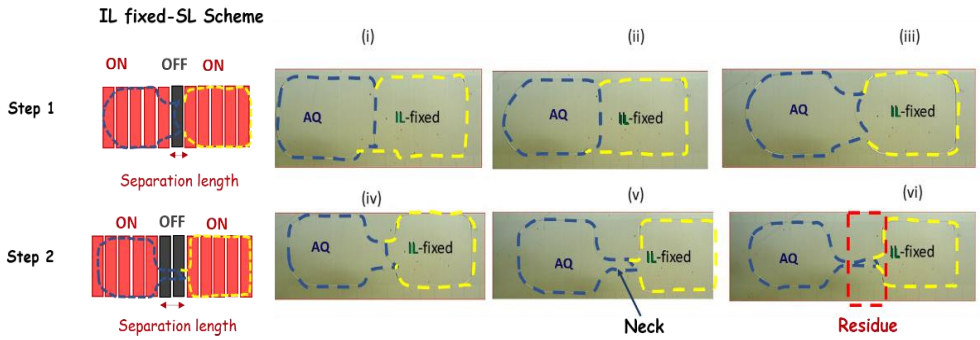

Figure 5-26 Droplet profiles for scheme IL fixed-SL.

Figure 5-27 is a representation of the effects of different schemes on residue formation. Each column represents the average value of the residue percentage for a particular scheme. The average for one specific scheme is calculated considering the residue values for all viscosity ratios and two different applied voltages. As shown in the figure, the first three columns are for the cases when both phases are pulled towards opposite directions. As we go from left (SL1 scheme) to the right (through SL2 to SQ scheme) columns, separation length increases, and residue percentage also increases. Compared to SQ scheme, SL1 and SL2 scheme produce very less residue. As predicted before, SL1 scheme gives the least residue which is only 1 % with a very small standard deviation whereas in SQ scheme, residue is as high as 17% with a standard deviation of 6. SL2 scheme is better than SQ scheme with a residue of 2.7 %. It should be noted that,

with the increase in separation length (from SL1 through SL2 to SQ), not only the residue but also the standard deviation increases. Which means, by using SL schemes, droplet behaviors can be predicted with better consistency. Whereas, with SQ schemes, the uncertainty increases with increased probability of hydrodynamic instability. The last four columns in Fig. 5-27 stand for the schemes with one fixed-phase. The trends observed for the first three columns in Fig. 5-27 still hold true. As before, smaller separation length (IL fixed-SL, Water fixed-SL scheme) is associated with less amount of residue. IL fixed-SL scheme gives 1.1% residue which is as good as the SL1 scheme. Again, for water fixed-SQ scheme, the average residue is 14% which is 12% more than its SL counterpart. IL fixed-SQ scheme is an improved version of SQ scheme, where the residue is almost 3% with a v ery low standard deviation.

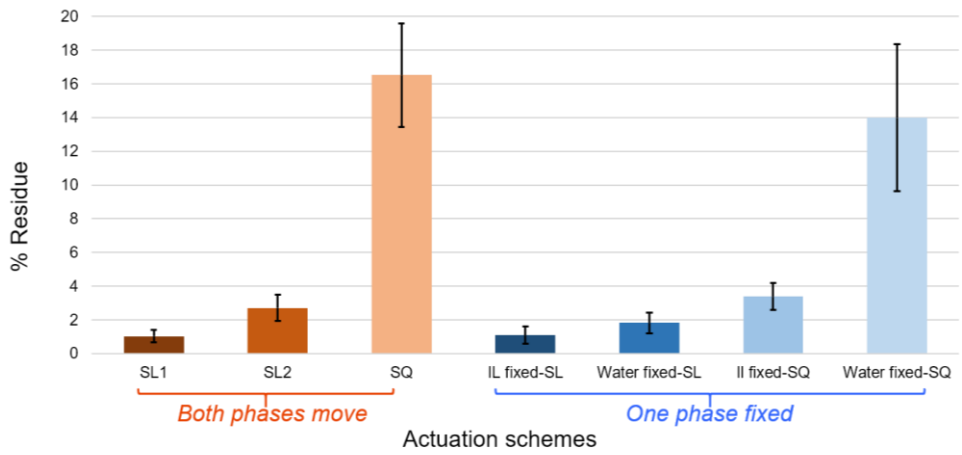

Figure 5-27 Amount of residue for different schemes. The ORANGE columns represent the cases where both phases are moved and the BLUE columns represent the cases where one phase is kept still while the remaining phase is moved. Error bars represent standard deviations.

5.4.2 Effects of viscosity ratio, λ

In our experiments, viscosity of aqueous solution of glycerol (AQ) was varied by mixing glycerol with DI water to create liquid pairs of aqueous solution (AQ) and Ionic liquid (IL) with viscosity ratios, λ (μ_{IL}/μ_{AQ}) of 1, 4, 62, 130 and 230.

Figure 5-28 shows the average residue (%) values at different viscosity ratios. For any viscosity ratio, average value was calculated over all the actuation schemes and the two applied voltages. As viscosity ratio increases, separation performance gets better. At viscosity ratio of 230, % residue is approximately 3% which is almost half of the residue (%) at viscosity ratio of 1. Interestingly, at three intermediate viscosity ratios, change in percentage residue is not very significant. Additionally, as the viscosity ratios get smaller, we observe the standard deviations to be larger. For example, a standard deviation of 9 is observed for λ =1 whereas for λ=230, standard deviation is 2.

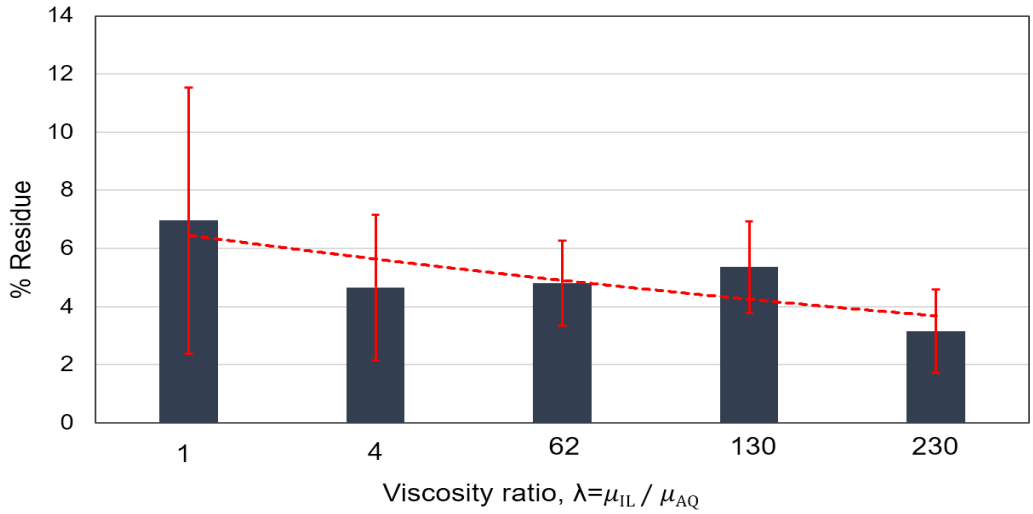

Figure 5-28 Amount of residue (%) for different viscosity ratios. The error bars represent the standard deviations.

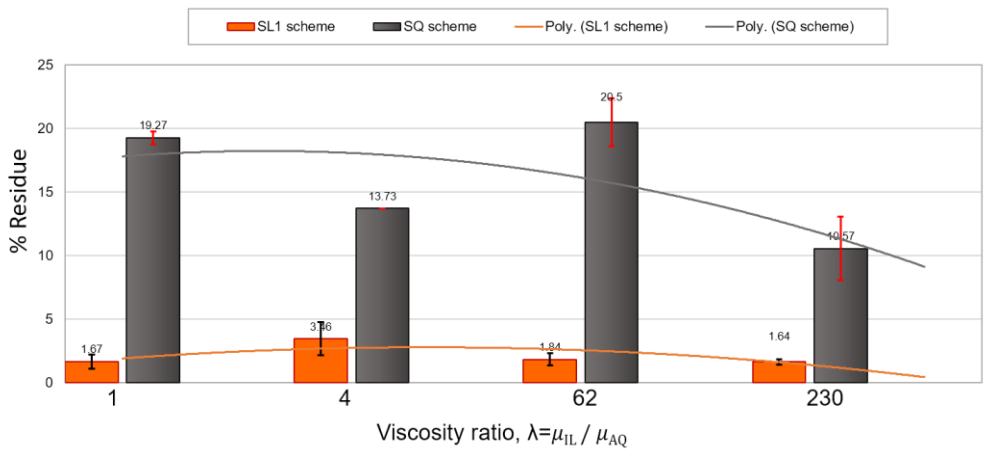

Figure 5-29 Amount of residue for different viscosity ratios for SL1 and SQ scheme.

The large standard deviations arise from the large differences in residue between the schemes. It can be clearly explained by using Fig. 5-29. Here, residue % is plotted for scheme SL1 and SQ at different viscosity ratios. It is seen that, both of the schemes, specially SL1 scheme, have very small standard deviations. However, the difference between the residues of these two schemes at any particular λ is very high. For example, at λ=1, the difference is about 17.5%. At λ=230, it is about 9%. As these differences in percentage residue between schemes gets smaller at higher viscosity ratios, standard deviations also decrease which is shown in Fig. 5-28.

5.4.3 Effects of applied voltage

The separation process in this study was achieved using electrowetting as the actuation method where the actuation force is a function of applied voltage. By keeping all system parameters same, the effects of varying voltage on force can be realized by analyzing electrowetting number, E which is given by Eq. 5.5:

$$\mathrm{E} = \frac{\varepsilon_o \ \varepsilon_r \ V^2}{2d\sigma} \tag{5.5}$$

Here, ε_o is the vacuum permittivity, ε_r is dielectric constant, d is the thickness of dielectric layer and V is the applied voltage. Electrowetting number represents the relative dominance of electrowetting effect over capillary force. Below saturation limit, droplet velocity increases as applied voltage increases. In other words, with increase in electrowetting number, E, velocity increases [100]. Now keeping the above theory in mind, let us see the effects of voltage on separation using Fig. 5-30. The average was taken by considering residue values for all the viscosity ratios and all schemes. It is evident that, voltage has very minor effect on residue formation at least in the small range of applied voltage (110V-130V). Between 110V and 130V, the difference in residue is less than 1%. However, the presence of very large standard deviations suggest a dominance of other parameters specially the actuation schemes on amount of residue.

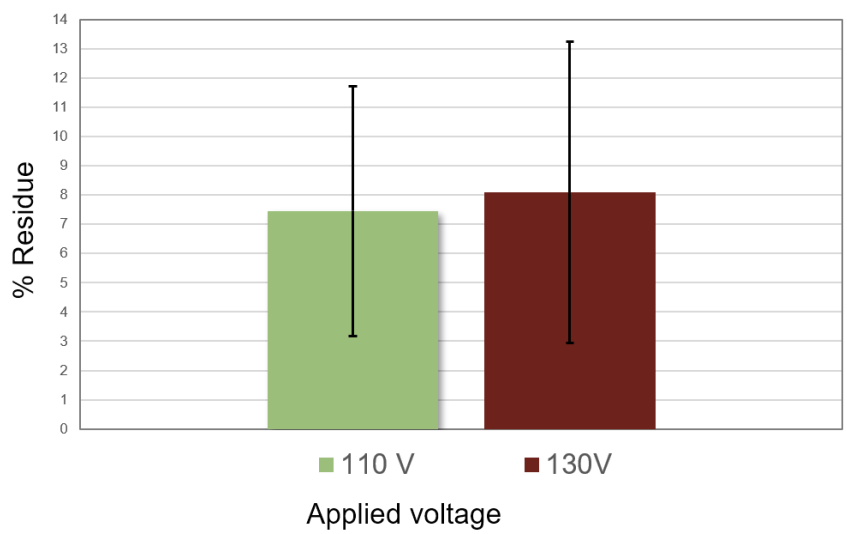

Figure 5-30 Amount of residue for different applied voltages.

We anticipate that, there can be visible effects of applied voltages if we consider a wider range (70 V-150 V). Also, the effects of applied voltage can vary according to the actuation schemes. As to check whether it is true, we plotted the average residues for

different schemes by averaging them over all the viscosity ratios. The results are shown in Fig. 5-31. We can divide the schemes into two categories where in one category of schemes, the separation lengths are shorter and deformations are well controlled. For these cases, applying higher voltage results in reduced amount of residue for all viscosity ratios. Since there is more control on velocity, velocity in the direction of motion is not increased significantly although the surface energy is more which means better wetting is provided by electrowetting. As a result, droplet shapes conform better with the areas of activated electrode and less amount of liquid contribute to form the tail (Fig. 5-32). On the other hand, for the schemes with less control on separation length or deformation (such as SQ scheme) separation performance deteriorates at higher voltage. This might be caused by the fact that, due to less control, velocity in the direction of motion is significantly increased in response to the increased electrowetting number and hydrodynamic instability gets more probable. A as SL2 or SQ), (highlighted with red dashed lines in Fig. 5-31) typically separation longer tail is formed and more liquid is added to the residue (Fig. 5-33).

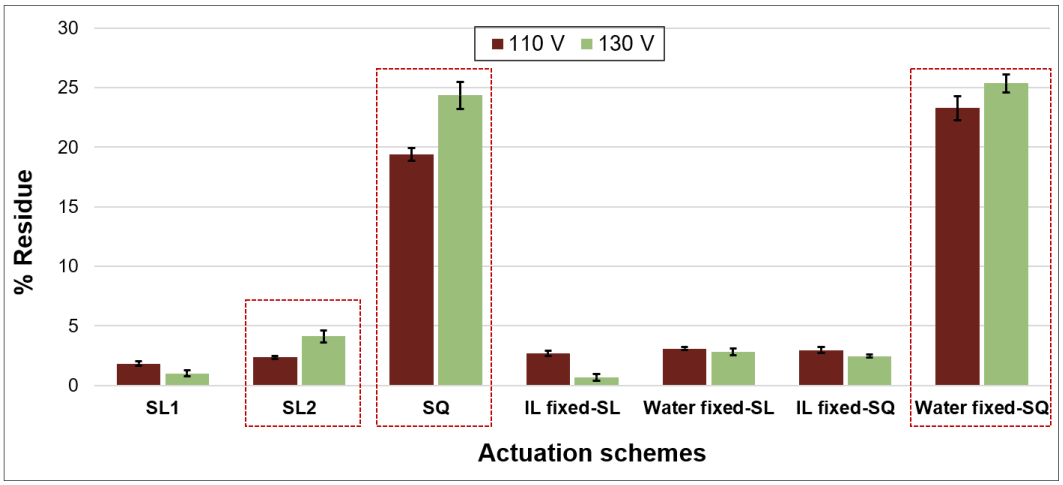

Figure 5-31 Amount of residue for different actuation schemes at viscosity ratio of 1 for different voltages.

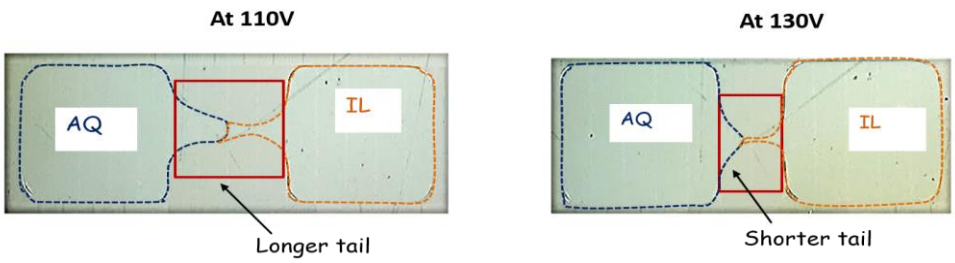

Figure 5-32 Droplets just before separation for SL1 scheme at 110 V and 130 V for viscosity ratio of 62.

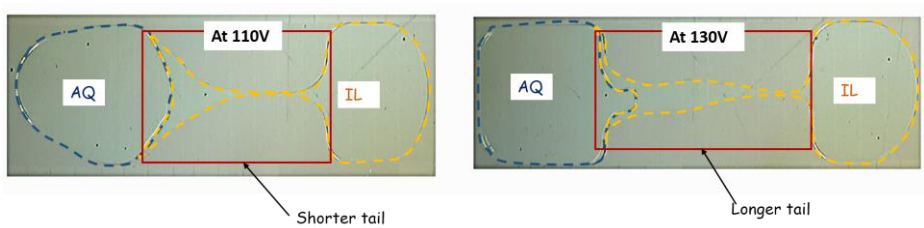

Figure 5-33 Droplets just before separation for SQ scheme at 110 V and 130 V for viscosity ratio of 62.

5.5 Results and Discussions

Since, the capillary number of AQ is very small, deformation of AQ is relatively smaller than IL for most of the schemes (other than IL fixed schemes). In these situations, given that each phase has equal volume, IL acts as the neck forming phase due to its higher deformability and residue from IL phase is left in AQ phase after separation. From here, we can generalize that, if the capillary number of two phases are significantly different, the neck formation occurs in the phase with higher capillary number. In this scenario, we can also assume that, since neck forming phase is capable of deforming at a much higher degree, the dynamics of the remaining phase does not play any significant role in the separation. Therefore, we can focus our attention on the dynamics of the phase having the neck and consider the separation process as the single droplet splitting.

The difference between the deformation numbers of two phases is a measure of residue formation. For that reason, we quantify this by taking the ratio of two deformation numbers representing the two phases and name it as Chi, χ. Figure 5-34 is a plot of amount of residue (%) as a function of χ. As shown in the plot, as χ increases, amount of % residue increases. That means, if two phases deform in equal amounts, necking is more symmetric and it will more likely coincide with the interface. On the other hand, higher χ means, more mismatch between deformation and asymmetry in necking is more. It can be noted that, in about 71% of the cases, amount of residue is less than 2 % when χ is between 1 and 1.25. For higher values, % residue is also higher.

Next, we plot the amount of residue as a function of capillary number, Ca of IL, CaIL (Fig. 5-35). It is seen that, for different viscosity ratios of the fluids, amount of residue changes at varying degree. Nevertheless, for all of the cases, as capillary no., CaIL increases, % residue also increases. If the viscosity ratio is less (λ=1), amount of residue increases more sharply with increase in capillary number. For the highest viscosity ratio, λ=230) the graph is almost flat-which means amount of residue is not affected much by the increasing capillary number and it gives the least amount of residue.

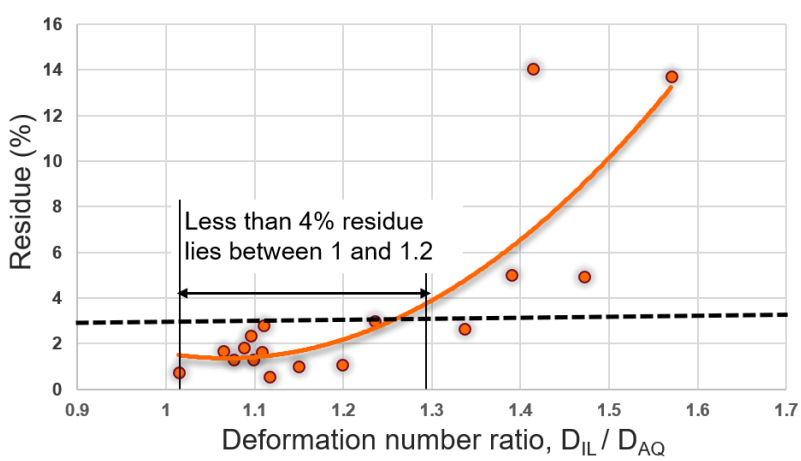

Figure 5-34 Deformation number ratio, χ vs amount of residue for different viscosity ratios.

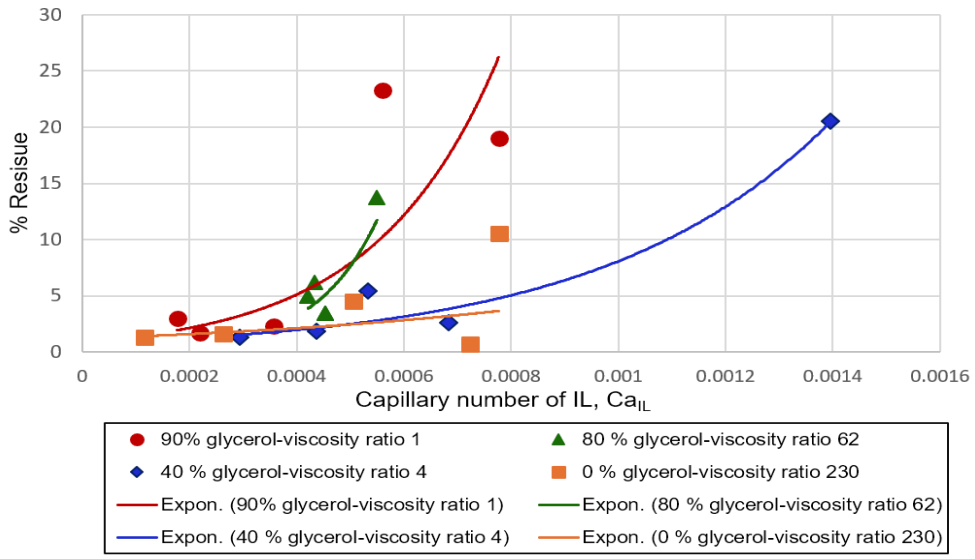

Figure 5-35 Amount of residue vs. capillary number, Ca_{IL} for different viscosity ratios.

Figure 5-36 shows the relation between residue % and electrowetting number. Electrowetting number can be changed by changing the device parameters such as dielectric constant or fluid properties such as surface tension or by changing the applied voltage. Since, all the other parameters were kept constant in our tests and the applied voltage was varied within a very small range, we do not expect to see any significant effect of electrowetting number on percentage residue. In our study, we consider two electrowetting numbers, E1 =.585 (applied voltage=110 V) and E2 =.818 (applied voltage=130V) for viscosity ratio, λ of 62 (40% glycerol). For higher applied voltage (E2 =.818), separation is slightly better in general but there is more inconsistency specially at higher capillary numbers. On the other hand, at lower voltage (E1 =.585), amount of residue consistently increases with capillary number with steeper slope.

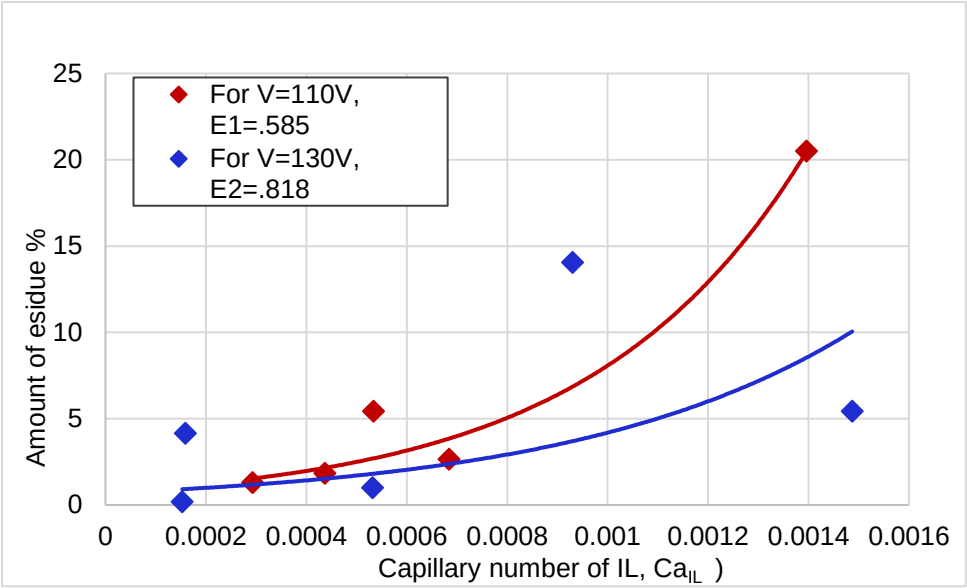

Figure 5-36 Amount of residue as a function of capillary number for different electrowetting numbers for viscosity ratio of 62 (40% glycerol).

Finally, table 5-2 shows the summary of our experiment. Best separation is achieved for lowest separation length with scheme IL fixed-SL at higher voltage (V=130 V), for viscosity ratio of 230 where residue is less than 1 %.

5.6 Conclusions

Symmetry of the splitting mechanism is the fundamental principle we need to focus on to achieve better separation. Deformation of two phases should be controlled in a way that the deformation numbers match with each other or the capillary number of both phases should closely match with each other. The most significant parameter in controlling residue formation is the actuation schemes where SL1 scheme offers the best performance and SQ scheme has the worst. The second most important parameter is the

viscosity ratio where higher viscosity ratio is better. Finally, there was no observable effects of applied voltage on residue %. To get better separation performance, the most suitable parameter to control is the actuation scheme and it should be tuned with the other parameters so as to reduce the difference in capillary numbers and amount of deformations of two phases.

Table 5-2 Summary of Experimental Results

Viscosity Ratio	Schemes																											
	SL1				SL2				SQ				Water fixed-SL				Water fixed-SQ				IL fixed-SL				IL fixed-SQ			
	110V		130 V		110V		130V		110V		130V		110V		130V		110V		130V		110V		130V		110V		130V	
	AVG	STD	AVG	STD	AVG	STD	AVG	STD	AVG	STD	AVG	STD	AVG	STD	AVG	STD	AVG	STD	AVG	STD	AVG	STD	AVG	STD	AVG	STD	AVG	STD
1(90%)	1.82	0.42	1	0.482	2.34	0.227	4.2	0.991	19.27	1.05	22.83	3.33	2.99	0.24	2.79	0.56	23.3	1.99	25.4	1.46	2.68	0.49	0.67 (IL)	0.57	2.96	0.46	2.72 2.44	0.249
4 (80%)	3.46	0.924	1.29	0.55	6.21	1.56	3.18	0.51	13.73	-	16.7	1.913	1.09	0.06	1	0.178	4.94	1.64	7.26	0.527	0.56	0.28	2.48	-	2.12	0.75	5.07	1.13
62 (40%)	1.84	0.91	0.48	0.39	2.67	0.99	4.14	2	20.5	3.78	14.05	2.96	1.3	0.35	1.05	0.19	5.43	1.21	13.25	0.12	0.65	0.66	0.31	-	5.47	1.43	2.37	1.08
92 (30 %)	0.393	.3653			3.410	2.37			15.86	5.677																		
230 (0 %)	1.64	0.217	0.227	0.118	1.32	0.59	0.947	0.979	10.57	0.963	5.065	1.157	0.74	0.61	0.538	0.065	4.52	2.05			6.87				3.16	0.76		

References

1. Lee, J., Moon, H., Fowler, J., Kim, C. J., & Schoellhammer, T. Addressable micro liquid handling by electric control of surface tension. In *Micro Electro Mechanical Systems, 2001. MEMS 2001. The 14th IEEE International Conference on* (pp. 499-502). IEEE.
2. Pollack, M. G., Fair, R. B., & Shenderov, A. D. Electrowetting-based actuation of liquid droplets for microfluidic applications. *Applied Physics Letters*, 2000. *77*(11), 1725-1726.
3. Gascoyne, P. R., Vykoukal, J. V., Schwartz, J. A., Anderson, T. J., Vykoukal, D. M., Current, K. W., & Andrews, C. Dielectrophoresis-based programmable fluidic processors. *Lab on a Chip*, *2000. 4*(4), 299-309.
4. Darhuber, A. A., Valentino, J. P., Troian, S. M., & Wagner, S. Thermocapillary actuation of droplets on chemically patterned surfaces by programmable microheater arrays. *Journal of Microelectromechanical Systems, 2003*. *12*(6), 873-879.
5. Sammarco, T. S., & Burns, M. A. Thermocapillary pumping of discrete drops in microfabricated analysis devices. *AIChE Journal*, *1999*. *45*(2), 350-366.
6. Mugele, F., & Baret, J. C. Electrowetting: from basics to applications. *Journal of Physics: Condensed Matter*, *2005. 17*(28), R705.
7. Fan, Shih-Kang, Yao-Wen Hsu, and Chiun-Hsun Chen. Encapsulated droplets with metered and removable oil shells by electrowetting and dielectrophoresis. *Lab on a Chip* 11.15 (2011): 2500-2508.

8. Wijethunga, Pavithra AL, and Hyejin Moon. On-chip aqueous two-phase system (ATPS) formation, consequential self-mixing, and their influence on drop-to-drop aqueous two-phase extraction kinetics. *Journal of Micromechanics and Microengineering* 25.9 (2015): 094002.
9. Kunchala, Praveen. On-chip Liquid-liquid Extraction And Separation Using Digital Microfluidics. (2010).
10. Wijethunga, Pavithra AL, et al. On-chip drop-to-drop liquid microextraction coupled with real-time concentration monitoring technique. *Analytical chemistry* 83.5 (2011): 1658-1664.
11. Nahar, Mun Mun, et al. "Droplet velocity in an electrowetting on dielectric digital microfluidic device." *Micromachines* 7.4 (2016): 71.
12. Nahar, Mun Mun, et al. "Numerical Modeling of 3D Electrowetting Droplet Actuation and Cooling of a Hotspot." *COMSOL CONFERENCE*. 2015.
13. J. Li, Y. Wang, H. Chen, H., and J. Wan, “Electrowetting-on-dielectrics for manipulation of oil drops and gas bubbles in aqueous-shell compound drops,” *Lab on a Chip*, *14*(22), 4334-4337, 2014.
14. D. Brassard, L. Malic, F. Normandin, M. Tabrizian, and T. Veres, “Water-oil core-shell droplets for electrowetting-based digital microfluidic devices,” *Lab on a Chip*, *8*(8), 1342-1349, 2008.
15. https://en.wikipedia.org/wiki/Lab-on-a-chip.
16. https://www.meddeviceonline.com/doc/silicon-a-material-with-huge-potential-for-lab-on-chips-0001.
17. https://www.theengineer.co.uk/issues/march-2011-online/lab-on-chip-device-promises-hiv-diagnosis-in-10-minutes.
18. https://wyss.harvard.edu/technology/human-organs-on-chips.

19. https://www.meddeviceonline.com/doc/silicon-a-material-with-huge-potential-for-lab-on-chips-0001.
20. Temiz, Yuksel, et al. "Lab-on-a-chip devices: How to close and plug the lab?." *Microelectronic Engineering* 132 (2015): 156-175.
21. Gupta, Shagun, et al. "Lab-on-Chip Technology: A Review on Design Trends and Future Scope in Biomedical Applications." *International Journal of Bio-Science and Bio-Technology* 8.5 (2016): 311-322.
22. Chou, Wei-Lung, et al. "Recent advances in applications of droplet microfluidics." *Micromachines* 6.9 (2015): 1249-1271.
23. Seemann, Ralf, et al. "Droplet based microfluidics." *Reports on progress in physics* 75.1 (2011): 016601.
24. Dixon, Christopher, Julian Lamanna, and Aaron R. Wheeler. "Printed microfluidics." *Advanced Functional Materials* 27.11 (2017).
25. https://www.elveflow.com/microfluidic-tutorials/microfluidic-reviews-and tutorials/digital-microfluidics-microfluidic-droplet-emulsion-science/
26. Sukhatme, S., and A. Agarwal. "Digital microfluidics: Techniques, their applications and advantages." *J Bioengineer & Biomedical Sci S* 8 (2012): 2.
27. Bindiganavale, Govindraj, Seung Mun You, and Hyejin Moon. "Study of hotspot cooling using electrowetting on dielectric digital microfluidic system." *Micro Electro Mechanical Systems (MEMS), 2014 IEEE 27th International Conference on*. IEEE, 2014.
28. Shah, G. J., Ohta, A. T., Chiou, E. P. Y., & Wu, M. C. EWOD-driven droplet microfluidic device integrated with optoelectronic tweezers as an automated platform for cellular isolation and analysis. *Lab on a Chip*, *2009. 9*(12), 1732-1739.

29. Paik, P., Pamula, V. K., & Fair, R. B. Rapid droplet mixers for digital microfluidic systems. *Lab on a Chip*, *2003. 3*(4), 253-259.
30. Cheng, J-T., and C-L. Chen. "Adaptive chip cooling using electrowetting on coplanar control electrodes." *Nanoscale and Microscale Thermophysical Engineering* 14.2 (2010): 63-74.
31. Berge, Bnmo. "Liquid lens technology: principle of electrowetting based lenses and applications to imaging." *Micro Electro Mechanical Systems, 2005. MEMS 2005. 18th IEEE International Conference on*. IEEE, 2005.
32. Krupenkin, Tom, and J. Ashley Taylor. "Reverse electrowetting as a new approach to high-power energy harvesting." *Nature communications* 2 (2011): 448.
33. Ni, Q., Capecci, D. E., & Crane, N. B. Electrowetting force and velocity dependence on fluid surface energy. *Microfluidics and Nanofluidics*, *2015.* 1-9.
34. Ren, H., Fair, R. B., Pollack, M. G., & Shaughnessy, E. J. Dynamics of electro-wetting droplet transport. *Sensors and actuators B: chemical*, *2002. 87*(1), 201-206.
35. Yogarajan, M. P., Ibrahim, F., & Soin, N. Effect of electrode geometric parameters on droplet translocation in digital micro-fluidic biosensor. In *4th Kuala Lumpur International Conference on Biomedical Engineering 2008* (pp. 711-714). Springer Berlin Heidelber
36. Mohseni, K., Arzpeyma, A., & Dolatabadi, A. Behaviour of a moving droplet under electrowetting actuation: Numerical simulation. *The Canadian Journal of Chemical Engineering*, *20016. 84*(1), 17-21.

37. Das, D., Das, S., & Biswas, K. Effect of electrode geometry on voltage reduction in EWOD based devices. In *Systems in Medicine and Biology (ICSMB), 2010 International Conference on* (pp. 371-375). IEEE.
38. Bahadur, V., & Garimella, S. V. An energy-based model for electrowetting-induced droplet actuation. *Journal of Micromechanics and Microengineering, 2006. 16*(8), 1494.
39. Rajabi, N., & Dolatabadi, A. A novel electrode shape for electrowetting-based microfluidics. *Colloids and Surfaces A: Physicochemical and Engineering Aspects*, *2010. 365*(1), 230-236.
40. Baird, E. S., & Mohseni, K. A unified velocity model for digital microfluidics. *Nanoscale and microscale thermophysical engineering*, *2007. 11*(1-2), 109-120.
41. Arzpeyma, Alborz, et al. A coupled electro-hydrodynamic numerical modeling of droplet actuation by electrowetting. *Colloids and Surfaces A: Physicochemical and Engineering Aspects, 2008.* 323.1 (2008): 28-35
42. Chatterjee, D., Shepherd, H., & Garrell, R. L. Electromechanical model for actuating liquids in a two-plate droplet microfluidic device. *Lab on a Chip*, *2009*. *9*(9), 1219-1229.
43. Berthier, J., Dubois, P., Clementz, P., Claustre, P., Peponnet, C., & Fouillet, Y. Actuation potentials and capillary forces in electrowetting based microsystems. *Sensors and Actuators A: Physical*, *2007*. *134*(2), 471-479.
44. Jagath B. Yaddessalage. Study of the capabilities of electrowetting on dielectric digital microfluidics (EWOD DMF) towards the high efficient thin film evaporative cooling platform, Doctor of Philosophy, University of Texas at Arlington, (2013).

45. Nelson, Wyatt C., and Chang-Jin ‘CJ Kim. "Droplet actuation by electrowetting-on-dielectric (EWOD): A review." *Journal of Adhesion Science and Technology* 26.12-17 (2012): 1747-1771.
46. Young, Patrick M., and Kamran Mohseni. "Calculation of DEP and EWOD forces for application in digital microfluidics." *Journal of Fluids Engineering* 130.8 (2008): 081603.
47. Moon, Hyejin, Sung Kwon Cho, and Robin L. Garrell. "Low voltage electrowetting-on-dielectric." *Journal of applied physics* 92.7 (2002): 4080-4087.
48. Guan, Yin, and Albert Y. Tong. "A numerical study of microfluidic droplet transport in a parallel-plate electrowetting-on-dielectric (EWOD) device." *Microfluidics and Nanofluidics*19.6 (2015): 1477-1495.
49. Islam, Md Ashraful, and Albert Y. Tong. "A numerical study of parallel-plate and open-plate droplet transport in electrowetting-on-dielectrode (EWOD)." *Numerical Heat Transfer, Part A: Applications* 71.8 (2017): 805-821.
50. https://www.comsol.com/model/capillary-filling-level-set-method-1878
51. Ismail, Maged. "Level Set and Phase Field Methods: Application to Moving Interfaces and Two-Phase Fluid Flows." *Claremont Graduate University, Claremont*.
52. Olsson, Elin, and Gunilla Kreiss. "A conservative level set method for two phase flow." *Journal of computational physics* 210.1 (2005): 225-246.
53. Amiri, HA Akhlaghi, and A. A. Hamouda. "Evaluation of level set and phase field methods in modeling two phase flow with viscosity contrast through dual-permeability porous medium." *International Journal of Multiphase Flow* 52 (2013): 22-34.

54. Neeson, Michael J., et al. "Compound sessile drops." *Soft Matter* 8.43 (2012): 11042-11050.

55. Wang, Weiqiang, T. B. Jones, and D. R. Harding. "On-chip double emulsion droplet assembly using electrowetting-on-dielectric and dielectrophoresis." *Fusion Science and Technology* 59.1 (2011): 240-249.

56. Guzowski, Jan, et al. "The structure and stability of multiple micro-droplets." *Soft Matter* 8.27 (2012): 7269-7278.

57. Kang, Zhanxiao, et al. "A Dewetting Model for Double-Emulsion Droplets." *Micromachines* 7.11 (2016): 196.

58. Liu, Meifang, et al. "Investigation of spherical and concentric mechanism of compound droplets." *Matter and Radiation at Extremes* 1.4 (2016): 213-223.

59. Black, James Aaron. *Compound droplets for lab-on-a-chip*. Diss. Georgia Institute of Technology, 2016.

60. Kong, Tiantian, et al. "Engineering polymeric composite particles by emulsion-templating: thermodynamics versus kinetics." *Soft Matter* 9.41 (2013): 9780-9784.

61. Dowding, Peter J., et al. "Oil core− polymer shell microcapsules prepared by internal phase separation from emulsion droplets. I. Characterization and release rates for microcapsules with polystyrene shells." *Langmuir* 20.26 (2004): 11374-11379.

62. Shah, Rhutesh K., Jin-Woong Kim, and David A. Weitz. "Janus supraparticles by induced phase separation of nanoparticles in droplets." *Advanced Materials* 21.19 (2009): 1949-1953.

63. Xu, Qiaobing, et al. "Preparation of monodisperse biodegradable polymer microparticles using a microfluidic flow-focusing device for controlled drug delivery." *Small* 5.13 (2009): 1575-1581.

64. De Geest, Bruno G., et al. "Synthesis of monodisperse biodegradable microgels in microfluidic devices." *Langmuir* 21.23 (2005): 10275-10279.
65. Park, Yoonjee, et al. "Monodisperse micro-oil droplets stabilized by polymerizable phospholipid coatings as potential drug carriers." *Langmuir* 31.36 (2015): 9762-9770.
66. Shum, Ho Cheung, et al. "Double emulsion templated monodisperse phospholipid vesicles." *Langmuir* 24.15 (2008): 7651-7653.
67. Schmidt, John J., Jon Rowley, and Hyun Joon Kong. "Hydrogels used for cell-based drug delivery." *Journal of Biomedical Materials Research Part A: An Official Journal of The Society for Biomaterials, The Japanese Society for Biomaterials,* 87.4 (2008): 1113-1122.
68. Barikbin, Zahra, et al. "Ionic liquid-based compound droplet microfluidics for 'on-drop'separations and sensing." *Lab on a Chip* 10.18 (2010): 2458-2463.
69. Nabavi, Seyed Ali, et al. "Prediction and control of drop formation modes in microfluidic generation of double emulsions by single-step emulsification." *Journal of colloid and interface science* 505 (2017): 315-324.
70. Yan, Jing, et al. "Monodisperse water-in-oil-in-water (W/O/W) double emulsion droplets as uniform compartments for high-throughput analysis via flow cytometry." *Micromachines* 4.4 (2013): 402-413.
71. Chen, Chia-Hung, et al. "Janus particles templated from double emulsion droplets generated using microfluidics." *Langmuir* 25.8 (2009): 4320-4323.
72. Vladisavljević, Goran T., Ruqaya Al Nuumani, and Seyed Ali Nabavi. "Microfluidic production of multiple emulsions." *Micromachines* 8.3 (2017): 75.
73. Lee, Tae Yong, et al. "Microfluidic production of multiple emulsions and functional microcapsules." *Lab on a Chip* 16.18 (2016): 3415-3440.

74. Chen, Xiaodong, et al. "Tunable structures of compound droplets formed by collision of immiscible microdroplets." *Microfluidics and Nanofluidics* 21.6 (2017): 109.
75. Li, J., and D. A. Barrow. "A new droplet-forming fluidic junction for the generation of highly compartmentalised capsules." *Lab on a Chip* 17.16 (2017): 2873-2881.
76. Che, Zhizhao, Teck Neng Wong, and Nam-Trung Nguyen. "A simple method for the formation of water-in-oil-in-water (W/O/W) double emulsions." *Microfluidics and Nanofluidics*21.1 (2017): 8.
77. Nie, Zhihong, et al. "Polymer particles with various shapes and morphologies produced in continuous microfluidic reactors." *Journal of the American chemical society* 127.22 (2005): 8058-8063.
78. Okushima, Shingo, et al. "Controlled production of monodisperse double emulsions by two-step droplet breakup in microfluidic devices." *Langmuir* 20.23 (2004): 9905-9908.
79. S. Ma, W. T. Huck, and S. Balabani, “Deformation of double emulsions under conditions of flow cytometry hydrodynamic focusing,” *Lab on a Chip*, *15*(22), 4291-4301, 2015.
80. Li, Jiang, Haosheng Chen, and Howard A. Stone. "Breakup of double emulsion droplets in a tapered nozzle." *Langmuir* 27.8 (2011): 4324-4327.
81. Khan, Saif A., and Suhanya Duraiswamy. "Microfluidic emulsions with dynamic compound drops." *Lab on a Chip* 9.13 (2009): 1840-1842.
82. Stone, H. A., and L. G. Leal. "Breakup of concentric double emulsion droplets in linear flows." *Journal of Fluid Mechanics*211 (1990): 123-156.

83. Lavrenteva, O. M., L. Rosenfeld, and A. Nir. "Shape change, engulfment, and breakup of partially engulfed compound drops undergoing thermocapillary migration." *Physical Review E* 84.5 (2011): 056323.
84. Chen, Haosheng, et al. "Breakup of double emulsions in constrictions." *Soft Matter* 7.6 (2011): 2345-2347.
85. Khan, Saif A., and Suhanya Duraiswamy. "Microfluidic emulsions with dynamic compound drops." *Lab on a Chip* 9.13 (2009): 1840-1842.
86. Min, Nam Gi, et al. "Microfluidic production of uniform microcarriers with multicompartments through phase separation in emulsion drops." *Chemistry of Materials* 28.5 (2016): 1430-1438.
87. Shi, Weichao, and David A. Weitz. "Polymer Phase Separation in a Microcapsule Shell." *Macromolecules* 50.19 (2017): 7681-7686.
88. Zarzar, Lauren D., et al. "Dynamically reconfigurable complex emulsions via tunable interfacial tensions." *Nature* 518.7540 (2015): 520.
89. Li, Jiang, et al. "Electrowetting-on-dielectrics for manipulation of oil drops and gas bubbles in aqueous-shell compound drops." *Lab on a Chip* 14.22 (2014): 4334-4337.
90. Fan, Shih-Kang, Yao-Wen Hsu, and Chiun-Hsun Chen. "Encapsulated droplets with metered and removable oil shells by electrowetting and dielectrophoresis." *Lab on a Chip* 11.15 (2011): 2500-2508.
91. Fan, Shih-Kang et al., "Encapsulated droplets with metered and removable oil shells by electrowetting and dielectrophoresis." *Lab on a Chip* 11.15 (2011): 2500-2508.
92. Cho, Sung Kwon, Hyejin Moon, and Chang-Jin Kim. "Creating, transporting, cutting, and merging liquid droplets by electrowetting-based actuation for digital

microfluidic circuits." *Journal of Microelectromechanical systems* 12.1 (2003): 70-80.

93. Bhattacharjee, Biddut. *Study of droplet splitting in an electrowetting based digital microfluidic system*. Diss. University of British Columbia, 2012.
94. Guan, Yin, and Albert Y. Tong. "A numerical study of droplet splitting and merging in a parallel-plate electrowetting-on-dielectric device." *Journal of Heat Transfer* 137.9 (2015): 091016.
95. Nikapitiya, NY Jagath B., Mun Mun Nahar, and Hyejin Moon. "Accurate, consistent, and fast droplet splitting and dispensing in electrowetting on dielectric digital microfluidics." *Micro and Nano Systems Letters* 5.1 (2017): 24.
96. Hassan, Md. *Experimental study of droplet actuation, splitting and particles manipulation using a cross scale digital microfluidics prototype*. Diss. University of British Columbia, 2013.
97. Banerjee, Ananda, et al. "Deterministic splitting of fluid volumes in electrowetting microfluidics." *Lab on a Chip* 12.24 (2012): 5138-5141.
98. Samiei, Ehsan, and Mina Hoorfar. "Systematic analysis of geometrical based unequal droplet splitting in digital microfluidics." *Journal of Micromechanics and Microengineering* 25.5 (2015): 055008.
99. Li, Yifan, et al. "Enhanced micro-droplet splitting, concentration, sensing and ejection by integrating ElectroWetting-On-Dielectrics and Surface Acoustic Wave technologies." *Solid-State Sensors, Actuators and Microsystems Conference (TRANSDUCERS), 2011 16th International*. IEEE, 2011.
100. Cui, Weiwei, et al. "Dynamics of electrowetting droplet motion in digital microfluidics systems: from dynamic saturation to device physics." *Micromachines* 6.6 (2015): 778-789.

101. https://www.electrochem.org/dl/interface/spr/spr07/spr07_p38.pdf

102. https://en.wikipedia.org/wiki/1-Butyl-3-methylimidazolium_hexafluorophosphate.

103. https://www.aciscience.org/docs/Physical_properties_of_glycerine_and_its_solutions.pdf

Biographical information

Mun Mun Nahar was born in Bangladesh. She received her BSc. in Mechanical Engineering degree from Bangladesh University of Engineering and Technology in 2011. She joined the Integrated Micro-Nanofluidics Lab (IMNfL) at UTA in 2013 for graduate studies and finished her PhD in July, 2018. Her research interests include droplet microfluidics, interfacial phenomena and microscale flow.